

Volume 8, Issue 2, October, 2016

*Proceedings of the National Seminar on “Frontiers in Science
and Technology Towards National Development”*

C O N T E N T S

Sl. No.	Name of the article	Author(s)	Page No.
1	Cognitive behaviour therapy- a way of addressing mental health problem	Dilip Kumar Guin	02-05
2	Promises of cryopreservation as tool in reproductive medicine- a pilot study with murine ovarian tissue	Debojyoti Dutta	06-10
3	Ethno-medicinal formulations against hair and scalp problems in paschim medinipur district, West Bengal, India	Rajendra Prasad De	11-15
4	Coordination chemistry on metal promoted c-n bond formation processes by the oxidative fusion of isomeric amino pyridines to coordinated 2-phenylazo pyridine (pap) ligand	Srijit Das	16-24
5	Structural and thermal properties of Cu and Co substituted $\text{Ni}_{46}\text{Mn}_{43}\text{Sn}_{11}$ ferromagnetic shape memory alloys	Rahul Das	25-28
6	Solid phase crystallization (spc) of nanocrystalline silicon (nc-Si:H) films: changes in structural and optical properties	Dr. Romyani Goswami	29-35
7	MHD natural convection over a melting horizontal plate in porous medium saturated with a fluid of variable viscosity	Rishi Raj Kairi	36-39
8	Auto-tandem catalysis: An unique approach for the direct conversion of isoxazole to 2-azafluorenone	Sajal Das	40-45
9	Ferroelectric and Antiferroelectric Liquid Crystals – Structures and Applications	Kartick Ch. Dey	46-50
10	Exploring exoticity in the realm of Nuclear Physics: relevance in Astrophysics	Prabir Banerjee	51-53
11	Stable violet to green luminescent silicon nanoparticles prepared by two different routes	Das <i>et. al.</i>	54-57
12	Bulk viscous cosmological model with modified Chaplygin gas	Partha Sarathi Debnath	58-63



COGNITIVE BEHAVIOUR THERAPY- A WAY OF ADDRESSING MENTAL HEALTH PROBLEM

Dilip Kumar Guin

University B.T. & Evening College, Cooch Behar; Email: guindilip@gmail.com

ABSTRACT

Our society is changing very fast with the development of science and technology. We are advancing in many folds due to the advancement of science and technology, and gradually our society becoming more complex and competitive. We are communicating with our closed mates over phone, e-mail, Whats app etc. instead of face to face meeting. All these are becoming an essential part to our busy life. We are careful about our physical world. But one thing which we do not consider seriously is our mental health. We take helps of doctor while suffering from physical health. But when someone suffers from mental health problem we do not take care of it. Rather in many occasion we consider the individual as mad. It stigmatise the person in a wrong way. But, it is fact, without any good mental health nobody can live peacefully in spite of having much man power, money etc. We are facing a great challenge to cope with the problems of mental health. Due to poor mental health development the incidence of suicide, taking drugs, rape are raising day by day. Physical health also very much depends on good mental health. So it is essential to promote good mental health for the development of the individual as well as the society. There are many methods and techniques to address the challenges. Cognitive Behaviour Therapy (CBT) is one of such important techniques. This paper attempted to explore the underlying principle of CBT to address the issue of mental health problem.

Key words: *Cognitive Behaviour Therapy, Mental Health*

Introduction

Cognitive Behavior Therapy (CBT) is a form of psychotherapy that talks about how you think about yourself, the world and other people. How your action affects your thoughts and feelings and vice versa. CBT can help to change how we are thinking ("Cognitive") and what we are doing ("Behaviour)". These changes can help us to feel better. CBT mostly focuses on looking for ways to improve mental wellbeing of the individual.

CBT says that it's not the event which causes our emotions, but how we interpret that event - what we think or what meaning we give that event or situation. For instance, if someone you know passes you in the street without acknowledging you, you can interpret it several ways. You might think he/she don't want to know you because no-one likes you (which may lead you to feel depressed), your thought may be that you hope he/she don't stop to talk to you, because you won't know what to say and they'll think you're boring and stupid (anxiety), you may think he deliberately avoid you (leading to anger). A healthier response might be that they just didn't see you.

Aaron Beck developed a form of psychotherapy in the early 1960s that he originally termed "cognitive therapy." "Cognitive therapy" is now used synonymously with "cognitive behavior therapy". Beck devised a structured, short-term, present-oriented psychotherapy for depression, directed towards solving current problems and modifying dysfunctional (inaccurate and/or unhelpful) thinking and behaviour (Beck, 1964).

The Cognitive Model

Cognitive behavior therapy is based on the cognitive model, which hypothesizes that people's emotions, behaviors, and physiology are influenced by their perception of events. Based on a particular situation thought comes to our mind and we react (behave) according to our such thought. In the last example, someone you know passes you in the street without acknowledging you is the situation. He/She don't know you because no-one likes you is the thought based on the situation and which lead you to fell depressed is behaviour/action. The relation among situation, thought and behaviour may be expressed by the arrow diagram.

Situation/Critical Incident → Automatic Thoughts → Reaction (emotional, behavioural, psychological)

A model of recording a sequence of events may be as-

Critical incident	Automatic thought	Reaction
The event or situation that triggered thought and feelings	The thought that went through head when the activating event occurred(or after)	Actions-How did you act then? Emotions-What did you feel then?

Hierarchical Organization of Thinking

Thinking or thoughts may be classified in three categories- Automatic thought, Intermediate thought and Core belief (thought). Core beliefs influence our intermediate thoughts and intermediate thoughts influence our automatic thoughts.

I. Automatic Thoughts:

Automatic thoughts are Immediate, first, quick thoughts that go through our mind in response to a situation. It is the initial thinking reactions that go on to affect emotions and behaviors. This thought may be negative or positive but usually go unnoticed, only emotion noticed.

Examples:

- “She thinks I’m weird”
- “I won’t pass that test”

II. Intermediate Beliefs:

Intermediate beliefs are formed based on core belief. It Influence the direction of our automatic thoughts (positive/negative), expectations and assumptions about ourselves, relationships and situations around us. It governs the rules and guidelines we follow while behaving. It is also linked with attentional priorities and biases which influence what we notice or don’t notice and the ways we think and respond to a given situation.

Examples:

- “ Meeting new people is something to avoid”
- “ Always look for danger and expect it to be there”

III. Core Beliefs are fundamental level belief:

It is global, rigid and over generalized. It represent our underlying self-values and perceptions, Underlying views of ourselves, others and the world around us.

Examples:

- “ I am worthless”
- “ I am helpless”
- “ No one loves me”
- “ I am unsafe in the world”

Hierarchy of Cognition

Core (unconditional) beliefs/schemas: Across situations



Underlying assumptions/conditional assumptions/intermediate beliefs/attitudes/rules (if – then): Situational



Negative Automatic Thoughts (NATs)

Relationship of Behaviour to Automatic Thoughts

One’s perception and thoughts are influenced by underlying beliefs. And such perception of the situation leads to automatic thoughts which then influence emotion. Thus the ultimate reaction towards the situation is the result of one’s core belief, intermediate belief, critical incidence and automatic thought.

Core Beliefs → Intermediate beliefs (rules, attitudes, assumptions) → Critical Incident → Automatic thoughts → Reaction (emotional, behavioural, and physiological).

Situation	Emotions (0-100%)	Physical emotion	Unhelpful thoughts/images	Alternative realistic thought	What did? What I could do? Rerate emotion (0-100%)
What happened? Where? When? With whom? How?	What emotion did I feel at that time? What else? How intense was it?	What did I notice in my body? Where did I feel it?	What went through my mind? Thoughts/image/memories? What am I responding to? Do I think I am being treated unfairly?	What is the bigger picture? Is there another way of seeing it? What advice would I give someone else?	What could I do differently? What would be more effective?

This relation indicates that if one has wrong core belief, it affects other beliefs and the final reaction towards the situation. For proper behaviour against a situation we require right cognition otherwise it mislead our behavior. In many occasion due to our wrong perception we feel anxiety, depression and other psychological problems. Thus identification of our dysfunctional thought is essential for showing proper behaviour.

Dysfunctional thought record (DTR)

DTRs are used for a number of purposes. Early in treatment, it provide a means of recording Negative Automatic Thoughts (NAT) associated with emotional change. They provide information concerning the content of negative automatic thoughts and offer a means by which the individual can develop an awareness of the links between thoughts and feelings.

Cognitive Distortions

It refers to the distortion of thought which is not right in absolute terms. It comes due to our belief system. Such distorted thought directs our behavior that may be unpleasant to the individual. So some knowledge of distorted thought may guide us in a better way. Some important types of cognitive distortion are as follows:

I. All or nothing thinking/ Black and White Thinking:

Thinking of things in absolute black and white categories like “always”, “every” or “never”.

For example,

- if your performance falls short of perfect, you see yourself as a total failure.
- When a young woman on a diet ate a spoonful of ice cream, she told herself, “I’ve blown my diet completely.” This thought upset her so much that she gobbled down an entire quart of ice cream!

II. Overgeneralization:

Taking isolated cases and using them to make wide generalizations. For example, you see a single negative event as a never-ending pattern of defeat: “She yelled at me. She’s always yelling at me. She must not like me.” Always, Never, All of Them, None of them, Everybody, Nobody, All of the time, None of the time etc. are the normal type of overgeneralization.

III. Selective Abstraction:

Focusing exclusively on certain, usually negative or upsetting, aspects of something while ignoring the rest. So, you pick out a single negative detail and dwell on it exclusively while ignoring the positive. Which diverted the reality and vision becomes darkened, like the drop of ink that discolours a beaker of water.

Example: You receive many positive comments about your presentation to a group of associates at work, but one of them says something mildly critical. You obsess about his reaction for days and ignore all the positive feedback.

IV. Mind Reading:

You assume that people are reacting negatively to you when there is no definite evidence for this. You assume what they must be thinking about you.

V. Magnification or minimization:

It consists of perceiving a case or situation in a greater or lesser light than it truly deserves. For example- you have made a small mistake and you think it's a big one.

Distorted cognition is the basic source of our unhealthy and disturbed behaviour. Thus the identification of distorted cognition and their restructuring is essential for the development of healthy mind.

Identifying assumption and core beliefs**Down word arrow technique:**

This involves encouraging clients to pursue the personal implications of a particularly dysfunctional thought. The counsellor asks "What does that mean to you"? In order to peel away layers of thought to uncover an underlying assumption or core belief.

For example a person telling that-
Other will see that I am blushing.

Counsellor: What does it mean that others will see that you are blushing?

It means others will wonder what is wrong with me.

Counsellor: What will it mean if others wonder what is wrong?

Then I will be exposed.

Counsellor: What does it mean to be exposed?

It means I am weak, a less of man.

This example shows that the basic cause of blushing is his weakness and it is the core belief related to the situation.

Conclusion

Core beliefs play a central role in cognitive theory and thus modification of core beliefs is essential for modification of other layers of cognition in the cognitive model. A healthy belief system helps to decrease the weight that an unhelpful schema carries. Some common strategies for the modification of erroneous thoughts are Socratic questioning, Evidence for and against technique, Cost and benefit analysis, Inverted pyramid technique and Pie technique. We may practice these techniques to know our actual thoughts and beliefs. While we face mental problem, disturbance or blame others we need to restructure our thoughts and beliefs in proper way for betterment of our behaviour, as behaviour is the result of thoughts towards the situation.

References

- Anxiety BC. Resources. Results. Relief. Retrieved from internet sources,dt-01.10.16
 Carol Vivyan (2009), An introductory Self-Help course in Cognitive Behaviour Therapy. Retrieved from internet sources,dt-01.10.16
 Discussion by Gargi Das Gupta. Short term course on 'Basic skill of counselling from 15.03.16 to 21.03.16'. UGC Human Resource Development Centre(HRDC) at Jadavpur University.
 South Central (Rural) MIREC Clinical Education Product. A therapist's Guide to Brief Cognitive Behaviour Therapy. Retrieved from internet sources,dt-01.10.16

PROMISES OF CRYOPRESERVATION AS TOOL IN REPRODUCTIVE MEDICINE- A PILOT STUDY WITH MURINE OVARIAN TISSUE

Debojyoti Dutta

Post Graduate Department of Zoology

Acharya B N Seal College, P.O. & Dt- Cooch Behar, PIN-736101

Email: - debojyotidutta2001@yahoo.com

ABSTRACT

The experimental evidence for low temperature storage of ovarian tissue is encouraging. Although restoration of fertility with cryopreserved ovarian grafts has been successful in various animals, there are uncertainties about the optimum use of stored ovarian tissue in humans. Auto transplantation appears to be promising, but the potential risk of transmitting malignant cells in women with cancer is of great concern. The maturation of primordial follicles with Xenopplantation is encouraging, but the efficacy and safety of this method need further investigation. Furthermore, the quality of oocytes that have been matured in a host animal is unknown. The development of *invitro* culture systems for oocytes maturation is still in its infancy. There are many issues to be resolved in ovarian transplantation before the full clinical use of this emerging technique. Most of all, there is an urgent need to optimize the freeze/ thaw procedure and to find the means to protect grafts from ischemia-reperfusion injury. Nevertheless ovarian transplantation should to be clinically useful for women at risk for premature ovarian failure. This paper deals with standardization of cryopreservation protocol based on Murine ovarian tissue to see it's efficacy in different cryoprotective agents. It has been seen that Glycerol is not perfectly active in murine ovarian tissue. Ethylene Glycol having less penetrative behavior. But Di methyl Sulfoxite (DMSO) is ideal in murine ovarian tissue cryopreservation.

Keywords: Transplantation, Cryopreservation, Antifreeze Protein, Ovarian Tissue, Cancer, fertility.

Introduction

With recent advances in clinical management of Cancer Patients, using aggressive chemotherapy and radiotherapy, survival rates have improved for both hematological malignancies and solid tumors (Meirow, 1999). Survival rates increased from 50 to nearly 90% in case of Hodgkin's disease from 4 to 67% for acute lymphocytic leukemia and from 33 to 77% for Wilm's tumor diagnosed during childhood; in addition survival of breast cancer has reached 70-75%. (Roberts & Okatay, 2005; Wallace *et.al.* 2005; Ridley *et. al.* 2005; Tournaya *et. al.* 2004).

The treatment to cure cancer is toxic to gonads. Ovarian damage and failure is a common long term side effect of curative chemotherapy. Sterilization and early menopause in the females has great impact on patient self esteem and quality of life. Amenorrhea is found in 40-68% of cases and the patients who enter normal cycles may experience premature menopause as a result of depleted follicles store in the ovaries (Thomson *et. al.* 2002; Brydoy *et. al.* 2005) These facts represent a serious problem for the cured patient because most of them are young and expect a normal reproductive life (Sonmezer & Okatay, 2004).

By cryopreserving a portion of the gonads, the patients can potentially have his/her own reserve of germ cells, which at a later date could be used for achieving genetic parenthood. For men in their reproductive age, there are enormous psychological implications for the continuity of their genetic lineage, partnering and masculinity. Semen sample could be cryopreserved as a precaution against lifelong sterility in cancer patients and also for infertile men undergoing testicular biopsy.

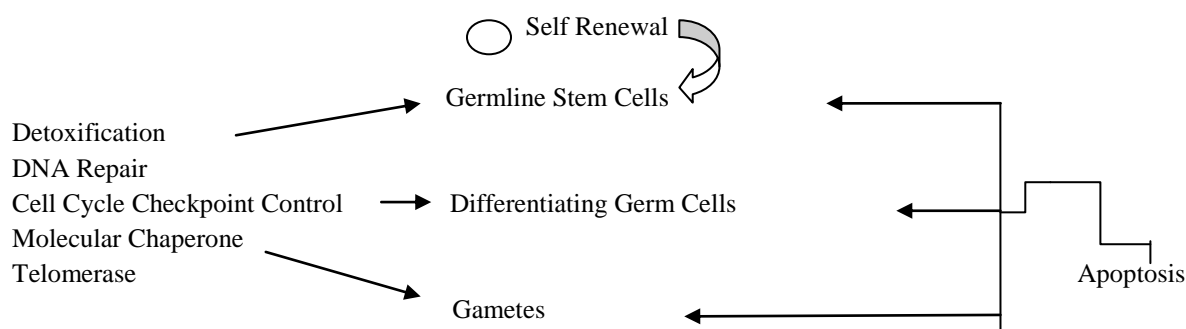


Fig.1. Schematic summary of Mechanisms involved in preserving Fertility Potential.

Thus men and women would benefit enormously if their gonadal biopsies are cryopreserved for future use prior to cancer therapy. Besides cancer, other situations of gonadal insufficiencies also exist e.g., Polycystic ovarian syndrome, primary ovarian failure, turner syndrome in females and varied reasons of infertility in males, cases where oophorectomy is devised e.g., endometriosis, recurring breast cancer etc. would also be benefitted by this novel approach.

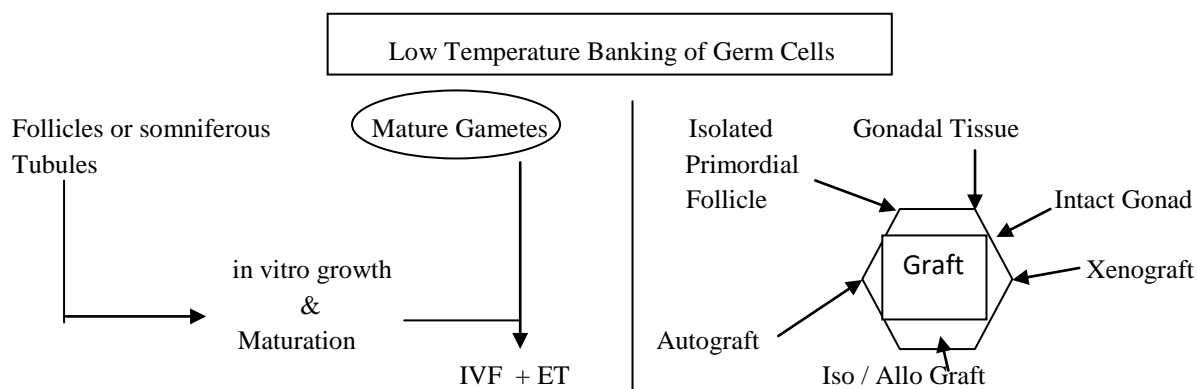


Fig.2. Practical & Theoretical options for Conserving Fertility by Low Temperature Banking of Germ Cells & Gametes.

Essentially these options involve either the growth or maturation *in vitro* or *in vivo* after transplantation or the collection of mature oocytes and spermatozoa for cryopreservation for subsequent *in vitro* fertilization and embryo transfer i.e., *in vitro* fertilization and Embryo transfer technology. One of the million dollar question is the indications for fertility preservation. The imperatives and indications for fertility preservation are

- High dose chemotherapy and pelvic irradiation.
- Pelvic disease for example Endometriosis.
- Surgical extirpation of gonadal tissue.
- Incipient ovarian failure for example premature menopause.
- Natural ageing of the ovaries.
- Preserving transgenic strains for experimental Biology.
- Conservation of rare breeds of farm animals and endangered species.

In this paper attempts are undertaken to standardization of cryopreservation protocol in Murine ovarian tissue in UK-Planner cryofreezer and investigate efficacy different cryopreservative agents to select the ideal one.

Materials and Methodology

Sample collection and transport:

During experimentation, four female rats were anesthetized by xylozine & Ketamine intra peritoneal injection is distilled water. Concentration of Xylazine is 0.16% and Ketamine 1.2%. Dose of Xylazine 16 mg/Kg and Ketamine 120 mg/Kg. The animals were scarified as per guideline of Institutional Ethical Committee. Then the body hairs in the ventral side of the rats were wiped out with the help of electric razor. The rats were dissected with autoclaved scissors and ovarian sample were transported in media M199 (containing NaHCO₃-370 mg, HEPES-600 mg, BSA-100 mg in 10 ml. Distilled water) at room temperature.

Tissue Slicing:

The fixed tissue were then placed in sterile petriplates at 37°C and sectioned into 1-3 slices under stereomicroscope on stage warmer. The sections were then freeze dried and rolled for 30 mins. It is then placed in freezing solution [Consists of L-15 media, 1.5(M) DMSO, 10% FCS, 0.1(M) sucrose] at 4°C.

Cryofreezing:

Then the tissues under cryofreezing starting Temperature 0°C and cooled at the rate of 2°C/min to 7°C. After this, the tissues were soaked for 10 mins. & seeded manually to touching cryotubes with forceps prechilled in liquid nitrogen. The cooling process was continue at 0.3°C/min to -40°C in slower rate and then at faster rate of 10°C/min to -140°C. Then the tissues were transferred to liquid nitrogen for storage.

Thawing:

Tissues were then thawed at 37°C and then removed quickly. Then tissues were placed in various petridishes with 3 ml. antibiotic medium containing 1(M) of cryoprotectant and 0.1(M) L-Sucrose for 5 mins; 0.5(M) of cryoprotectant and 0.1(M) L-sucrose for 5 mins and 0.1(M) L-sucrose for mins. Tissue was then transferred to fresh medium for culture or could be fixed for electron microscopic studies.

Staining schedule:

Conventional haematoxylin and eosin staining was done. Rat ovarian tissue after successful dissection and progressive dehydration were embedded in paraffin for block preparation. This acted as control and undergoes conventional H & E protocol of staining after preparation of thin sections in microtome. 3 rat ovaries after incision undergo cryopreservation with PLANNER-UK following protocol depicted above. One of the Rat ovary was cryopreserved in Ethylene Glycol as cryopreservative agent, next one is cryopreserved with Glycerol as CPAs, the last ovary is cryopreserved without any cryopreservative agents but following slow cooling and fast thawing protocol which is recommended by most of the literature.

Result

In these studies cortical ovarian biopsies was collected by direct incision. The biopsies (small ovarian section) become a source of small follicles which are less vulnerable to cryopreservation as they are smaller in size, metabolic rate is low, cells are arrested in prophase of meiosis hence no spindle, less number of support cells, absence of zona pellucid and less amount of cold sensitive intracytoplasmic lipid.

The control rat ovarian tissue (**Fig.3a**) primordial, primary and secondary follicles are numerous in numbers. Graffian follicles with more or less middle position underlying ovum are clear. Large number of fat droplets is seen in overlapping section. Ovarian tissue cryopreserved in ethylene glycol as cryopreservative agents (**Fig.3d**) few numbers of ice crystals are found considerable amount of presence in intrafollicular space. So, some amount of follicles is damaged. Cryopreserved ovarian tissue with glycerol as cryoprotective agents are seen in **Fig.3b**. Most remarkable observation is amount of ice crystals in much less in comparison with ovarian tissue cryopreserved with ethylene glycol (**Fig.3d**). But size of ice crystal is less in comparison with **Fig. 3d**. Cortical tissue in general is atrophied more or less. Usually recommended mode of cooling and thawing protocol for cryopreservation by International bodies is slow cooling and fast thawing protocol. When followed this kind of protocol. When followed this kind of protocol usually ice crystals are formed in around graffian follicular area (**Fig.3c**). Primordial follicles are drastically affected. As in this case no cryoprotective agents are applied over here so cells are vigorously affected by cellular shrinkage. When cryopreserved ovarian cortical

strips are transplanted subcutaneously transplantation of ovarian tissue at defected time intervals to study neovascularization it is being observed that during course of time within 72 hrs. Healthy primordial follicles are seen (**Fig.4a to 4c**).

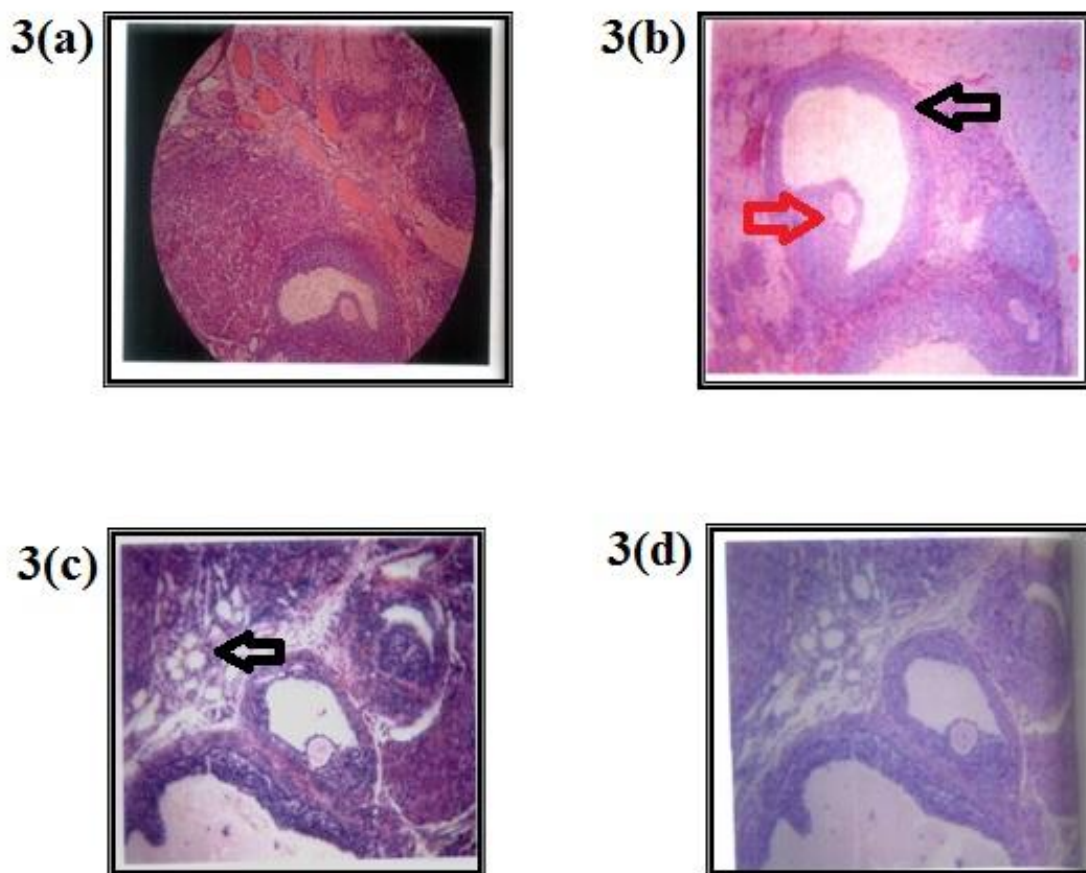


Fig.3: (a) Rat ovarian tissue (control) showing general histology of ovarian tissue showing all cellular architecture intact. (b) Cryopreserved ovarian tissue with glycerol as CPA. Black arrow indicates healthy graffian follicle and red arrow indicate normal ovum going to rupture. (c) Rat ovary cryopreserved using slow cooling & fast thawing protocol without Cryopreservative agents. Black arrow indicates ice crystal. (d) Cryopreserved ovarian tissue with Ethylene glycol as CPA.

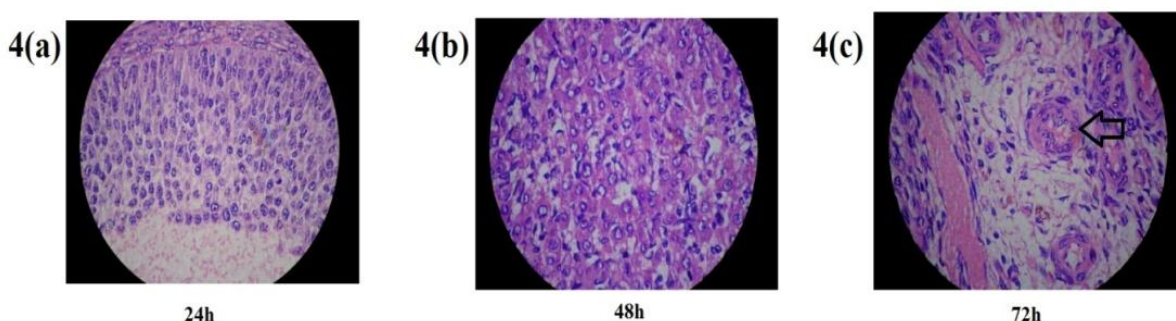


Fig.4: Histological sections of subcutaneous transplantation of ovarian tissue at different time intervals to study neovascularization. (a) 24 hrs after subcutaneous transplantation. (b) 48 hrs. after subcutaneous transplantation. (c) 96 hrs. after subcutaneous transplantation. Healthy primordial Follicle is evident by arrow.

Discussion

One of the biggest challenges to all cancer survivors is to have their own genetic lineages. This is due to loss of reproductive potential. In crude sense it is due to loss of germ cell in both the sexes. If germ cell is cryopreserved prior to cancer therapy in both the patients then it is possible to retain their fertility potentials after aggressive chemo/ Radiotherapy. Because germ cell reserve can possibly be utilized for future use. Therefore, standardization of cryopreservation protocol in Indian context is the urgent task which would be solved by reproductive Biologists.

The first breakthrough in Assisted Reproductive Technology (ART) in form of cryobiology over 50 years ago was the discovery of glycerol as cryoprotective agents (CPAs). In the present study the effect of glycerol as cryoprotective agents (CPAs) and type of cryopreservation, effect of CPA is also verified. Dimethyl Sulfoxide (DMSO) is recommended as best cryopreservative agent as all the cellular architecture remains more or less intact in comparison with other CPAs. Further studies should be undertaken to develop effective strategy to understand viability percentage before and after cryopreservation.

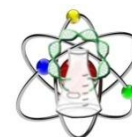
It is too early to predict how for this technology will serve the purposes of fertility preservation or the direction of the next phase of development. Research needs to address the safety and efficiency of Assisted Reproductive technology (ART) and may eventually enable the banking of whole organs for transplantation with vascular reanastomosis. Full development of female and male germ cells in-vitro will contribute to the ongoing revolution in reproductive technology. Such progress in near future will certainly provide new and welcome options for fertility conservation in all cancer survivors.

Acknowledgement

The authors express deepest sense of gratitude to Dr. Deepa Bhartiya, Head, Stem Cell Biology Division at National Institute for Research in Reproductive Health (ICMR), J.M. Street, Parel, Mumbai-400012 for overall guidance in this area of applied Biology. Thanks are extended to the Officer-in-Charge, A B N Seal College for overall academic support at Department of Zoology, A B N Seal College, Cooch Behar.

References

- Brydoy, M., Fossa S. D. and Klepp, O (2005) paternity following treatment for testicular cancer, *Jr. of the National Cancer Institute*, **97**, 1580-1588
- Meirow, D., Fasouliotis, S.J. and Nugent, D (1999) A Laproscopic technique for obtaining ovarian cortical biopsy specimens for fertility conservation in patients with cancer. *Fertile. Steril.*, **71**, 948-951.
- Ridley M., Nicosia S. and Meadows A. (1985) Gonadal effects of cancer therapy in boys, *Cancer* **55**, 2355-2363.
- Roberts, J.E. and Oktay, K. (2005) Fertility preservation: a comprehensive approach to the young women with cancer *J Natl. Cancer Inst. Monogr.*, **57**-59
- Sonmezer, M. and Oktay, K (2004) Fertility preservation in female patients. *Hum Reprod. Update* **10**, 251-266,
- Thomson, A.B., Critchley, H.O.D., Kelner, C.J.H and Wallace W.H.B. (2002) Late reproductive sequelae following treatment of childhood cancer and options for fertility preservation, *Best practice and research: clinical endocrinology and metabolism* **16**, 311-334,
- Tournaye H., Gossens E. and Verheyen G (2004) Preserving the reproductive Potential of men and boys with cancer: current concepts and future prospects. *Hum. Reprod. Update*, **10**, 525-532.
- Wallace, W.H.B, Anderson, R.A and Irvine, D.S (2005) Fertility preservation for young patients with cancer: who is at risk and what can be offered? *Lancet Oncol.* **6**, 209-218,



ETHNO-MEDICINAL FORMULATIONS AGAINST HAIR AND SCALP PROBLEMS IN PASCHIM MEDINIPUR DISTRICT, WEST BENGAL, INDIA

Rajendra Prasad De

Department of Botany, Government General Degree College, Mohonpur, Paschim Medinipur, Paschim Banga, India.

E. mail rajendrade.bot@gmail.com

ABSTRACT

The ethnic communities of Paschim Medinipur district have valuable indigenous knowledge about medicinal plants. Their traditional knowledge for curing numerous diseases is a valuable material for further research of modern system of medicine. But now this ethno-medicinal knowledge of thousand years old is under threat of rapid invasion of urban culture and change of traditional way of life style. Among ethnic people diseases of hair and scalp like dandruff, graying of hairs, hair loss is common and head louse is a major problem of them. They have some traditional medicines using plant materials which are believed to solve these problems. *Allium ascalonicum*, *Allium cepa*, *Citrus aruntifolia* and *Hibiscus rosa-sinensis* are most frequently used in hair and scalp problems by ethnic and other communities. *Cleistanthus collinus* is considered by ethnic communities as most effective to prevent hair loss and to grow new hairs. This work deals with 18 such plants used by the different ethnic communities of Paschim Medinipur District.

Key words: Paschim Medinipur, hair and scalp problems, ethno-medicinal knowledge

Introduction

The district Paschim Medinipur is the second largest district of West Bengal, India. It is situated on the extreme south-western part of West Bengal, and is located in between 22°57'10" N to 21°36'35" N latitudes and 88°12'40" E to 86°35'50" E longitudes. It covers an area of 9786.28 square kilometers (Anonymous, 2003).

The district is bounded in east with Purba Medinipur and Howrah districts of West Bengal, on the west with Mayurbhanj district of Orissa and Purba Singhbhum district of Jharkhand states, on the north with Hooghly, Bankura and Purulia districts of West Bengal and on the south with Purba Medinipur district of West Bengal and Baleshwar district of Orissa state.

The population of ethnic people in Paschim Medinipur district is about 17.55 % of total population, which is largest in West Bengal (Hansda, 2004). Most of them are forest inhabitant and populated in the western forest region. Total number of scheduled tribes in this district is 37 (Mandal *et al.* 2002). Major ethnic communities are Santals, Bhumijis, Mundas, Savars, Koras and Lodhas.

The district is rich in plant diversity also. Many wild plant species are under threat of increasing human population.

The ethnic communities of the district have valuable traditional ethno-medicinal knowledge of their own. Their traditional knowledge for curing numerous diseases (of both human and veterinary) is invaluable to strengthen modern system of medicine. But this indigenous knowledge of thousand years old is also under threat of rapid invasion of urban culture. Their traditional way of life style is also changed rapidly.

Earlier works on ethno-medicinal plants of this area were done by Chaudhuri and Pal (1975), Chaudhuri and Pal (1976), Pal (1988), Pal and Jain (1989, 1998), Ghosh (2003), Paria (2005), De and Bhattacharya (2005), De (2013), De (2015); medicinal plants of the adjacent areas of the district was explored by a number of workers such as Bodding (1925, 1927, 1940), Maiti and Manna (2000), Chakraborty *et al.* (2003), Chakraborty (2006), Chakraborty and Bhattacharjee (2006), Dey and De (2011).

Both the traditional knowledge and its plant (and animal also) materials are under threat of extinction. So the written documentation of this indigenous knowledge is very much needed.

Materials and Methods

Some plants are believed to have useful against hair and scalp problems by ethnic communities of Paschim Medinipur district. Medicinal formulations using these plant materials apply externally on the affected areas. No oral administration is observed for this purpose. This paper deals with 19 such plants used by the different ethnic communities of the district. Field studies in this regard were done by the following way- Interaction with various tribal people for preliminary information about medicinal plants useful against hair and scalp problems.

- i) Consultation with medical practitioners among tribal communities who regularly practice their traditional medicine.
- ii) Consultation with different ethnic groups like Santals, Mundas, Lodhas etc. of the field area to confirm the medicinal property of individual plant used against hair and scalp problems.
- iii) Plant specimens were identified following available literatures (i.e. Prain, 1903; Haines, 1921-1925; Mooney, 1948).
- iv) Ethno-botanical enumeration method as proposed by Jain (1995) and Jain and Mudgal (1999) is followed in this field study with some necessary modifications.
- v) Herbarium specimens are deposited in herbarium of Department of Botany, Government General Degree College, Mohonpur.

19 plant species under 17 genera and 14 families are found to be used against hair and scalp problems by field study. These plants are arranged alphabetically by their botanical name, family, accession number, vernacular name, along with their traditional medicinal formulation/s.

List of abbreviations: B-Bangla; E-English; K-Kurmali; L-Lodha; M-Mundari; S-Santali; Syn.-Synonym.

Results and Discussion

During the survey a number of unique and interesting ethno-medicinal formulations were observed and recorded. The detailed description of the same is enumerated below:

1. *Allium ascalonicum* L. [Liliaceae] RPD-44

Vernacular name: *Chanchi Pniyāj (B); Shallot, Small onion (E):*

1. Bhumijis apply small onion juice with honey externally on head and massage in hair loss or white hairs. Honey sometimes excluded.
2. Some ethnic communities mix small onion juice with leaf juice of *Cleistanthus collinus* and lime juice (about 3:5:2) and apply it externally on scalp to prevent hair loss and to grow new hairs. New juice is prepared after 1 month.

2. *Allium cepa* L. [Liliaceae] RPD-34

Vernacular name: *Piyāj, Pniyāj, Pneyāj (B); Onion (E):*

1. Bhumijis apply onion juice with honey externally on head and massage in hair loss or white hairs. Honey sometimes excluded.
2. Some ethnic communities mix onion juice with leaf juice of *Cleistanthus collinus* and lime juice (about 3:5:2) and apply it externally on scalp to prevent hair loss and to grow new hairs. New juice is prepared after 1 month.
(Ethnic communities prefer *Allium ascalonicum* instead of *Allium cepa*).

3. *Annona squamosa* L. [Annonaceae] RPD-41

Vernacular name: *Ātā, Mādār, Medār, Sitāālphal (B); Custard Apple (E); Mādāl (K, M); Mādārgam (S):*

1. Ethnic communities apply leaf juice external on head and then cover with a cloth to kill lice, for 2-3 days.
2. Mundas prepare ash by burning dried fruits, mix the ash powder with coconut oil and apply externally on head to kill lice.

4. *Azadirachta indica* A. juss. [Meliaceae] RPD-26

Vernacular name: *Nim (B); Neem (E):*

1. Lodhas, Bhumijis and other ethnic communities apply flower paste externally on head to remove lice.

5. *Citrus aruntifolia* (Christon.) Sw. [Rutaceae] RPD-29**Vernacular name: Kāgji lebu, Pāti lebu, Kāgji nebu, Pāti nebu (B); Lime (E):**

1. Santals apply fresh fruit juice on head to cure dandruff (*Khushi*), once in a day preferably half an hour before bathing, up to cure.
2. Some ethnic communities mix lime juice with leaf juice of *Cleistanthus collinus* and small onion juice (in about 2:5:3) and apply it externally on scalp to prevent hair loss and grow new hairs. New juice is prepared after 1 month. Onion juice sometimes used when small onion is not available.

6. *Cleistanthus collinus* (Roxb.) Benth. ex Hook. f. [Euphorbiaceae] RPD-33**Vernacular name: Parhāsi (L, S):**

1. Some ethnic communities mix leaf juice with small onion juice and lime juice (in about 5:3:2) and apply it externally on scalp to prevent hair loss and grow new hairs. Fresh juice is prepared after 1 month. Onion juice is used when small onion is not available.

7. *Clerodendrum viscosum* Venten. [Verbenaceae] RPD-27**Vernacular name: Ghentu, Bhānt, Bhetkāni, Bhetikāni (B); Bhātkān, Hānrhujiki (S):**

1. Mundas apply leaf juice externally on head to kill lice.

8. *Cynodon dactylon* (Linn.) Pers. [Poaceae] RPD-39**Vernacular name: Durbā (B); Bermuda grass (E); Dhup ghās (M); Dhubi (S):**

1. Bhumijis extract juice from 200-250g fresh leafy twigs, mix it with equal amount of juice of *Eclipta prostrata*, boil the mixture with 50g coconut oil, and apply it after sieving and cooling externally on head to stop hair loss, graying of hairs and for strong hair roots.

9. *Datura innoxia* Mill. [Solanaceae] RPD-42**Vernacular name: Krishna dhuturā, Kālo dhuturā (B); Thorn-apple (E); Hende dāotārāo (S):**

1. Kurmis prescribe flower paste mixed with any vegetable oil which is used as hair oil externally on head and bath after 1 hour without soap to prevent hair loss and dandruff. Sometimes petal paste of *Hibiscus rosa-sinensis* is mixed with it.

10. *Datura stramonium* Linn. [Solanaceae] RPD-28**Vernacular name: Dhuturā, Shwet dhuturā, Sādā dhuturā (B); Thorn-apple (E); Ponrh dāotārāo (S):**

1. Kurmis prescribe flower paste mixed with any vegetable oil which is used as hair oil externally on head and dry it for 1 hour to prevent hair loss and dandruff. Sometimes petal paste of *Hibiscus rosa-sinensis* is mixed with it. Soap is prohibited.

11. *Eclipta prostrata* (L.) L. Syn. *E. alba* (L.) Hassk. [Asteraceae] RPD-32**Vernacular name: Keshut, Keshuti, Keshattha, Lāu Keshattha (B); Marsh daisy (E); Lāu Keshari (M); Lāu Keshar (S):**

1. Bhumijis and Kurmis and other communities apply leaf paste externally on hair and retain it for 1-2 hours, then wash without soap for black and strong hairs and to prevent hair loss.
2. Bhumijis extract juice from 200-350g leaves, add equal amount of juice of *Cynodon dactylon* with it, boil the mixture with coconut oil (50g) and apply it after sieving and cooling externally on head to stop hair loss, prevent greying of hairs and for strong hair roots.

12. *Ficus benghalensis* L. [Moraceae] RPD-43**Vernacular name: Bat, Barh (B); Banyan tree (E); Barhe dāre (S):**

1. Lodhas prescribe ash obtained after burning of dry leaves, mixed with coconut oil externally on head in dandruff (*Khushki*).

13. *Hibiscus rosa-sinensis* L. [Malvaceae] RPD-38**Vernacular name:** *Jabā (B); China-rose (E):*

1. Santals prescribe fresh leaf-juice on head to prevent hair loss.
2. Bhumijis mix leaf juice with any vegetative oil (usually coconut oil or any oil used by the patient as hair oil) and prescribe it externally on hair before bath for black hair and to stop hair loss.
3. Santals and other communities use juice of flowers or flower buds on the head to prevent hair loss.
4. Kurmis prescribe petal paste mixed with flower paste of *Datura* spp. and any vegetative oil which is used as hair oil externally on head and dry it for 1 hour, then bath without soap to prevent hair loss and dandruff.

14. *Jatropha curcas* Linn. [Euphorbiaceae] RPD-40**Vernacular name:** *Bāg bherendā, Sādā bherendā, Sādā gābjārāhā (B); Physic nut (E); Bhendrā (M); Pand bhendrā (S):*

1. Bhumijis prescribe latex externally on head of children to prevent hair loss.

15. *Moringa oleifera* Lamk. [Moringaceae] RPD-31**Vernacular name:** *Sajinā (B); Drum stick tree (E); Sallā (M); Mungoo, Munga (S):*

1. Bhumijis apply leaf juice externally on head in dandruff.

16. *Ocimum tenuiflorum* L. Syn. *O. sanctum* L. [Lamiaceae] RPD-37**Vernacular name:** *Tulsi (B); Sacred basil (E); Tursi (S):*

1. Ethnic communities apply crushed leaves (½ cup) externally on scalp for the treatment of dandruff (*Khuski*).

17. *Piper betel* Linn. [Piperaceae] RPD-35**Vernacular name:** *Pān (B); Betel vine (E):*

1. Ethnic communities apply leaf juice externally on head and then cover with a cloth to kill lice, for 2-3 days. Crushed leaves are also used.

18. *Sapindus emarginatus* Vahl. [Sapindaceae] RPD- 30**Vernacular name:** *Rithā (B):*

1. Ethnic and other communities use fruit juice mixed with water externally on head as hair tonic for black and strong hairs, and to reduce hair loss, once in a day for 5-6 days.

19. *Wedelia chinensis* (Osbeck) Merrill Syn. *W. calendulacea* Less [Asteraceae] RPD-36**Vernacular name:** *Bhringarāj (B); Chinese wedelia (E):*

1. Ethnic communities apply leaf paste externally on head to remove head louse.

Conclusion

19 plant species under 17 genera and 14 families are found to be used against hair and scalp problems. Dandruff, graying of hairs, hair loss and head louse are major problems of hair and scalp. A number of ethno-medicinal formulations are observed among different ethnic communities for treatment against these problems. 7 plant species are found to be used against dandruff, these are *Citrus aurantifolia*, *Datura innoxia*, *Datura Strmonium*, *Ficus benghalensis*, *Hibiscus rosa-sinensis*, *Moringa oleifera* and *Ocimum sanctum*. 6 plant species, namely *Annona squamosa*, *Azadirachta indica*, *Clerodendrum viscosum*, *Ocimum sanctum*, *Piper betel* and *Wedelia calendulacea* are used to kill hair lice. They apply juice or paste of plant parts externally on head. Oral administration for this purpose is not observed. *Citrus aruntifolia*, *Eclipta prostrata* and *Hibiscus rosa-sinensis* are most frequently used in hair and scalp problems. *Cleistanthus collinus* is considered most effective to prevent hair loss and to grow new hairs.

References

Anonymous, 2003. *District Statistical Handbook 2002. Paschim Medinipur*. Bureau of Applied Economics & Statistics. Govt. of West Bengal. Kolkata.

- Bodding, P.O. 1925. Studies in Santal medicine and connected Folk lore - I. The Santals and disease. *Mem. Asiat. Soc. Bengal* **10**: 1-132.
- Bodding, P.O. 1927. Studies in Santal medicine and connected Folk lore - II. Santal medicine. *Mem. Asiat. Soc. Bengal* **10**: 133-426.
- Bodding, P.O. 1940. Studies in Santal medicine and connected Folk lore. *Mem. Royal Asiat. Soc. Bengal* **10**: 427-502.
- Chakraborty, M.K. 2006. *Ethnobotany of Purulia district, West Bengal*. Ph. D. Thesis, Vidyasagar University.
- Chakraborty, M.K. & Bhattacharjee, A. 2006. Some common ethnomedicinal uses for various diseases in Purulia district, West Bengal. *Indian Journal of Traditional Knowledge*. 5(4): 554-558.
- Chakraborty, M.K.; Bhattacharjee, A. & Pal, D.C. 2003. Ethnomedicinal uses of some exotic plants of Purulia district, West Bengal, India. *J. Econ. Taxon. Bot.*, 27(3): 559-563.
- Chaudhuri, Rai H.N. & Pal, D.C. 1975. Notes on magico-religious belief about plants among Lodhas of Midnapur, West Bengal, *Vanyajati*. **23 (2-3)**: 20-22.
- Chaudhuri, Rai H.N. & Pal, D.C. 1976. Preliminary observation on ethnobotany of Midnapur District, West Bengal, *Indian Mus. Bull.* **11(2)**:51-53.
- De, R.P. 2013. An Investigation on the Medicinal Plants of Paschim Medinipur, West Bengal. Ph. D. Thesis, Vidyasagar University.
- De, R.P. 2015. Ethno-medicinal formulations against Abdominal and Colic Pain in Paschim Medinipur District, West Bengal, India. *Indian Journal of Plant Sciences*, Vol. 4 (4.)
- De, R.P. & Bhattacharya, A. (2005). Plant used To Stop Bleeding by the Tribal People of Paschim Medinipur District, West Bengal. *Journal of Science, Jhargram Raj College*, **1**: 40-52.
- Dey, A. & De, J.N. (2011). Ethnobotanicals of the family Euphorbiaceae used by the ethnic groups of Purulia district, West Bengal, India. *Life sciences Leaflets*, 18:690-694.
- Ghosh, A. (2003). Herbal folk remedies of Bankura and Medinipur districts, West Bengal. *Indian Journal of Traditional Knowledge*. 2(4): 393-396.
- Haines, H.H. 1921-1925. *Botany of Bihar and Orissa*. Vol. I-VI. Bishen Singh Mahendra Pal Singh, Dehradun, India.
- Hansda, S. 2004. Medinipurer adibasi sampraday: loukik achar-anushtan (in Bengali) in *Paschimbanga, Medinipur jela sankhya, Tathya o sanskriti bibhag*, Govt. of West Bengal. India.
- Jain, S.K. & Mudgal, V. 1999. *Hand Book of Ethnobotany*. Bishen Singh Mahendra Pal Singh, Dehradun. India.
- Jain, S.K. 1995. *A Manual of Ethnobotany* (2nd Ed). Scientific publishers, Jodhpur.
- Maiti, A. & Manna, C.K. 2000. Some ethnomedicines used by the Santal of Baghmundi- Ajodhya hill region of Purulia district, West Bengal, in controlling fertility. *Ethnobotany* **12**: 77-80.
- Mandal, H., Mukherjee, S. & Datta, A. 2002. *India : An Illustrated Atlas of Tribal World*. Anthropological Survey of India, Kolkata.
- Mooney, H. 1948. *Supplement of the Botany of Bihar and Orissa*. International Book Distributors, Dehradun.
- Pal, D.C. & Jain, S.K. 1989. Notes on Lodha medicine in Midnapur district, West Bengal, India. *Econ. Bot.* **43(4)**: 464-470.
- Pal, D.C. & Jain, S.K. 1998. *Tribal medicine*. Nayaprakash, Kolkata.
- Pal, D.C. 1988. Ethnobotany of Midnapur district, India. Ph. D. Thesis, Calcutta University.
- Paria, N.D. 2005. *Medicinal Plant Resources of South West Bengal*. Research wing, Directorate of Forests, Govt. of West Bengal.
- Prain, D. 1903. *Bengal Plants* Vol. I & II. Bishen Singh Mahendra Pal Singh, Dehradun.



COORDINATION CHEMISTRY ON METAL PROMOTED C-N BOND FORMATION PROCESSES BY THE OXIDATIVE FUSION OF ISOMERIC AMINO PYRIDINES TO COORDINATED 2- PHENYLAZO PYRIDINE (PAP) LIGAND

Srijit Das

Department of Chemistry, A.B.N.Seal College P.O & Dist. Cooch Behar, 736101

Email: icsrijit77@gmail.com

ABSTRACT

The design and synthesis of ligand systems capable of accommodating two or more metal centers in close proximity and in predetermined spatial arrangements is an active area of research. The present paper describes the design and synthesis of multidentate pyridyl containing azo based bridging ligands through the metal mediated C-N bond formation processes. The ligand was synthesized by the oxidative fusion of 2-amino pyridine, one of the isomer of amino pyridines, to coordinated 2-phenylazo pyridine (pap) ligand. The ligand upon deprotonation acts as a potential binucleating ligands for different transitional metal ions. The coordination chemistry of these transformed ligands in general displays rich spectral and redox properties, which originate from strong delocalization of electronic charge along the ligand backbone. We have studied extensive study of coordination chemistry of this ligands with group metal ions *viz.* Ni(II), Pd(II), Pt(II), group 12 metal ions in particular d^{10} - metal ions *viz.* Zn(II), Cd(II), Hg(II) and In(III) and group 11 metal ions *viz.* Cu(II). The chemistry of this complexes are of current interest, not only due to their structural parts but also displayed interesting spectral, magnetic, redox and catalytic reactivity that primarily originated due to the interactions between different metal centers. The present paper describes interesting properties of transition metal complexes which have wide important applications in material and redox chemistry.

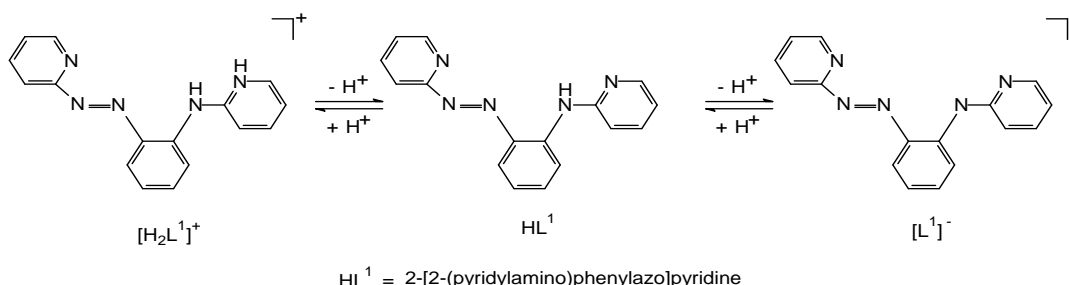
Keywords: 1. Multidentate N-donor bridging ligands 2. Metal mediated C-N bond formation process 3. Coordination Chemistry

Introduction

The synthesis and characterization of the tridentate nitrogen donor ligand, HL^1 , ($HL^1 = 2$ -[2-(pyridylamino)phenylazo]pyridine) was done *via* cobalt promoted¹ C-N bond formation reaction through the regioselective aromatic ring amination of the coordinated 2-(phenylazo) pyridine (pap) ligand. The ligand HL^1 readily loses its proton upon deprotonation and the conjugate base, $[L^1]^-$ coordinates as a bischelating tridentate nitrogen donor ligand (Scheme 1).

Scheme 1

Pictorial representation of HL^1



Coordination chemistry of this ligand is vast not only from their structural part but also from the spectroscopic properties also. The coordination chemistry² of the newly synthesized ligands show interesting structural, redox & magnetic property which were not possible to synthesize such type of tricoordinated ligands having no pyridyl ring during the fusion reaction. The present paper describes the syntheses, structure and spectroscopic property of the azo-based

pyridyl containing ligands with d^{10} metal ions viz. In(III), Zn(II), Cd(II) & Hg(II) and detailed chemistry of binuclear Cu_2 - complexes.

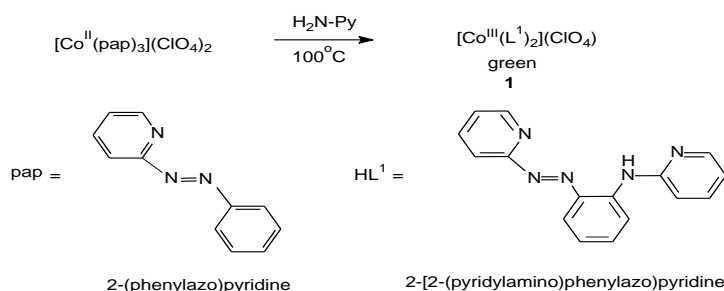
Results and Discussion

A. The Ligand, HL^1 ($HL^1 = 2$ -[2-(pyridylamino)phenylazo]pyridine:

Recently we have reported synthesis and characterization of the bridging ligand HL^1 . We briefly describe¹ here its synthesis and properties. Synthesis of the ligand HL^1 involves cobalt promoted regioselective amination reaction at coordinated 2-(phenylazo)pyridine (pap) ligand. The brown cationic complex, $[Co^{II}(pap)_3](ClO_4)_2$ reacted with molten 2-aminopyridine (H_2NPy) on a steam bath to produce a bis chelated green cobalt (III) complex, $[Co^{III}(L^1)_2]ClO_4$ (**1**) (Scheme 2).

Scheme 2

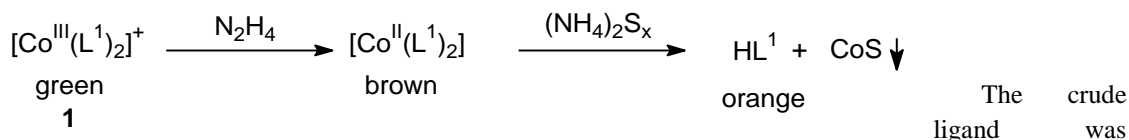
Regioselective aromatic ring amination reaction to coordinated 2- (phenylazo)pyridine



The cationic cobalt complex, **1** was isolated as its perchlorate salt and the free ligand, HL^1 was isolated from the green cobalt(III) complex, $[Co(L^1)_2](ClO_4)$ (**1**) by subsequent reduction of $Co^{III} \rightarrow Co^{II}$ state by dilute hydrazine hydrate followed by removal of the metal ion as CoS using ammonium polysulphide as precipitating reagent. The chemical reaction is presented in Scheme 3.

Scheme 3

Isolation of ligand, HL^1



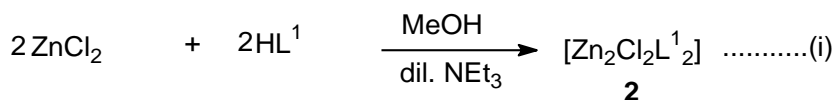
purified finally on a silica gel preparative TLC plate. A major orange-yellow band was eluted with toluene-chloroform (1:2) mixture. Upon evaporation of the solvent, crystalline orange HL^1 was obtained in 80% yield. The ligand is a weak acid with $pK_a = 8.6 \pm 0.1$

B. The Di-zinc Complex $[Zn_2Cl_2L^1_2]$ (**2**)

i) The Synthetic Reaction of $ZnCl_2$ with HL^1 [$HL^1 = NH_4C_5N=NC_6H_4N(H)C_5H_4N$]

The reaction of $ZnCl_2$ with equimolar quantity of HL^1 in presence of dilute NEt_3 as a base in methanol at room temperature (298K) produced an intense blue solution. Upon slow evaporation of the reaction mixture, dark crystals of a di-zinc(II) compound of molecular formula $[Zn_2Cl_2L^1_2]$ (**2**) was obtained in a moderate yield (ca. 50%) (equation i). In this complex conjugate base of ligand HL^1 binds as a normal coordination mode of bridging ligand.

Reaction of $ZnCl_2$ with HL^1



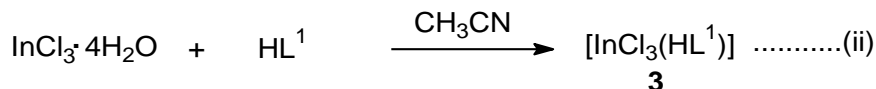
B. The Indium(III) Complex $[InCl_3(HL^1)]$ (**3**)

(i) The Synthetic Reaction of $InCl_3 \cdot 4H_2O$ with HL^1 [$HL^1 = NH_4C_5N=NC_6H_4N(H)C_5H_4N$]

The 1:1 reaction of $InCl_3 \cdot 4H_2O$ with HL^1 in acetonitrile at room temperature (298K) produced³⁻⁵ an ink-blue solution. In an attempt to isolate the indium complex, a solution of HL^1 in acetonitrile was added slowly to a hydrated chloride salt, $InCl_3 \cdot 4H_2O$ dissolved in minimum water. The mixture immediately became ink-blue

and finally the dark crystalline complex of formula, $[\text{InCl}_3(\text{HL}^1)]$ (**3**) was obtained through the slow evaporation of the solution of the compound (equation ii).

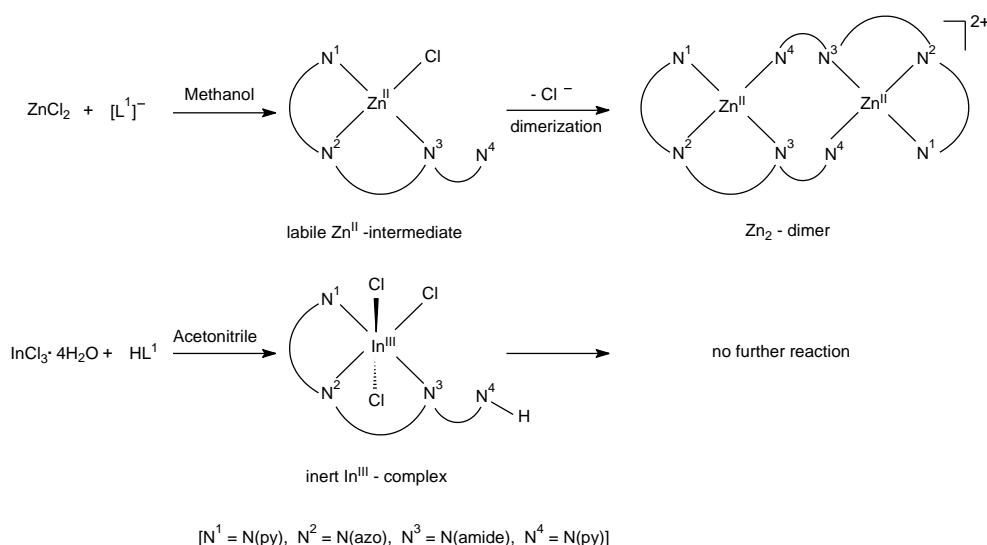
Reaction of $\text{InCl}_3 \cdot 4\text{H}_2\text{O}$ with HL^1



The complex **3** is sparingly soluble in acetonitrile. In this compound the ligand HL^1 coordinates as a tridentate ligand using one pyridyl, azo and deprotonated secondary amine nitrogen atoms. The second pyridyl nitrogen of amino pyridyl function remains unused. Thus the coordination mode of the ligand, in the case of indium(III), is different than that observed in the di-zinc complex, **2**. In the di-zinc compound the anionic ligand $[\text{L}^1]^-$ coordinates to one zinc atom as a tridentate ligand using one pyridyl, azo and the deprotonated secondary amine nitrogen atoms. The second pyridyl nitrogen of amino pyridyl function binds to a second zinc atom. It is believed that lability of the starting material⁵ is crucial for the dimerization process (Scheme 4).

Scheme 4

Dimer vs. monomer



In the case of In(III) salt, because of its high charge, the coordinated chlorides are not labile and hence dimerization was not possible; the dangling pyridyl nitrogen of amino pyridyl function in this case is protonated to produce a molecular, zwitterionic compound. In contrast the corresponding zinc(II) salt⁶, on the other hand, is labile and forms a five coordinate intermediate, which undergoes further dimerization using the pendent pyridyl nitrogen atom to produce a penta-coordinate di-zinc complex.

ii) ¹H NMR Spectra

¹H NMR spectra of mononuclear indium complex were obtained in CD₃CN. The spectra **3** are displayed in Figure 1.

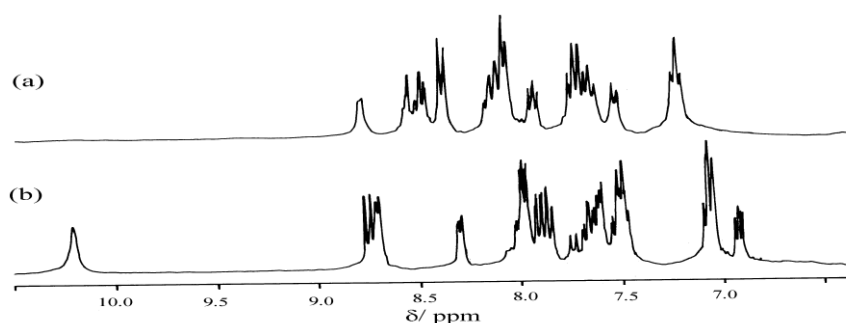


Fig. 1: ¹H NMR spectrum of (a) $[\text{InCl}_3(\text{HL}^1)]$ (**3**) and (b) HL^1 in CD_3CN .

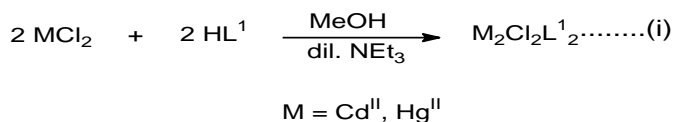
The indium complex showed the absence of N-H resonance, which appeared at 10.6 δ in free ligand, HL¹. However, a new broad resonance at 8.76 δ appeared in the complex **3**. This may be assigned to a pyridyl N-H resonance. ¹H NMR spectrum of **3** was complex in nature due to serious overlap of the unique proton resonances and these could not be assigned individually. The pyridyl and aromatic proton resonances appeared in the region (8.5-7.9) δ and (7.7-7.2) δ , respectively.

D. (i) The Synthetic Reaction of CdCl₂·H₂O and HgCl₂ with HL¹ (HL¹ = 2-[2-(pyridylamino)phenylazo]pyridine)

The metal salts MCl₂ (M= Cd and Hg) react almost instantaneously with an equimolar quantity of HL¹ in presence of dilute NEt₃ as a base at room temperature (298K) in methanol to produce di-metallic complexes of formula [M₂Cl₂L₂¹₂] in good yields (60%) (equation i) (Scheme 5). There were distinct colour changes from orange (free [L¹]⁻) to ink-blue [M₂Cl₂L₂¹₂] in both cases. In an attempt to isolate the present complexes, a solution of [L¹]⁻ in methanol was added slowly to hydrated metal salts, dissolved in minimum water. The mixture immediately became ink-blue in both cases and finally the dark crystalline molecular complexes of formula [M₂Cl₂L₂¹₂] were obtained through⁷⁻¹⁰ the slow diffusion of the toluene into the dichloromethane solution of the compound.

Scheme 5

Reaction of CdCl₂·H₂O and HgCl₂ with HL¹



(ii) NMR Spectra

¹H NMR spectra of di-cadmium and di-mercury complex were obtained in CDCl₃. The spectra of **4** is displayed in **Figures 2**.

(i) [Cd₂Cl₂L₂¹₂] (4**):**

¹H NMR spectrum of the dicadmium complex showed all twelve resonances of coordinated anionic ligand [L¹]⁻. There was no N-H resonance¹⁰ in the ¹H NMR spectrum of **4**. The absence of N-H resonance in **4** indicates that the ligand is coordinated to the metal ion *via* the deprotonation of the secondary amine proton. The spectrum revealed that the two ligands in the dicadmium complex are magnetically equivalent,¹¹⁻¹⁸ indicating the presence of two-fold symmetry axis and each kind of proton of the coordinated anionic ligand [L¹]⁻ gave rise to one signal. The two-pyridyl protons¹⁹ *viz.* 6-H and 3-H resonated as two doublets at 8.52 and 7.51 δ , respectively. The signals due to 5-H and 4-H were triplet appeared at 7.26 and 7.78 δ , respectively. The four-phenyl protons resonated in the region (7.35-5.50) δ . For example, two phenyl protons *viz.* 12-H and 9-H resonate as two doublet at 7.33 and 5.82 δ , respectively. Similarly, 11-H and 10-H appeared as triplet at 6.44 and 6.22 δ , respectively. The pyridyl proton signals due to 15-H and 18-H were doublet and 16-H and 17-H was triplet. They resonated at 8.52, 7.48, 7.78 and 7.20 δ , respectively.

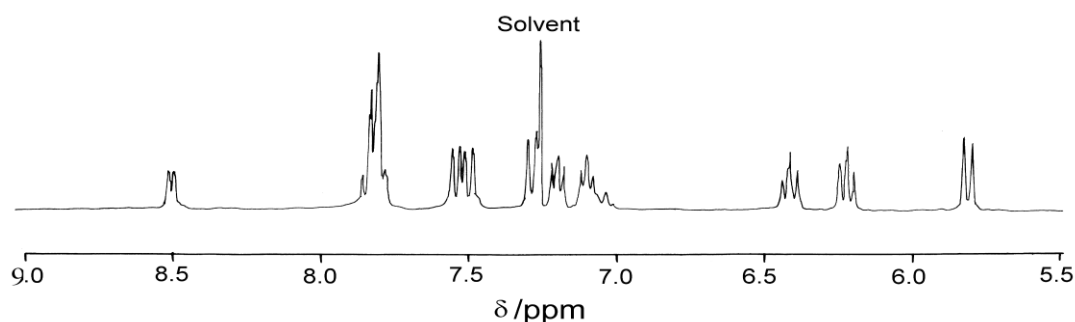


Fig. 2: ¹H NMR spectrum of [Cd₂Cl₂L₂¹₂] (**4**) in CDCl₃.

(ii) $[\text{Hg}_2\text{Cl}_2\text{L}^1_2 \cdot 0.5\text{H}_2\text{O}]$ (**5**):

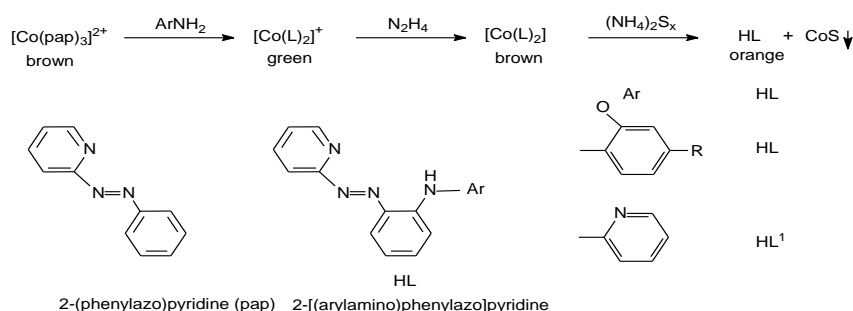
While the room temperature (298K) ^1H NMR spectrum of di-cadmium complex showed resolved but in contrast the ^1H NMR spectrum of di-mercury complex at 298K showed broad spectrum, the phenyl proton resonances were particularly broad. To gain some idea about the reason for broadening of NMR spectrum in the present di-mercury complex, low temperature NMR was studied. It was observed that the spectrum became relatively sharp at subnormal temperatures (<250K). Broad nature of ^1H NMR spectra of Hg(II)- complexes may possibly due to their inherent nature of undergoing rapid exchange in solution with the coordinated ligands.¹⁷ With decrease of temperature the exchange process becomes slow and a sharp spectrum is observed at a low temperature. Like the di-cadmium complex, N-H resonance was absent in complex **5** indicating the presence of conjugate base, $[\text{L}^1]^-$ in the complex. The -pyridyl protons, viz. 6-H and 3-H resonated as two doublet resonances at 8.68 and 7.49 δ , respectively. The signals due to 5-H and 4-H were triplet and appeared at 7.83 and 7.23 δ , respectively. The four-phenyl protons resonated in the region (7.32-5.58) δ . Between them two signals (12-H and 9-H) appeared as two doublet at 7.32 and 5.58 δ , respectively. The rest two-phenyl protons (11-H and 10-H) resonated as triplet at 6.33 and 6.22 δ , respectively. The signals due to 15-H, 16-H, 17-H and 18-H appeared in the range (7.83-7.11) δ .

E. Electronic Spectra of d^{10} - metal complexes

While the indium complex is soluble in acetonitrile the di-zinc, di-cadmium and di-mercury complex, on the other hand, is freely soluble in non-polar solvents such as dichloromethane, chloroform. All the complexes produced ink-blue solution. Their UV-visible spectra were similar with a strong absorption band near 600 nm. In addition, there were multiple transitions in the high energy UV-region. Notably, the lowest energy transition of free $[\text{L}^1]^-$ which appeared at 450 nm was red-shifted considerably to ca. 600 nm in both complexes. We wish to note here that the blue colour of the coordinated ligand ($\text{HL}^1/[\text{L}^1]^-$) appears to be unique for d^{10} -metal ions. The presence of the pyridyl nitrogen is found to be essential for the formation and stabilization of the present complexes. For example, if a phenyl group replaces the bridging pyridyl group, no stable compound of either of the above metal ions could be isolated. Furthermore, deprotonation of $[\text{InCl}_3(\text{HL}^1)]$ (**3**) led to decomposition of the product. All these points indicate that interactions between the pyridyl nitrogen and a lewis acid are important for the formation of these blue complexes of d^{10} -metal ions. Thus the low energy visible range electronic transitions in the present complexes may best be ascribed as intra-ligand $\pi-\pi^*$ transitions. Modification of the properties of ligand orbitals in the present systems is due to increased planarity and conjugation of the ligand framework.^{1,2b} Such intensely coloured d^{10} -metal complexes are rare in the literature.²⁰⁻²² Moreover, the present ligand system may be useful for the detection and extraction of the toxic metal ions such as Cd(II) and Hg(II).

F. (i) The Synthetic Reaction of $\text{CuX}_2 \cdot n\text{H}_2\text{O}$ ($\text{X} = \text{Cl}, \text{ClO}_4$) with HL and HL^1 ($\text{HL} = 2-[(\text{arylamino})\text{phenylazo}] \text{pyridine}$; $\text{HL}^1 = 2-[2-(\text{pyridylamino})\text{phenylazo}] \text{pyridine}$)

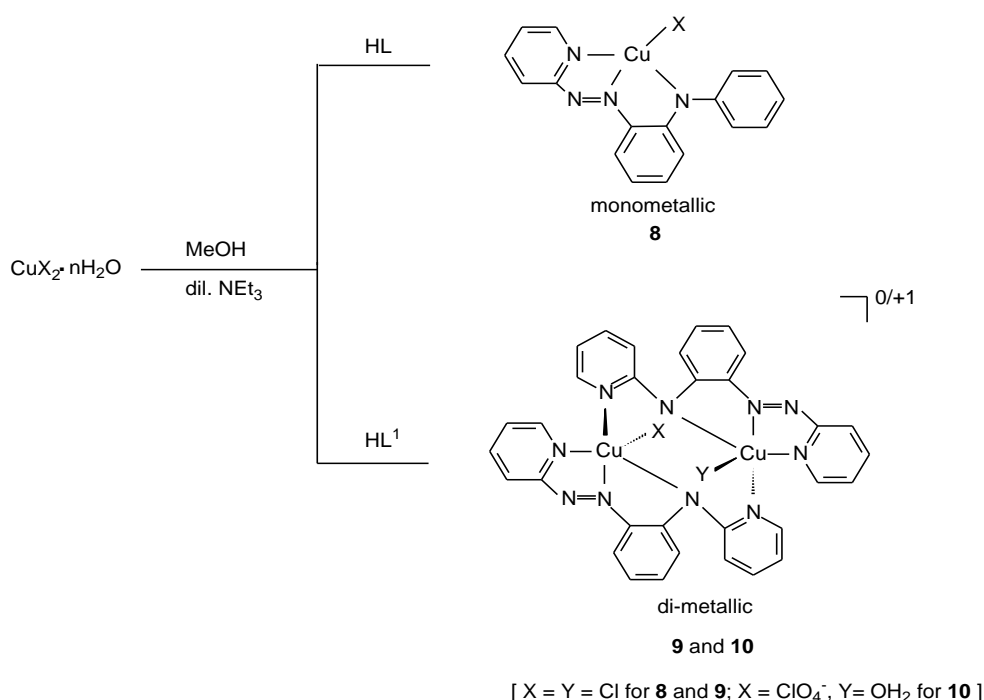
The ligands viz. HL and HL^1 were synthesized¹ by regioselective *ortho*-amine fusion reactions of primary aromatic monoamines on cobalt(II) coordinated 2-(phenylazo)pyridine ligand (Scheme 6).

Scheme 6*Syntheses of Ligand*

The reaction of hydrated $\text{CuCl}_2 \cdot 2\text{H}_2\text{O}$ with an equimolar quantity of the HL in presence of dilute NEt_3 as a base in methanol at room temperature (298K) produced mononuclear copper(II) complexes of chemical composition $[\text{CuClL}]$ (**6**) in good yield (80%). There was distinct colour change from red (free $[\text{L}]$) to green complexes, **6**. A similar reaction of hydrated $\text{CuCl}_2 \cdot 2\text{H}_2\text{O}$ with equimolar quantity of the deprotonated $[\text{L}^1]$ under an identical experimental condition was performed for a comparison. We wish to reiterate here that a phenyl group in $[\text{L}]$ replaces a 2-pyridyl group of $[\text{L}^1]$. The reaction of $\text{CuCl}_2 \cdot 2\text{H}_2\text{O}$ with an equimolar quantity of HL^1 in presence of dilute NEt_3 as a base in methanol produced a molecular di-copper complex having the composition $[\text{Cu}_2\text{Cl}_2\text{L}_2 \cdot \text{H}_2\text{O}]$ (**7**) in a high yield (80%). Besides it, a similar reaction of the hydrated cupric salt, $\text{Cu}(\text{ClO}_4)_2 \cdot 6\text{H}_2\text{O}$ with an equimolar quantity of the deprotonated ligand $[\text{L}^1]$ in methanol produced a cationic di-copper complex $[\text{Cu}_2(\text{OH}_2)(\text{ClO}_4)_2\text{L}_2](\text{ClO}_4)$ (**8**) in a high yield (75%). There were distinct colour changes from orange (free $[\text{L}^1]$) to sky-blue in both cases. The chemical reactions concerning us here are presented in Scheme 7 for comparison.

Scheme 7

Chemical reaction



(ii) ESIMS Measurement

The spectral data of ESIMS measurements of all the copper(II) complexes have been found to be strong support in favour of the formulation of the complexes. The positive ion ESI mass spectra of the complexes viz. **6**, **7** and **8** were recorded in dichloromethane and very clear spectra were obtained in each case. Interestingly, all the mononuclear copper complexes, **6a-c** showed an intense peak at m/z 337, 351 and 383 amu, respectively, which is assigned to $[\text{M}_c - \text{X}]^+$, where M_c and X represent the molecule and Cl^- , respectively. The di-nuclear copper complexes, viz. **7** and **8** on the other hand, showed a peak at m/z 711 and 775 amu, which are assigned to $[\text{M}_c - \text{Cl}]^+$ and $[\text{M}_c - \text{ClO}_4]^+$, respectively. In all cases the experimental isotopic distributions for the molecular ion corresponded with the simulated pattern. Besides these there were many weak daughter peaks, which may be due to fragmentation or unknown combination of fragmented ions. Thus the ESIMS data provide the evidence for the integrity of the complexes also in solution.

(iii) Magnetic Properties

Room temperature (298K) magnetic studies of all the mononuclear copper complexes **6** fall in the range 1.68-1.72 μ_B that are very close to the spin-only value 1.73 μ_B for a single unpaired electron.

Variable-temperature magnetic susceptibility data for the complex **7**, measured at temperature ranging from 2.0 to 300 K, showed very weak antiferromagnetic behavior. From the curve it was observed that the $\chi_m T$ value is $0.91 \text{ cm}^3 \text{ K mol}^{-1}$ at room temperature and it decreases gradually with lowering of temperature. The $\chi_m T = 0.91 \text{ cm}^3 \text{ K mol}^{-1}$ at 300 K is higher than the spin-only value $\chi_m T = 0.75 \text{ cm}^3 \text{ K mol}^{-1}$ for the uncorrelated two Cu^{II} ($S = 1/2$) with $g = 2.00$. Such a high $\chi_m T$ value has been reported¹⁶ for other dinuclear copper(II) complex such as $[\text{Cu}_2(\text{t-bupy})_4(\text{N}_3)_2](\text{ClO}_4)_2$ where t-bupy stands for 4-tert-butylpyridine. The temperature dependence of $\chi_m T$ indicates that two Cu^{II} ions are coupled antiferromagnetically¹⁷ through the bridging ligands. The susceptibility data were fitted by the following expression derived¹⁸ by Bleany and Bowers.

$$\chi = \frac{2Ng^2\beta^2}{kT[3 + \exp(-J/kT)]}$$

Where, N is Avogadro's number, β the Bohr magneton and k Boltzman's constant. A good-fitting curve was obtained for the following parameters: $J = -1.04 \text{ cm}^{-1}$, $g = 2.04$.

Variable-temperature magnetic susceptibility of the complex **8** was measured at temperature ranging from 2.0 to 300 K. At room temperature $\chi_m T$ is equal to $0.82 \text{ cm}^3 \text{ K mol}^{-1}$ (300K). This value at room temperature is higher than the spin-only value $\chi_m T = 0.75 \text{ cm}^3 \text{ K mol}^{-1}$ for the uncorrelated two Cu^{II} ($S = 1/2$) with $g = 2.00$ and $\chi_m T$ is almost constant until 100 K. On further cooling, $\chi_m T$ increases rapidly and reaches a maximum at 5.0 K. The $\chi_m T$ data of temperature range from 10 to 300 K were fitted by the same Bleany and Bowers expression¹⁸ used for the complex **7**. A good-fitting curve was obtained for the following parameters: $J = 4.3 \text{ cm}^{-1}$, $g = 2.08$. The small positive J value indicates a weak ferromagnetic¹⁹ coupling between the two copper(II) ions at low temperature.

(iv) Redox Properties

The redox properties of all the copper(II) complexes, **7-9** were studied by cyclic voltammetry (CV) in dichloromethane solvent using a platinum-working electrode. The complexes **6** and **7** displayed multiple irreversible, quasireversible ill-nature responses. For example, all the mononuclear copper(II) complexes, **6** showed one irreversible anodic response at *ca.* 0.80 V. It also showed two irreversible cathodic responses, which appeared at *ca.* -0.50 and -1.0 V, respectively. Like complex **6**, complex **7** showed one irreversible response at -0.11 V. In contrast, the complex **8**, on the other hand, displayed two closely spaced one-electron reversible responses at +0.06 V and -0.05 V. The separation between the two-reduction processes is small, and the differential pulse voltammetry (DPV) was performed to identify the two successive steps. This reversible couple was further characterized by $i_{pa} = i_{pc}$; $\Delta E_p = 110 \text{ mV}$ and I_{pc} vs. $V^{1/2}$ was constant. Constant potential electrolysis of **8** was performed at -0.4V, which confirmed an overall two-electron transfer for the above response. So the two redox²³⁻²⁶ processes are assigned as follows:



Since the couple, under consideration, is electrochemically reversible, the starting compounds and the reduced species are likely to have very similar gross structure. This was confirmed by the fact that the reduced species, generated in solution, gave rise to response at exactly the same potential when subjected to anodic scan setting the potential 200 mV more positive than the E_{pc} of the parent compound. The reference ligand has a unique combination of hard and soft donor sites and is known to stabilize variable states of different metal ions. Moreover, the lability of the fifth coordinating ligands (H_2O and ClO_4^-) in **8** is believed to be also a key factor for the electrochemical reversibility. For comparison, the cyclic voltammetry of non-labile di-metallic complex **7** under an identical experimental condition showed irreversible responses. Since the processes are electrochemically reversible, the constant potential electrolysis was performed at -0.4V to produce green $[\mathbf{8}]^{2-}$ solution. $[\mathbf{8}]^{2-}$ (green solution) regenerated to parent complex **8** (sky-blue) almost quantitatively upon electrolysis at 0.35V.

(v) Catalytic Properties

Electrochemical reversibility of the complex **8** persuaded us to examine its catalytic properties. The compound **8** reacts²¹ with L-ascorbic acid (H₂A) in aqueous methanol instantaneously to form a brownish-violet solution presumably due to the formation of copper(I) species. The colour of the solution is stable in an inert atmosphere but regenerates the parent complex **8** quantitatively upon exposure to air. The above catalytic reaction was thus followed spectrophotometrically using air saturated solvent mixture. Interestingly, the catalytic cycle is most effective up to H₂A/**8** molar ratio of 20:1 with quantitative regeneration of **8**. The overall rates of regeneration of the parent complex **8** were measured with H₂A/**8** molar ratio of 10:1, 15:1 and 20:1 and the observed rates are 5.75, 4.79 and 2.87 M⁻¹s⁻¹, respectively. In contrast, the complexes **6** and **7** both react with H₂A irreversibly to produce brown solutions of unknown compositions *via* the transient violet intermediates. The above catalytic process involving **8** consisted of several steps that primarily include reduction of **8** by L-ascorbic acid and reoxidation of copper(I) species by aerial oxygen. Catalytic activity²⁷⁻³⁰ of copper(II) complexes towards oxidation of potential bio-reductant L-ascorbic acid is of current interest for the construction of possible models for copper enzymes.

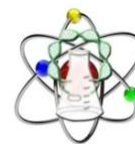
Conclusion

In this paper we have successfully demonstrated how rational design of a ligand system can bring about monometallic to di-metallic transition. These four metal ions form ink-blue complexes. Di- and polymetallic cadmium and mercury complexes are mostly obtained using chalcogenide as the bridging ligand. However, such examples involving extended organic ligand with bridging nitrogen atoms are rare. Moreover, the present work provides an opportunity to compare and contrast the chemistry of all three group-12 metal ions involving the polydentate nitrogen donor, HL¹. On the other hand, In the present cupric complexes, non-covalent hydrogen bonding interactions were observed in mono- and di-copper systems. Furthermore, redox behavior of the labile Cu₂- complex, **8** is noteworthy, it catalyses aerial oxidation of L-ascorbic acid which has bio-relevance. Moreover, these systems may be useful in extracting further insights into biochemical Cu₂-based O₂ activation processes.

References

1. S. Das, C. -H. Hung and S. Goswami; *Inorg. Chem.*, **2003**, 42, 5153.
2. (a) G. A. Crosby, R. G. Highland and K. A. Truesdell; *Coord. Chem. Rev.*, **1985**, 64, 41. (b) R. Ibrahim, S. Tsuchiya and S. Ogawa; *J. Am. Chem. Soc.*, **2000**, 122, 12174.
3. (a) M. Dakanali, E. T. Kefalas, C. P. Raptopoulou, A. Terzis, T. Mavromoustakos and A. Salifoglou; *Inorg. Chem.*, **2003**, 42, 2531. (b) M. C. Aragoni, M. Arca, F. Demartin, F. A. Devillanova, F. Isaia, A. Garau, V. Lippolis, F. Jalali, U. Papke, M. Shamsipur, L. Tei, A. Yari and G. Verani; *Inorg. Chem.*, **2002**, 41, 6623 and references therein. (c) F. A. Cotton, G. Wilkinson, A. A. Murillo and M. Bochmann; *Advanced Inorganic Chemistry*, John Wiley and Sons, Inc., New York, **1999**, 598. (d) R. H. Prince; In *Comprehensive Coordination Chemistry*; G. Wilkinson, R. D. Gillard and J. A. McCleverty; Eds.; Pergamon: Oxford, England, **1987**, Vol. 5, Chapter 56.1, p 925. (e) K. Brodersen and H. -U. Hummel; *Ibid*; Vol. 5, Chapter 56.2, p 1047.
4. A. T. Yordanov and D. M. Roundhill; *Coord. Chem. Rev.*, **1998**, 170, 93.
5. (a) J. B. King, M. R. Haneline, M. Tsunoda and F. P. Gabbaï; *J. Am. Chem. Soc.*, **2002**, 124, 9350. (b) P. Pykkö and M. Straka; *Phys. Chem. Chem. Phys.*, **2000**, 2, 2489. (c) P. Pykkö; *Chem. Rev.*, **1997**, 97, 597. (d) A. J. Canty and G. B. Deacon; *Inorg. Chim. Acta*, **1980**, 45, L225.
6. (a) G. Magesh, H. B. Singh, R. P. Patel and R. J. Butcher; *Inorg. Chem.*, **1998**, 37, 2663. (b) R. Lopez-Garzon, M. L. Godino-Salido, M. D. Gutierrez- Valero, P. Arranz- Mascaros and J. M. Moreno; *Inorg. Chim. Acta*, **1996**, 247, 203. (c) I. M. Vezzosi; *Polyhedron*, **1993**, 12, 2235. (d) N. Govindaswamy, J. Moy, M. Millar and S.A. Koch; *Inorg. Chem.*, **1992**, 31, 5343.
7. (a) U. Schöberl, T. F. Magnera, R. M. Harrison, F. Fleischer, J. L. Pflug, P. F. H. Schwab, X. Meng, D. Lipiak, B. C. Noll, V. S. Allured, T. Rudalevige, S. Lee and J. Michl; *J. Am. Chem. Soc.*, **1997**, 119, 3907. (b) E. García- España, J. Latorre, S. V. Luis, J. F. Miravet, P. E. Pozuelo, J. A. Ramírez and C. Soriano; *Inorg. Chem.*, **1996**, 35, 4591. (c) P. G. Lye, G. A. Lawrance, M. Maeder, B. W. Skelton, H. Wen and A. H. White; *J. Chem. Soc., Dalton Trans.*, **1994**, 793. (d) A. E. Mauro, S. H. Pulcinelli, R. H. A. Santos and M. T. P. Gambardella; *Polyhedron*, **1992**, 11, 799. (e) A. L. Spek, A. R. Siedle and J. Reedijk; *Inorg. Chim. Acta*, **1985**, 100, L15. (f) H. J. Callot, B. Chevrier and R. Weiss; *J. Am. Chem. Soc.*, **1979**, 101, 7729. (g) J. C. Dewan, D. L. Kepert and A. H. White; *J. Chem. Soc. Dalton Trans.*, **1975**, 490. (h) R. C. Elder, J. Halpern and J. S. Pond; *J. Am. Chem. Soc.*, **1967**, 89, 6877.
8. (a) A. Saha, A. K. Ghosh, P. Majumdar, K. N. Mitra, S. Mondal, K. K. Rajak, L. R. Falvello and S. Goswami; *Organometallics*, **1999**, 18, 3772. (b) B. S. Raghavendra and A. Chakravorty; *Indian J. Chem.*, **1976**, 14A, 166.
9. K. C. Kalia and A. Chakravorty; *J. Org. Chem.*, **1970**, 35, 2231.
10. K. K. Kamar, S. Das, C. -H. Hung, A. Castiñeiras, C. Rillo, M. Kuzmin and S. Goswami; *Inorg. Chem.*, **2003**, 42, 5367.
11. A. W. Addison, T. N. Rao, J. Reedijk, J. V. Rijn and G. C. Verschoor; *J. Chem. Soc., Dalton Trans.*, **1984**, 1349.

12. (a) F. -A. Yang, J. -H. Chen, H. -Y. Hsieh, S. Elango and L. -P. Hwang; *Inorg. Chem.*, **2003**, 42, 4603. (b) M. Fondo, A. Sousa, M. R. Bermejo, A. Garcia -Deibe, A. Sousa- Pedrares, O. L. Hoyos and M. Helliwell; *Eur. J. Inorg. Chem.*, **2002**, 703. (c) J. L. Sessler, T. Murai and V. Lynch; *Inorg. Chem.*, **1989**, 28, 1333.
13. J. E. Huheey, E. A. Keiter and R. L. Keiter, *Inorganic Chemistry*, 4th ed.; Harper Collins College: New York, **1993**; pp 114, 292.
14. (a) M. -C. Wang, L. -S. Sue, B. -C. Liao, B. -T. Ko, S. Elango and J. -H. Chen; *Inorg. Chem.*, **2001**, 40, 6064. (b) A. J. Canty, N. Chaichit, B. M. Gatehouse, E. E. George and G. Hayhurst; *Inorg. Chem.*, **1981**, 20, 2414. (c) A. J. Canty, N. Chaichit, B. M. Gatehouse and E. E. George; *Inorg. Chem.*, **1981**, 20, 4293.
15. (a) J. S. Casas, E. E. Castellano, M. S. Garcia- Tasende, A. Sanchez, J. Sordo, E. M. Vazquez- Lopez and J. Zuckerman- Schpector; *J. Chem. Soc., Dalton Trans.*, **1996**, 1973. (b) J. L. Atwood, D. E. Berry, S. R. Stobart and M. Zaworotko; *Inorg. Chem.*, **1983**, 22, 3480.
16. (a) D. C. Bebout, M. M. Garland, G. S. Murphy, E. V. Bowers, C. J. Abelt and R. J. Butcher; *Dalton Trans.*, **2003**, 2578 and references therein. (b) D. C. Bebout, D. E. Ehmann, J. C. Trinidad, K. K. Crahan, M. E. Kastner and D. A. Parrish; *Inorg. Chem.*, **1997**, 36, 4257.
18. G. Orellana, C. A. Ibarra and J. Santoro; *Inorg. Chem.*, **1988**, 27, 1025.
19. S. Choudhury, A. K. Deb and S. Goswami; *Polyhedron*, **1993**, 13, 1063.
20. S. Choudhury, M. Kakoti, A. K. Deb and S. Goswami; *Polyhedron*, **1992**, 11, 3183.
21. M. N. Ackerman, C. R. Barton, C. J. Deodene, E. M. Specht, S. C. Keill, W. E. Schreiber and H. Kim; *Inorg. Chem.*, **1989**, 28, 397.
22. W. Kaein and S. Kohlmann; *Inorg. Chem.*, **1987**, 26, 68.
23. A. K. Mahapatra, B. K. Ghosh, S. Goswami and A. Chakravorty; *J. Ind. Chem. Soc.*, **1986**, 53, 101.
24. E. V. Brown and G. R. Granneman; *J. Am. Chem. Soc.*, **1975**, 97, 621.
25. C. Mealli and D. M. Proserpio; *J. Chem. Educ.*, **1990**, 67, 399.
26. V. Lozan and B. Kersting; *Eur. J. Inorg. Chem.*, **2005**, 3, 504.
27. A. Sousa-Pedrares, J. Romero, J. A. Garcia-Vazquez, M. Luzduran, I. Casanova and A. Sousa; *Dalton Trans.*, **2003**, 1379.
28. P. R. Meehan, G. Ferguson, R. P. Shakyia and E. C. Alyea; *J. Chem. Soc., Dalton Trans.*, **1997**, 3487.
29. (a) C. D. Johnson, J. Feldmann, D. E. Macphee, F. Worrall and J. M. S. Shackle; *Dalton Trans.*, **2004**, 3611. (b) M. J. Plater, M. R. St., J. Foreman, T. Gelbrich, S. J. Coles and M. B. Hursthouse; *J. Chem. Soc., Dalton Trans.*, **2000**, 3065.
30. (a) M. Kontturi, E. Laurila, R. Mattsson, S. Peraniemi, J. J. Vepsalainen and M. Ahlgren; *Inorg. Chem.*, **2005**, 44, 2400. (b) R. D. Hancock, J. H. Reibenspies and H. Maumela; *Inorg. Chem.*, **2004**, 43, 2981. (c) R. March, J. Pons, J. Ros, W. Clegg, A. Alvarez-Larena, J. F. Piniella and J. Sanz; *Inorg. Chem.*, **2003**, 42, 7403. (d) J. B. King, M. Tsunoda and F. P. Gabbai; *Organometallics*, **2002**, 21, 2345.



STRUCTURAL AND THERMAL PROPERTIES OF Cu AND Co SUBSTITUTED $\text{Ni}_{46}\text{Mn}_{43}\text{Sn}_{11}$ FERROMAGNETIC SHAPE MEMORY ALLOYS

Rahul Das

Department of Physics, A. B. N. Seal College, Cooch Behar-736101, India.

Email: rahul04ph4004@gmail.com

ABSTRACT

A systematic study of structural and thermal properties of Cu and Co substituted $\text{Ni}_{46}\text{Mn}_{43}\text{Sn}_{11}$ ferromagnetic shape memory alloys synthesized by arc melting method has been reported in this work. Basically, change in free energy (ΔG), enthalpy (ΔE) and entropy (ΔS) at the first order structural transition from a high symmetric austenitic phase to a low symmetric martensitic phase in bulk off-stoichiometric Heusler alloys with compositions $\text{Ni}_{46}\text{Mn}_{43}\text{Sn}_{11}$, $\text{Ni}_{44}\text{Mn}_{43}\text{Cu}_2\text{Sn}_{11}$ and $\text{Ni}_{44}\text{Mn}_{43}\text{Co}_2\text{Sn}_{11}$ were investigated. The structural transition temperatures such as martensitic start temperature (T_{Ms}), martensitic finish temperatures (T_{Mf}), austenitic start temperatures (T_{As}), austenitic finish temperature (T_{Af}) of the parent ternary alloy shifts to lower temperatures upon Cu and Co substitution. All the alloys exhibited cubic $L2_1$ structure corresponding to the austenite phase at room temperature. The values of ΔG (ΔE and ΔS) are 163.8 Jkg^{-1} (6.9 kJkg^{-1} and $23.4 \text{ Jkg}^{-1}\text{K}^{-1}$), 166.2 Jkg^{-1} (7.7 kJkg^{-1} and $27.7 \text{ Jkg}^{-1}\text{K}^{-1}$) and 308.2 Jkg^{-1} (5.5 kJkg^{-1} and $26.8 \text{ Jkg}^{-1}\text{K}^{-1}$) for $\text{Ni}_{46}\text{Mn}_{43}\text{Sn}_{11}$, $\text{Ni}_{44}\text{Mn}_{43}\text{Cu}_2\text{Sn}_{11}$ and $\text{Ni}_{44}\text{Mn}_{43}\text{Co}_2\text{Sn}_{11}$ alloys, respectively. It can be seen that introducing either Cu or Co in the parent alloy leads to an increase in the ΔS and ΔG around the first order structural transition. It can also be noticed that lower ΔG at the structural phase transition result in smaller thermal hysteresis (ΔT_{hys}).

Introduction

Alloys based on Ni-Mn-Sn, belong to the new class of ferromagnetic shape memory alloys (FSMAs). These types of alloys are being intensively studied in recent years since they can exhibit room temperature martensitic structural transition from cubic austenite phase to orthorhombic martensite phase. Sutou *et al.* [SUTO04] established a phase diagram for the $\text{Ni}_{50}\text{Mn}_{50-x}\text{Sn}_x$ alloys displayed in Figure 1. In this alloy system, $\text{Ni}_{50}\text{Mn}_{37}\text{Sn}_{13}$ composition is particularly interesting because in this alloy both the second order magnetic phase transition at austenite phase as well as the first order martensitic structural phase transition occur around room temperature. The phase transition temperatures, structural, thermal and some other important physical properties including magnetocaloric effect (MCE) of the Ni-Mn-Sn alloys can be tailored by atomic substitution of elements such as Fe, Co, Cu, Cr etc. for Ni or Mn [FUKU09, PASS09, KREN07]. Ni-Mn-Sn based and its substituted alloys can experience three phase transitions: two second order magnetic phase transitions and one first-order martensitic structural phase transition. Krenke *et al.* [KREN05], reported that at the high temperature austenitic phase (above the austenitic Curie temperature, T_{CA}), the alloy is in paramagnetic phase and ferromagnetic phase when it is in below T_{CA} . With decreasing temperature, the martensitic structural phase transition takes place at T_{Ms} accompanied by a drop in magnetic moment (here magnetization) due to the increase in the proportion of the martensitic phase and the weakening (and ultimate disappearance) of the ferromagnetic behavior in the austenite phase. In the martensitic phase, if the temperature is further decreased, another second order magnetic transition occurs at martensitic Curie temperature (T_{CM}), the temperature at which the martensitic paramagnetic phase becomes martensitic ferromagnetic phase. In this report, a detailed study of the structural and thermal transitions as well as their related properties of Ni-Mn-Sn alloy influenced by the partial substitution of Co and Cu atoms for Ni is presented.

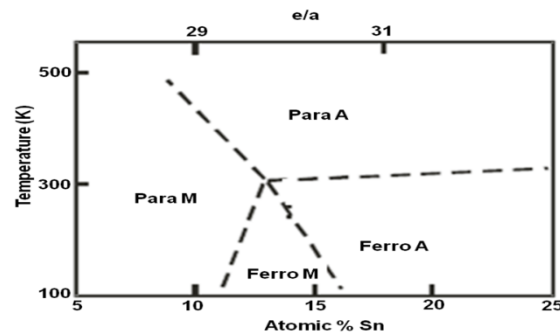


Fig. 1: Phase diagram of $Ni_{50}Mn_{50-x}Sn_x$ alloys, where Para, Ferro, A and M denote paramagnetic state, ferromagnetic state, austenitic phase and martensitic phase, respectively [SUTO04, BROW06].

Experimental

Polycrystalline $Ni_{44}(Co/Cu)_2Mn_{43}Sn_{11}$ alloy ingots were prepared by arc melting method followed by homogenization under a vacuum pressure of 10^{-3} Pa at 1273 K for 24 h and quenching in ice water. The overall composition of the master alloys was measured by energy dispersive spectrometer (EDS, Oxford) attached to a scanning electron microscope (SEM, Leo 1430 VP). In this case, the EDS results are the mean value of at least three independent observations. The final alloy composition was nearly the same as the nominal (starting) composition of the respective alloys (Table 1).

Table 1: The overall measured composition of $Ni_{44}(Co/Cu)_2Mn_{43}Sn_{11}$ alloys.

Nominal Composition	Measured Composition
$Ni_{46}Mn_{43}Sn_{11}$	$Ni_{45.95}Mn_{43.12}Sn_{10.93}$
$Ni_{44}Mn_{43}Co_2Sn_{11}$	$Ni_{43.50}Mn_{43.33}Co_{2.21}Sn_{10.96}$
$Ni_{44}Mn_{43}Cu_2Sn_{11}$	$Ni_{43.88}Mn_{42.95}Cu_{2.14}Sn_{11.03}$

X-ray diffractometer (Seifert 3003 T/T) and differential scanning calorimeter (DSC, PerkinElmer DSC 7) were used for structural and thermal characterization.

Results and discussion

X-ray diffraction (XRD) patterns for $Ni_{46}Mn_{43}Sn_{11}$, $Ni_{44}Mn_{43}Co_2Sn_{11}$ and $Ni_{44}Mn_{43}Cu_2Sn_{11}$ alloys recorded at room temperature are shown in Figure 2. The structural data extracted from these XRD patterns are listed in Table 2. All the diffraction peaks in the XRD patterns of all the alloys could be indexed to $L2_1$ cubic structure corresponding to the austenite phase. Lattice parameters ($a = b = c$) of $Ni_{46}Mn_{43}Sn_{11}$, $Ni_{44}Mn_{43}Co_2Sn_{11}$ and $Ni_{44}Mn_{43}Cu_2Sn_{11}$ alloys are 0.5929 ± 0002 nm, 0.5978 ± 0003 nm, and 0.5922 ± 0001 nm, respectively. The small increase (decrease) in lattice parameter and unit cell volume with Co (Cu) substitution for Ni may be attributed to slight differences in the atomic radii of Co and Cu with respect to that of Ni.

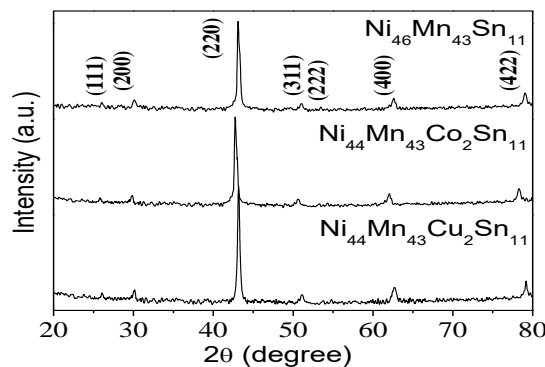
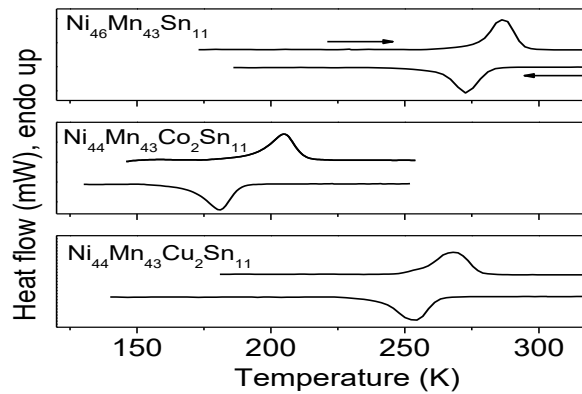


Fig. 2: Room temperature X-ray diffraction patterns for $Ni_{46}Mn_{43}Sn_{11}$, $Ni_{44}Mn_{43}Co_2Sn_{11}$ and $Ni_{44}Mn_{43}Cu_2Sn_{11}$ alloys.

Table 2: Crystal phase, lattice parameters (a , b , c) and unit-cell volume of $\text{Ni}_{44}(\text{Co/Cu})_2\text{Mn}_{43}\text{Sn}_{11}$ alloys.

Alloy	Crystal phase	a (nm)	b (nm)	c (nm)	Unit-cell volume (nm ³)
$\text{Ni}_{46}\text{Mn}_{43}\text{Sn}_{11}$	Austenite	0.5929	0.5929	0.5929	0.2084
$\text{Ni}_{44}\text{Mn}_{43}\text{Co}_2\text{Sn}_{11}$	Austenite	0.5978	0.5978	0.5978	0.2136
$\text{Ni}_{44}\text{Mn}_{43}\text{Cu}_2\text{Sn}_{11}$	Austenite	0.5922	0.5922	0.5922	0.2077

DSC data corresponding to $\text{Ni}_{46}\text{Mn}_{43}\text{Sn}_{11}$, $\text{Ni}_{44}\text{Mn}_{43}\text{Co}_2\text{Sn}_{11}$ and $\text{Ni}_{44}\text{Mn}_{43}\text{Cu}_2\text{Sn}_{11}$ alloys are plotted in Figure 3. The direct and reverse martensitic phase transformations are accompanied by well-defined exothermic and endothermic peaks. From these DSC curves, it is easy to find out the characteristic temperatures of the direct (T_{Ms} and T_{Mf}) and the reverse (T_{As} and T_{Af}) martensitic transition. The values of the martensitic structural characteristic temperatures obtained for different alloy compositions from the DSC plot are displayed in Table 3.

**Fig. 3:** DSC plots of $\text{Ni}_{46}\text{Mn}_{43}\text{Sn}_{11}$, $\text{Ni}_{44}\text{Mn}_{43}\text{Co}_2\text{Sn}_{11}$ and $\text{Ni}_{44}\text{Mn}_{43}\text{Cu}_2\text{Sn}_{11}$ alloys.**Table 3:** Martensitic start temperature (T_{Ms}), martensitic finish temperatures (T_{Mf}), austenitic start temperatures (T_{As}), austenitic finish temperature (T_{Af}), thermal hysteresis (ΔT_{hys}), change in total enthalpy (ΔE), change in total entropy (ΔS) and change in free energy (ΔG) of $\text{Ni}_{44}(\text{Co/Cu})_2\text{Mn}_{43}\text{Sn}_{11}$ alloys estimated from DSC data.

Alloy	T_{Ms} (K)	T_{Mf} (K)	T_{As} (K)	T_{Af} (K)	ΔT_{hys} (K)	ΔE (kJkg ⁻¹)	ΔS (Jkg ⁻¹ K ⁻¹)	ΔG (Jkg ⁻¹)
$\text{Ni}_{46}\text{Mn}_{43}\text{Sn}_{11}$	292	240	259	299	13.0	6.9	23.4	163.8
$\text{Ni}_{44}\text{Mn}_{43}\text{Co}_2\text{Sn}_{11}$	194	157	178	217	22.0	5.5	26.8	308.2
$\text{Ni}_{44}\text{Mn}_{43}\text{Cu}_2\text{Sn}_{11}$	273	225	245	283	15.0	7.7	27.7	166.2

Using the DSC data, the ΔG , ΔE and ΔS have been estimated for the $\text{Ni}_{44}(\text{Co/Cu})_2\text{Mn}_{43}\text{Sn}_{11}$ alloys. The obtained values of ΔG (ΔE and ΔS) are 163.8 Jkg⁻¹ (6.9 kJkg⁻¹ and 23.4 Jkg⁻¹K⁻¹), 308.2 Jkg⁻¹ (5.5 kJkg⁻¹ and 26.8 Jkg⁻¹K⁻¹) and 166.2 Jkg⁻¹ (7.7 kJkg⁻¹ and 27.7 Jkg⁻¹K⁻¹) for $\text{Ni}_{46}\text{Mn}_{43}\text{Sn}_{11}$, $\text{Ni}_{44}\text{Mn}_{43}\text{Co}_2\text{Sn}_{11}$ and $\text{Ni}_{44}\text{Mn}_{43}\text{Cu}_2\text{Sn}_{11}$ alloys, respectively. It can be observed that introducing either Co or Cu in the parent alloy leads to an increase in the ΔS and ΔG around the martensitic first order structural transition. It can also be noticed that lower ΔG at the martensitic phase transition result in smaller thermal hysteresis, $\Delta T_{hys} [= (T_{As} + T_{Af})/2 - (T_{Ms} + T_{Mf})/2]$ which are 13 K, 22 K and 15 K for $\text{Ni}_{46}\text{Mn}_{43}\text{Sn}_{11}$, $\text{Ni}_{44}\text{Mn}_{43}\text{Co}_2\text{Sn}_{11}$ and $\text{Ni}_{44}\text{Mn}_{43}\text{Cu}_2\text{Sn}_{11}$ alloys, respectively.

Conclusions

In this work, structural and thermal properties of the arc melted polycrystalline $\text{Ni}_{44}(\text{Co/Cu})_2\text{Mn}_{43}\text{Sn}_{11}$ alloy ingots have been investigated. All the alloys show evidence of cubic $L2_1$ structure corresponding to the austenite phase at room temperature. Slight increase (decrease) in lattice parameter and unit cell volume was observed when Co (Cu) was partially substituted for Ni. Introducing either of these elements leads to an increase in the area under thermal hysteresis around the structural transition. These studies establish a procedure

for tailoring both the properties structural and thermal in Ni-Mn-Sn alloys by Co and Cu substitution. Not only the structural and thermal properties but also some other important physical properties including magneto caloric effect of the Ni-Mn-Sn alloys can be tailored by atomic substitution of elements (Fe, Co, Cu, Cr etc. for Ni or Mn) which provides the alloys suitable for applications such as magnetic sensors, actuators and magnetic refrigeration.

Acknowledgements

I am very much thankful to Dr. A. Srinivasana, Professor of Indian Institute of Technology Guwahati for his support, cooperation and lab facilities.

References

- [BROW06] Brown P J, Gandy A P, Ishida K, Kainuma R, Kanomata T, Neumann K U, Oikawa K, Ouladdiaf B and Ziebeck K R A, J. Phys.: Condens. Matter 18 (2006) 2249.
- [FUKU09] Fukushima K, Sano K, Kanomata T, Nishihara H, Furutani Y, Shishido T, Ito W, Umetsu R Y, Kainuma R, Oikawa K and Ishida K, Scr. Mater. **61** (2009) 813.
- [KREN05] Krenke T, Acet M, Wassermann E F, Moya X, Mañosa L and Planes A. Phys. Rev. B 72 (2005) 014412.
- [KREN07] Krenke T, Duman E, Acet M, Moya X, Mañosa L and Planes A, J. Appl. Phys. 102 (2007) 033903.
- [PASS09] Passamani E C, Xavier F, Favre-Nicolin E, Larica C, Takeuchi A Y, Castro I L and Proveti J R, J. Appl. Phys. 105 (2009) 033919.
- [SUTO04] Sutou Y, Imano Y, Koeda N, Omori T, Kainuma R, Ishida K and Oikawa K Appl. Phys. Lett. 85 (2004) 4358.

SOLID PHASE CRYSTALLIZATION (SPC) OF NANOCRYSTALLINE SILICON (nc-Si:H) FILMS: CHANGES IN STRUCTURAL AND OPTICAL PROPERTIES

Romyani Goswami

Dept. of Physics, Surya Sen Mahavidyalaya, Surya Sen Colony, Block – B
Siliguri – 734004, E-mail: romyanieru@gmail.com

ABSTRACT

Solid Phase Crystallization of hydrogenated nanocrystalline silicon films (nc-Si:H) deposited by radio frequency plasma enhanced chemical vapor deposition (RF-PECVD) and annealed at 600°C in a vacuum furnace has been investigated. The structural and optical properties are studied for the as deposited nanocrystalline films. The effects of variation of deposition power on the properties of nanocrystalline (initial) and crystallized (after annealing) films have been investigated. The dependence of the structure of the crystallized films on the properties of as deposited films has been studied. It has been observed that the surface morphology of the crystallized films obtained by scanning electron microscopy is highly influenced by the bonded hydrogen content of the as deposited nanocrystalline films. It is also observed that the rate of crystallization during annealing is much faster for nc-Si films than a-Si. X-ray diffraction study, Raman spectroscopy and Transmission electron microscopy reveal formation of smooth, large grained crystallized silicon films by Solid Phase Crystallization of nanocrystalline films deposited at medium plasma power regime.

Keywords: Nanocrystalline silicon, Crystallization, Structural properties

Introduction

There is a current interest in fabricating high quality polycrystalline silicon films on standard, inexpensive glass substrate for application to large area solar cells and other microelectronic and flat panel display technologies. Intrinsic microcrystalline silicon thin films nowadays are being widely used as the main absorber or active layer (i layer) of solar cells. The serious drawback of the microcrystalline layer in device application is its low deposition rate because several micrometer thick microcrystalline films are needed for sufficient light absorption. Another alternative method to get large grain silicon layer is crystallization of amorphous silicon (a-Si) material having high growth rate. Polycrystalline films after crystallization possess not only a large crystalline grain and reduced density of grain boundary but also include a smoother surface morphology and higher conductivity. There are various methods of crystallization of a-Si among which the most promising is solid phase crystallization (SPC). It is a simple and cost effective process by which comparatively thick amorphous silicon thin films can be crystallized by thermal annealing in a conventional furnace. The structure of SPC grown polysilicon films from undoped amorphous silicon is reported previously by many authors. In this work solid phase crystallization process is done on nanocrystalline Si:H films which are often called the “edge” of a-Si:H [1]. The as deposited nc-Si:H films are the transition materials between amorphous and microcrystalline Si:H and it has the phase just before the formation of microcrystalline grains. In this work initial nanocrystalline films are deposited by PECVD process at high pressure with fixed hydrogen dilution ratio but varying the deposition power from 10 W to 150 W and the structural and optical changes in nanocrystalline silicon films after solid phase crystallization are investigated. The dependence of the structure of crystallized films on the microstructure of the as deposited films is also studied.

Experimental Results

The structural studies of as deposited and annealed films have been done by X-ray diffraction. Figure 1a and 1b show the X-ray diffraction profiles of the nanocrystalline silicon films before and after SPC respectively. In this figure the XRD spectra are shown for the film deposited at 10 W, 40 W, 80 W, 130 W and 150 W RF power. No sharp diffraction peak is observed for the as deposited films but the broad hump at around 28° and

45° to 60° indicates that there is a tendency of crystallization and the films are not completely amorphous. All films annealed at 600°C exhibit diffraction peaks at 2θ values of 28.4°, 47.3° and 56.2°, which correspond to (111), (220) & (311) silicon planes respectively in which (111) peak is the most intense.

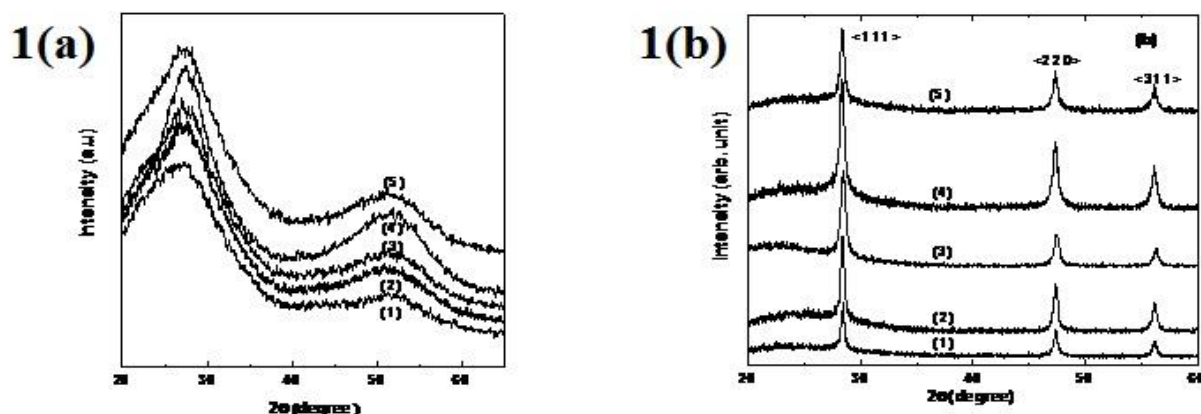


Fig. 1: (a) X-ray diffraction spectra of nanocrystalline silicon films deposited at (1) 10 Watt, (2) 40 Watt, (3) 80 Watt, (4) 130 Watt and (5) 150 Watt plasma power; (b) XRD spectra of annealed films with power (1) 10 W, (2) 40 W, (3) 80 W, (4) 130 W and (5) 150 W.

In order to investigate the structural nature of the as-deposited and annealed films, Raman spectroscopy is done.

Figure 2 shows the Raman spectra of the as-deposited samples and samples after SPC. Curves (a), (b) and (c) represent the Raman spectra of as-deposited films at 130 Watt, 80 Watt and 40 Watt RF power respectively and the curves (d), (e) and (f) show Raman spectra of the same films after SPC. The peak corresponding to transverse optical (TO) mode around 480 cm^{-1} of the as-deposited film which corresponds to the amorphous phase. After SPC, the broad band attributed to amorphous component almost disappears and mainly a sharp peak around 520 cm^{-1} remains for all samples which correspond to the crystalline silicon TO phonon mode.

To calculate the crystalline volume fraction of the films after SPC all the Raman peaks after SPC are deconvoluted into three peaks around 480 cm^{-1} , 510 cm^{-1} and 520 cm^{-1} . The crystalline volume fraction X_c has been estimated from the Raman spectra by the following formula,

$$X_c = I_c / (I_c + I_b + I_a)$$

Where, I_c , I_b and I_a are the integrated intensity of peak around 520 cm^{-1} which corresponds to crystalline silicon peak, 510 cm^{-1} which corresponds to grain boundary peak and 480 cm^{-1} which corresponds amorphous silicon peak respectively. Very small volume fraction of crystallinity (X_c) is observed from Raman spectra of the as deposited nanocrystalline films by deconvoluting the curves (a), (b) and (c) into two curves around 480 cm^{-1} and 520 cm^{-1} . The values of X_c for these nanocrystalline films are given in Table 1. Sharp crystalline peaks are observed with a less amorphous component for all the films after annealing. The crystalline volume fraction of films after crystallization is also shown in this table. It is observed that the films deposited at medium power are better crystallized than that at lower and higher power.

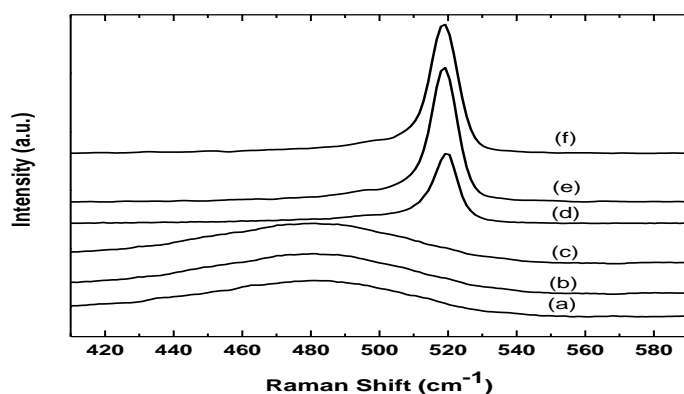


Fig. 2: Raman Spectra of as-deposited and annealed films with (a), (b), (c) as deposited films at 130 Watt, 80 Watt and 40 Watt and (d), (e), (f) annealed films at 130 Watt, 80 Watt and 40 Watt.

The bonding configurations of Si and H in the silicon films can be determined by fourier transform infrared spectroscopy.

FTIR spectra of the as deposited nanocrystalline films are investigated in the range of 400-4000 cm^{-1} where all the films show a prominent peak centered near 2000 cm^{-1} corresponding to Si:H stretching mode. Generally the peak at 2000 cm^{-1} is attributed to the monohydride bonding of silicon [Si-H] and the peak at 2100 cm^{-1} corresponds to di- or polyhydride bonding of silicon [Si-H₂, (SiH₂)_n]. The microstructure factor [$R = I_{2100}/(I_{2000} + I_{2100})$] has been calculated from the ratio of integrated intensity under the deconvoluted curves at 2000 cm^{-1} and 2100 cm^{-1} . The peak positions and values of R are given in Table 1. The bonded hydrogen content (C_H in atomic %) of the as deposited silicon films have been calculated from the integrated infrared absorption (α) of the peak corresponding to rocking-wagging mode of silicon hydrogen bonding around 630-640 cm^{-1} and the values are also given in Table 1. It is observed that C_H is lower in the films deposited at lower power and increases as RF power increases. Value of C_H is 6.6 - 8.6 at atomic % for 10-80 Watt deposited films whereas the value is 17.5-18.5 at atomic % for 130-150 Watt deposited films. A shift of peak position of the stretching band is shown in Table 1. The position of the 2000 cm^{-1} peak changes with increased hydrogen concentration of the films. All the nanocrystalline films show dominating peak at 2000 cm^{-1} with very low contribution from 2100 cm^{-1} , as we can see from the low value of microstructural factor. We can say that we have deposited dense, void free films initially. It is interesting to note that even at high power deposited films where C_H is high R is low.

After annealing, each sample has been analyzed again by FTIR spectroscopy. No peak has been observed in the IR spectra of the annealed films. The peak observed at 2000 cm^{-1} for the as deposited films disappears after annealing the films at 600 °C. The bonded hydrogen content is negligible for the films after SPC. As expected hydrogen diffusion takes place where the films are annealed near 600°C. The samples deposited at low power (10-40 watt) have smooth surface after effusion of hydrogen from the surface of the film due to annealing but the surface becomes very rough for those samples deposited at high power. The sample deposited at 150 Watt is partly peeled off. Thus we obtain uniform, smooth, damage free crystallized films deposited at low power region after solid phase crystallization.

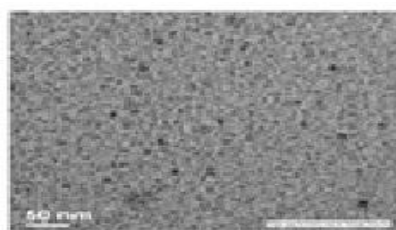
Table 1: Structural properties of as deposited nanocrystalline silicon films and films after SPC deposited at different deposition power.

Power (Watt)	X_c (Before SPC) (%)	X_c (After SPC) (%)	Peak position of IR stretching mode of as-deposited films	Micro structural factor R of as-deposited films	C_H (at%) of as-deposited films
10	2.83	81.1	1994.2	0.016	6.6
40	5.01	89.8	2003.9	0.184	8.0
80	2.53	88.9	2003.9	0.125	8.6
130	1.67	83.2	2005.8	0.121	17.5
150	0.96	82.5	2007.7	0.108	18.5

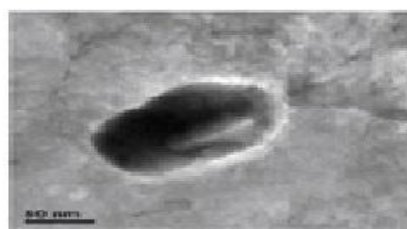
In order to study the structural nature of the annealed films more thoroughly, high resolution TEM (HRTEM) measurements are performed. Figure 3a and 3b shows bright field plane view Transmission Electron micrographs of the sample deposited at 40 Watt before and after SPC respectively. It is very clear from the images that larger grain growth occurs due to annealing at 600 °C whereas very small sized grains are observed before annealing in the sample. Figure 3c shows the TEM micrograph of sample deposited at 80 Watt after SPC. A wide distribution of circular and elliptical grains are observed having grain size between 67 nm to 130 nm. The most interesting feature in this micrograph is the elliptical shape of the crystallites.

From the TEM micrograph of Figure 3b, it is observed that the grain is approximately ellipsoidal in shape. By measuring the length along the two main axes (a,b) of this ellipsoidal and assuming that the area of the ellipsoid is equal to a square of side g, we can find out the grain size as given below

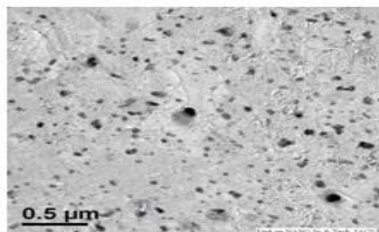
$$g = (\pi ab)^{1/2}/2$$



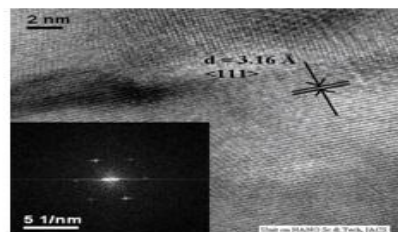
(a) Power= 40 Watt before SPC



(b) Power= 40 Watt after SPC



(c) 80 Watt after SPC



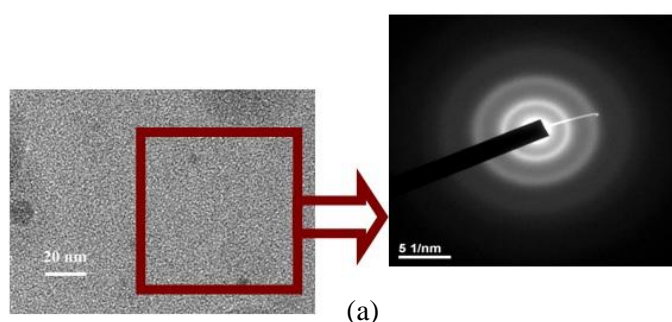
(d) High Resolution TEM image of film deposited at 40 Watt after crystallization

Figure 3d shows the high resolution TEM image (HRTEM) of annealed film deposited at 40 Watt in which the lattice spacing is clearly identified. The interplanar spacing d is calculated from the lattice

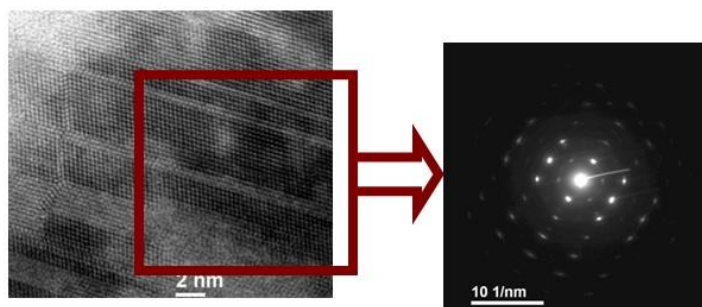
Fig. 3: Transmission Electron Micrograph of silicon films

image. Comparing the d value with JCPDS data the crystalline plane can be recognized. In Figure 3d the value of $d = 3.16 \text{ \AA}$ which corresponds to (111) plane. From the FFT (Fast Fourier Transform) image shown in the inset of Figure 3d the value of d is calculated which 3.12 \AA . This also indicates the (111) orientation.

The crystallization of silicon films by furnace annealing can be very clearly viewed by the high resolution TEM images and selected area diffraction (SAD) patterns. Figures 4a and b show the HRTEM image of as-deposited and annealed samples deposited with 40 W and the corresponding diffraction image. The square box indicates the selected area in the sample for diffraction. The diffused rings in the transmission electron diffraction (TED) pattern in figure 4a reveals the absence of crystallites before SPC, whereas the clear lattice planes as well as the presence of bright spots in the TED pattern in the annealed film as depicted in figure 6.5b implies complete crystallization of the film.



(a)



(b)

Fig. 4: HRTEM and corresponding SAD pattern of 40 W deposited film (a) before SPC and (b) after SPC.

Figure 5 shows a high resolution transmission electron micrograph of the film after annealing deposited initially at 40 W, enlighten heavily twinned structure in a typical crystallized region. The microtwin lines are clearly visible in the grain as denoted by a letter 'T'. The portion of the grain surrounded by white rectangle in the figure has been magnified and shown in the inset of the image. On both side of the microtwin, periodic (111) planes have clearly seen. Actually, in the solid phase crystallization process from a-Si to polycrystalline silicon thin film,

compressive stresses arise in the amorphous films due to the mismatch of thermal expansion coefficients between the film and the substrate. Again tensile stress may be induced in the films as the crystallization

proceeds since the amorphous to crystalline transition is accompanied by a volume contraction. To relieve these stresses, two dimensional crystalline defects such as microtwins, stacking faults etc. and one dimensional crystalline defect such as dislocation develop during the nucleation stage and the growth stage of the crystal. Studies on the crystallization of amorphous semiconductor thin films strongly suggest that lattice defects, such as twins, play an important role in the growth of the crystalline plane. Csepregi et al. [2] have shown that the presence of twins can accelerate silicon crystal growth. It is observed from the micrograph that the grains have a dendritic appearance with preferred growth direction as indicated by the black arrow marks in Fig. 5. Introduction of microtwins (T) facilitates growth in the arrow directions by providing favorable atomic sites for atom attachment. The inset of the figure shows the SAED pattern of the film. Regular and symmetrical arrangement of bright spots attributed to perfect polycrystalline silicon growth. The identification of the lattice planes have been done from the SAED pattern resulting (111), (220) and (311) lattice planes. In our work all the three peaks have been observed by X-ray diffraction study for the annealed films

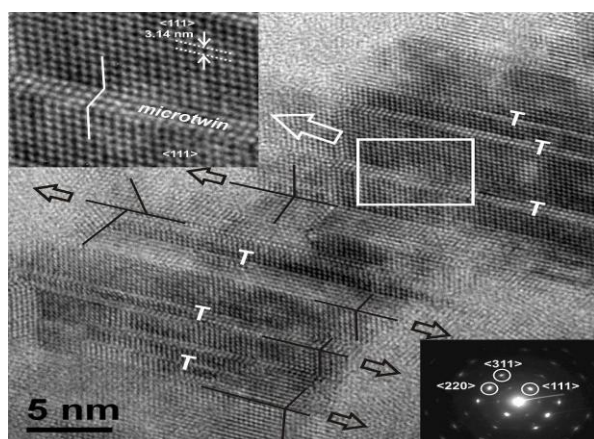
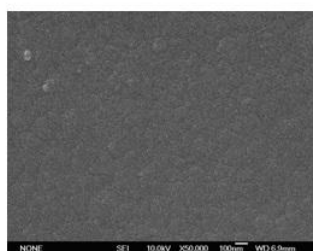
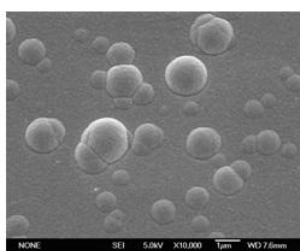


Fig. 5: High resolution transmission electron micrograph of heavily twinned structure in a crystallized region of Si:H film after annealing deposited initially at

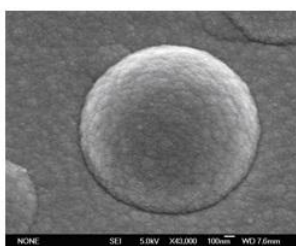
Surface morphologies of the films have been studied using scanning electron microscopy before and after annealing. The as deposited samples having thickness of 1 μm to 1.5 μm show the same featureless surface morphology typical of amorphous silicon. But there is considerable change in the surface structure of the films after annealing. Figure 6a and 6b show the surface morphology of same sample deposited at 40 Watt before and after SPC. It is seen from the micrographs that before annealing almost no grain growth occurs in the surface of the film whereas after annealing a large number of spherical grains (1 to 2 μm) are randomly distributed all over the surface.



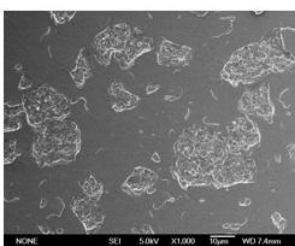
(a) Power= 40 Watt before annealing



(b) Power=40 Watt and annealed at 600 °C for 6 hrs



(c) Individual grain of 40 Watt annealed film



(d) 80 Watt annealed film

Figure 6c shows an individual grain which contains a large number of small spherical grains of average diameter ~ 80 nm to 100 nm coagulating with each other to form the large grain. Annealing degrades the surface of the films which are initially deposited at higher power. Annealing degrades the surface of the films which are initially deposited at higher power (≥ 80 W). The films deposited at high power show damage surface after SPC with large number of craters (Fig. 6d).

Fig. 6: Scanning Electron Micrograph of silicon films.

Optical absorption α is determined for both the as deposited (nanocrystalline) and annealed (polycrystalline) films deposited at different powers. Figure 7 shows the absorption characteristics of silicon films against photon energy $h\nu$ deposited at 40 Watt before and after SPC. It is clearly seen from the figure that the nature of variation of α change drastically in case of the annealed samples in comparison to the unannealed films. Two distinct regions are shown from the absorption curve: Below 2 eV, the absorption increases after annealing. Before annealing α at 1.55 eV was $3.3 \times 10^3 \text{ cm}^{-1}$, whereas after annealing α at 1.6 eV becomes $1.1 \times 10^4 \text{ cm}^{-1}$. Above 2 eV region, optical absorption coefficient is higher for the as deposited silicon films than the annealed films. The large value of absorption coefficient of as deposited films is mainly due to amorphous phase.

The optical band gap E_g^{opt} is estimated by Tauc's relation $\alpha h\nu \sim (h\nu - E_g^{\text{opt}})^2$ from high absorption region ($\alpha \sim 10^4$). The optical band gap of the samples before annealing is 1.68 eV for film deposited at 40 Watt, which corresponds to the nanocrystalline silicon material compare with others data. After solid phase crystallization optical band gap of the first sample becomes 1.12 eV, which is similar to the value of indirect gap of crystalline silicon. Thus it is observed that the annealing shifts the absorption edge closer to the crystalline silicon phase.

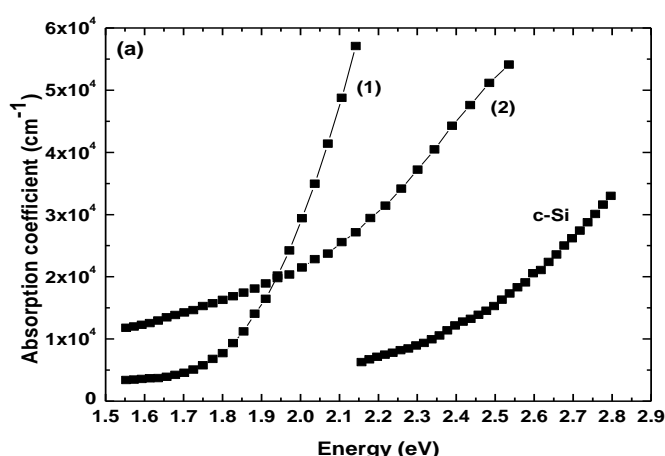


Fig. 7: Optical absorption spectra of silicon films deposited at 40 Watt in which (1) as deposited and (2) annealed film.

Discussions

The initial as deposited films deposited at high growth rate are nanocrystalline in nature that has the phase at the threshold of crystallinity. The XRD spectra of the as deposited films indicate different nature from the typical x-ray peak of a-Si. For amorphous silicon a broad hump is usually observed in XRD. From the Raman spectra of the as deposited films very small fraction of crystallinity is obtained which satisfies the nanocrystalline nature of the films. TEM images of the as deposited films confirm the presence of very small crystalline grains of average diameter 2.5-8 nm embedded in the amorphous structure. The size and volume fraction of these crystallites are too low to be detected by Raman spectroscopy. It may also be noted that microstructure factors (R) of these nanocrystalline films are much lower compared to that of microcrystalline silicon films indicating more compact and void free network.

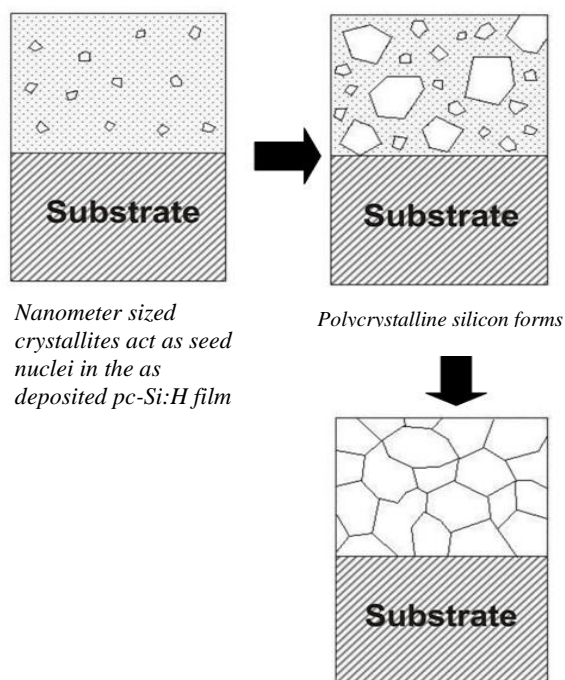
Solid phase crystallization of amorphous silicon is basically a first order phase transition from amorphous to polycrystalline phase. It involves two distinct processes, the nucleation of seeds, which are often called the “jerm nuclei” and their growth to become larger “growth nuclei” which are the grains of polycrystalline silicon. Both processes are thermally activated. Due to thermal annealing the whole covalently bonded random network of a-Si rearranges in such a manner that the free energy of the final phase should be less than the free energy of previous random phase. This is called “structural relaxation” which is very slow process. During annealing the tetrahedral bond angle deviation $\delta\theta$ of a-Si decreases and short range order improves and hence crystallization occurs. The rate of crystallization = nucleation rate + grain growth rate. This type of homogeneous crystallization leads to a progressive conversion of as deposited Si:H material into a polycrystalline form, as depicted in figure 8. As the crystal lattices of individual crystallites or “grains” do not mach up perfectly at the grain boundaries, a polycrystalline nature is formed. The final grain size $d \propto [v_g / N]^{1/3}$, according to the theoretical calculation of Iverson and Reif et al. [3] where N is the nucleation rate and v_g is the grain growth rate.

From several reports on the crystallization time and crystallization temperature it is obvious that at an annealing temperature of 600 °C, undoped amorphous silicon film requires much high annealing time of the order of 20-100 hrs [4]. But in this work, SPC of nanocrystalline silicon takes much less time i.e. only 6 hrs. The structural study of intrinsic nanocrystalline silicon reveals that there already exist a large number of tiny grains of average diameter 5-8 nm in these films which are treated as the “seed” nuclei.

Thus crystallization comprises only the growth process from these seeds and crystallization of nc-Si occurs faster than a-Si. In another aspect we can say that as the nanocrystalline silicon has improved short range order i.e. less bond angle deviation in its atomic structure, the enhancement of long range order by thermal annealing is much faster than a-Si. The surface morphology of the samples after annealing at 600 °C for 6 hrs is related to their initial (before annealing) bonded hydrogen content. It is shown very clearly from the SEM images and the bonded hydrogen content (C_H) values of the as deposited samples that the surface damages occur for samples having higher initial hydrogen concentration. Above 80 W all the samples have higher initial hydrogen content, thus massive hydrogen effusion occurs during annealing which creates surface damage for those samples as we can see from the scanning electron micrographs. The optical absorption spectra of the silicon films after solid phase crystallization show similar variation as that of c-Si although α values are high.

Conclusions

Nanocrystalline silicon films have been prepared using high chamber pressure and RF power by PECVD method. The phase change of nanocrystalline silicon to polycrystalline silicon is realized by solid phase



crystallization process. All the films are highly crystalline after SPC having volume fraction of crystallinity (X_c) varies from 81 % to 90 %. After SPC, the large crystalline grain of grain size ~102 nm (from TEM), highest volume fraction of crystallinity ~ 90 % and dark conductivity of 10^{-4} Scm^{-1} have been obtained in the film deposited at 40 W deposition power. For this sample deposition rate is ~ 0.5 nm/sec. It is very interesting to note that the rate of crystallization of the nc-Si films due to annealing is higher than that of a-Si. The low bonded hydrogen content (6.6-8 at. %) in 10 and 40 W deposited film is suitable to avoid massive hydrogen evolution during SPC. The films deposited at high power (> 80 W) have large hydrogen content. The rigorous effusion of hydrogen during SPC causes extensive surface damage to the films. It is observed from scanning electron micrographs that no surface damage occurs for films deposited at 10 and 40 W after SPC. Thus we obtain large grained, smooth, crystallized silicon films with considerable growth rate (~ 0.5 nm/sec) by solid phase crystallization using an optimum deposition power which is 40 W in this case.

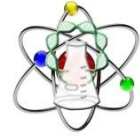
Fig.8: Crystallization kinetic of the polycrystalline silicon film by solid phase crystallization of the as deposited film.

Acknowledgement

The author is grateful to Prof. Swati Ray, Energy Research Unit, Indian Association for the Cultivation of Science, Jadavpur, Kolkata for giving the facility of the research work.

References

- [1] C. R. Wronski, J. M. Pearce, J. Deng, V. Vlahos, R. W. Collins, Thin Solid Films 451-452 (2004) 470.
- [2] L. Csepregi, J. W. Mayer and T. W. Sigmon, Appl. Phys. Lett. 29 (1976) 92.
- [3] R. B. Iverson and R. Reif, J. Appl. Phys. 62 (1987) 1675.
- [4] X. Zheng Bo, N. Yao, S. R. Shieh, T. S. Duffy and J. C. Sturm, J. Appl. Phys. 91 (2002) 2910.



MHD NATURAL CONVECTION OVER A MELTING HORIZONTAL PLATE IN POROUS MEDIUM SATURATED WITH A FLUID OF VARIABLE VISCOSITY

Rishi Raj Kairi

Department of Mathematics, Islampur College, Uttar Dinajpur, West Bengal-733202, India.

Email: rishirajkairi@gmail.com

ABSTRACT

The MHD natural convection heat and mass transfer over a melting horizontal plate embedded in a porous medium saturated with a fluid of variable viscosity is investigated in this paper. The plate and ambient medium are maintained at constant but different levels of temperature and concentration such that heat and mass transfer occurs from the wall to the medium. The Reynolds viscosity model is used to characterize the viscosity of the fluid. A similarity solution for the transformed equations is obtained. The numerical computation is carried out for various values of the flow, temperature and concentration influencing characteristics. The effect of radiation, viscosity, thermo-diffusion (Soret effect) and melting in presence of magnetic field on the temperature and concentration field as well as on the heat and mass transfer coefficients is analyzed. It is noticed that the effect of thermo-diffusion parameter on the heat and mass transfer coefficients reduces with increasing value of the melting parameter. The reduction in heat and mass transfer due to melting phenomenon in the porous medium is influenced by viscosity parameter. It is also evident that the combined effects of melting and Soret effect are prominent in presence of radiation.

Keywords: Natural convection, Soret effect, melting, radiation, magnetic field, Porous medium.

Introduction

The study of convection heat and mass transfer in a porous medium has wide range of applications in geophysics and energy related problems such as thermal insulation, enhanced recovery of petroleum resource, geophysical flows, polymer processing in packed beds and sensible heat storage bed. The second order effects like melting, radiation, thermo-diffusion (Soret effect), variable viscosity and magnetic field are important phenomena coupled convection in porous media. A lot of heat and mass convection studies in porous media have been reported by researchers [1-14] with considering different second order effects. Understanding the collective consequence of second order effects on double diffusive convection of heat and mass in porous media is very crucial due to their huge practical applications.

The main purpose of this present investigation is to illustrate the effect of radiation and Soret effect on MHD natural convection heat and mass transfer over a melting horizontal plate in a non-Darcy porous medium saturated with a fluid of variable viscosity, using the similarity solution technique.

Mathematical Formulation

Consider the steady two-dimensional laminar boundary layer flow over a horizontal plate embedded in a saturated porous medium. The fluid is considered to be gray, absorbing-emitting radiation but non-scattering medium, and the Rosseland approximation is used to describe the radiative heat flux in the energy equation. The physical model and the co-ordinate system are shown in the Figure 1. The x -coordinate is taken along the plate, the y -coordinate is measured normal to the plate, while the origin of the reference system is taken at the leading edge of the plate. A transverse magnetic field of strength B_0 is imposed.

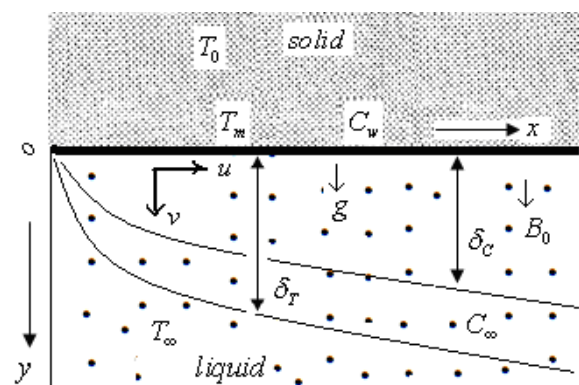


Fig. 1: Physical Model and coordinate system (Kairi[14])

The plate is at a constant temperature T_m at which the material of the porous matrix melts. The liquid phase temperature is $T_\infty(>T_m)$ and the temperature of the solid far from the interface is $T_0(<T_m)$. The concentration at the wall is C_m and the surrounding porous medium is maintained at constant concentration C_∞ . With the usual boundary layer and linear Boussinesq approximations, the governing equations, namely the equation of continuity, the Darcy flow model, the energy and concentration equations for the isotropic and homogeneous porous medium may be written as

$$\frac{\partial u}{\partial x} + \frac{\partial v}{\partial y} = 0 \quad (1)$$

$$\frac{\partial u}{\partial y} + \frac{\partial}{\partial y} \left(\frac{K\sigma B_0}{\mu(T)} u^2 \right) = -\frac{\partial}{\partial x} \left(\frac{Kg}{\mu(T)} \rho_\infty [\beta_T(T - T_\infty) + \beta_C(C - C_\infty)] \right) \quad (2)$$

$$u \frac{\partial T}{\partial x} + v \frac{\partial T}{\partial y} = \alpha \frac{\partial^2 T}{\partial y^2} - \frac{1}{\rho_\infty c_p} \frac{\partial q_y^r}{\partial y} \quad (3)$$

$$u \frac{\partial C}{\partial x} + v \frac{\partial C}{\partial y} = D \frac{\partial^2 C}{\partial y^2} + D_1 \frac{\partial^2 T}{\partial y^2} \quad (4)$$

The associated boundary conditions are:

$$y = 0: v = 0, T = T_m, C = C_m \quad (5)$$

$$y \rightarrow \infty: u \rightarrow 0, T \rightarrow T_\infty, C \rightarrow C_\infty \quad (6)$$

In the above equations, u and v are the average velocity components along the x and y directions. ρ_∞ is the density at some reference point, g is the acceleration due to gravity, β_T and β_C are the coefficients of thermal and concentration expansion, respectively. Also, b is the empirical constant associated with the Forchheimer porous inertia term and $\mu(T)$ is the variable consistency index, while c_p is the specific heat at constant pressure. α and D are the effective thermal and solutal diffusivities, respectively, D_1 quantifies the contribution to the mass flux due to temperature gradient, The radiative heat flux term q_y^r is written using the Rosseland approximation (Sparrow and Cess [13]) as

$$q_y^r = -\frac{4\sigma}{3k^*} \frac{\partial T^4}{\partial y} \quad (7)$$

where σ and k^* are the Stefan-Boltzman constant and the mean absorption coefficient, respectively. T^4 is expressed as a linear function of temperature, hence

$$T^4 \approx 4T_\infty^3 T - 3T_\infty^4 \quad (8)$$

The continuity equation is automatically satisfied by defining a stream function $\psi(x, y)$

such that $u = \frac{\partial \psi}{\partial y}$ and $v = -\frac{\partial \psi}{\partial x}$. We introduce the following similarity transformation:

$$\eta = \frac{y}{x} Ra_x^{1/3}, \psi(\eta) = \alpha Ra_x^{1/3} f(\eta), \theta(\eta) = \frac{T - T_m}{T_\infty - T_m}, \varphi(\eta) = \frac{C - C_m}{C_\infty - C_m},$$

$$\text{where } Ra_x = \frac{x}{\alpha} \left[\frac{\rho_\infty K g \beta_T (T_\infty - T_m)}{\mu_\infty} \right].$$

The fluid viscosity $\mu(\theta)$ is assumed to obey Reynolds viscosity model

$$\mu(\theta) = \mu_\infty e^{-\xi \theta} \quad (9)$$

where ξ is the non-dimensional viscosity parameter depending on the nature of the fluid and μ_∞ is the ambient viscosity of the fluid.

The above transformation reduces the system of partial differential equations into the following system of nonlinear ordinary differential equations:

$$(1 + M_g e^{\xi \theta}) f'' + M_g \xi e^{\xi \theta} f' \theta' = -\frac{2\eta}{3} e^{\xi \theta} [(\theta' + N \varphi') + \xi(\theta + N \varphi)] \quad (10)$$

$$\theta'' + \frac{1}{3} f \theta' + \frac{4}{3} R [(C_t + \theta)^3 \theta']' = 0 \quad (11)$$

$$\frac{1}{Le} \varphi'' + \frac{1}{3} f \varphi' + S_r \theta'' = 0 \quad (12)$$

The transformed boundary conditions are

$$\eta = 0: f + 3m\theta' = 0, \theta = 0, \varphi = 0 \quad (13)$$

$$\eta \rightarrow \infty: f' \rightarrow 0, \theta \rightarrow 1, \varphi \rightarrow 1 \quad (14)$$

In the above, $R = \frac{4\sigma T_\infty^3}{k^*k}$, $S_r = \frac{D_1(T_\infty - T_m)}{\alpha(C_m - C_\infty)}$, $N = \beta_c(C_m - C_\infty)/\beta_T(T_m - T_\infty)$, $Le = \alpha/D$ and $Gr^* = b \left(\frac{k^* \rho^2 [g\beta(T_m - T_\infty)]}{\mu_\infty^2} \right)$ fluid of variable viscosity saturated are the radiation, thermo-diffusion or Soret parameter, buoyancy ratio, Lewis number and modified Grashof number, respectively. The parameter $N > 0$ represents the aiding buoyancy and $N < 0$ represents the opposing buoyancy.

In the presence of radiation, the surface heat and mass fluxes from the wall to the medium is given by

$$q_T = -k \left(\frac{\partial T}{\partial y} \right) - \frac{4\sigma}{3k^*} \left(\frac{\partial T^4}{\partial y} \right)_{y=0}, \quad (15)$$

$$q_c = -D \left(\frac{\partial C}{\partial y} \right) \quad (16)$$

using these, non-dimensional heat and mass transfers coefficient are written as

$$\frac{Nu_x}{Ra_x^{1/3}} = -\theta'(0) \left(1 + \frac{4}{3} R \right), \quad (17)$$

$$\frac{Sh_x}{Ra_x^{1/3}} = -\phi'(0). \quad (18)$$

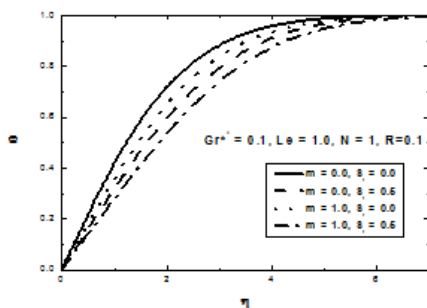


Fig.2: Variation of temperature profiles with similarity variable η

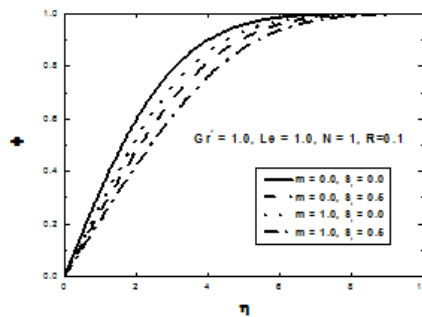


Fig. 3: Variation of concentration profiles with similarity variable η

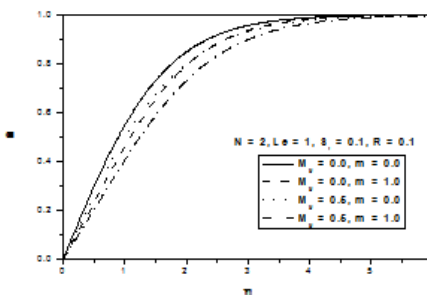


Fig. 4: Variation of temperature profiles with similarity variable η

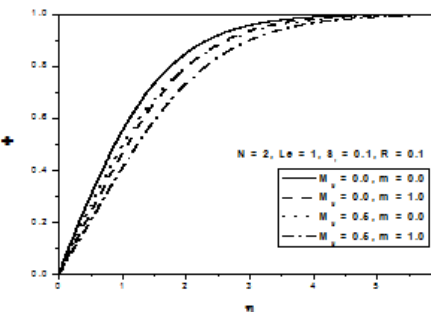


Fig. 5: Variation of concentration profiles with similarity variable η

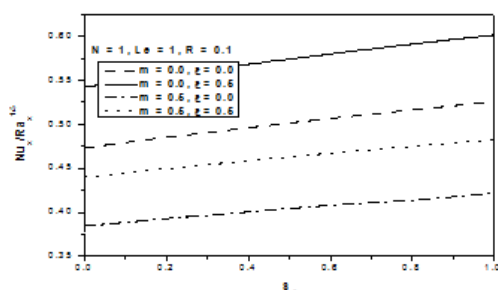


Fig. 6: Variation of heat transfer coefficient against S_r for varying m and ξ .

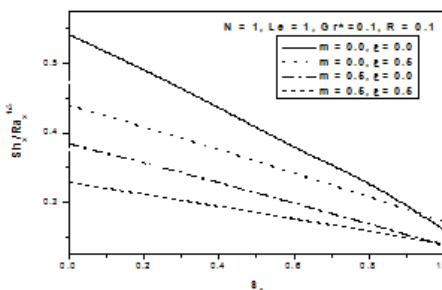


Fig.7: Variation of mass transfer coefficient

Results and Discussion

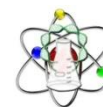
The non-linear ordinary differential equations (10)-(12) with the boundary conditions (13-14) are solved using 4th order Runge-Kutta method by shooting and matching technique. The variation of heat and mass

transfer coefficients are shown for some selected values of the parameters through figures. Figures 2 and 3 illustrate the variation of the non-dimensional temperature and concentration profiles θ and ϕ , respectively, against the similarity variable η across the boundary layer for two sets of values of S_r and m for fixed value of other parameters. It is seen that increasing the melting parameter m tends to increase both thermal and concentration boundary layer thicknesses. With an increase in the Soret parameter, a rise in temperature profiles and fall in the concentration profiles is seen against the similarity variable η inside the boundary layer. Figures 4 and 5 display the temperature and concentration profiles θ and ϕ , respectively, for various values of melting parameter m and magnetic parameter M_g for fixed value of other parameters. It is clearly shown that both temperature and concentration boundary layer thicknesses increase with an increase in the values of magnetic and melting parameter.

The variation of non-dimensional heat transfer coefficient (Nusselt number) and non-dimensional mass transfer coefficient (Sherwood number) against the Soret parameter S_r for different values of m and ξ is plotted in Figures 6 and 7, respectively. It is observed that Nusselt number increases with Soret parameter and viscosity parameter while the same decreases with increase in the values of melting parameter. It is observed that as the melting parameter increases the impact of viscosity parameter on the heat transfer rate reduced. On the other hand Sherwood number decreases with increased values of viscosity, melting and Soret parameters. As in the case of heat transfer rate the mass transfer rate is reduced with the increase in the values of melting parameter.

References

1. Bejan, A. (2004). Convective Heat Transfer. New York. Wiley. First Edition.
2. Chamkha, A. J. (1997). Non-Darcy fully developed mixed convection in a porous medium channel with heat generation/absorption and hydromagnetic effects. Numerical Heat Transfer 32, pp. 853–875.
3. Cheng, W. T. and Lin, C. H. (2007). Melting effect on mixed convective heat transfer with aiding and opposing external flows from the vertical plate in a liquid-saturated porous medium. International Journal of Heat and Mass Transfer 50, pp. 3026-3034.
4. Epstein, M. and Cho, D. H. (1976). Melting heat transfer in steady laminar flow over a flat plate. ASME Journal of Heat Transfer 98, pp. 531–533.
5. Gorla, R. S. R., Mansour, M. A., Hassanien, I. A. and Bakier, A. Y. (1999). Mixed convection effect on melting from a vertical plate in a porous medium. Transport in Porous Media 36, pp. 245-254.
6. Hassanien, I. A. and Bakier, A. Y. (1991). Melting with mixed convection flow from horizontal plate embedded in a porous medium. Earth, Moon and Planets 52, pp. 51-63.
7. Kazmierczak, M., Poulikakos, D. and Pop, I. (1986). Melting from a flat plate embedded in a porous medium in the presence of steady convection. Numerical Heat Transfer 10, pp. 571–581.
8. Kazmierczak, M., Poulikakos, D. and Sadowski, D. (1987). Melting of a vertical plate in porous medium controlled by forced convection of a dissimilar fluid. International Communication in Heat Mass Transfer 14, pp. 507-517.
9. Luikov, A. V. and Mikhailov, Y. A. (1936). Theory of Energy and Mass Transfer. Pergamon press. Oxford.
10. Narayana, P. A. L. and Murthy, P. V. S. N. (2008). Soret and Dufour effect on free convection heat and mass transfer from a horizontal plate in a Darcy Porous medium. ASME Journal of Heat Transfer 130(10).
11. Postelnicu, A. (2007). The influence of chemical reaction on heat and mass transfer by natural convection from vertical surfaces in porous media considering SoretDufour effects. Heat Mass Transfer 43, pp. 595-602.
12. Tashtoush, B. (2005). Magnetic and buoyancy effects on melting from a vertical plate embedded in a saturated porous media. Energy Conversion and Management 46, pp. 2566-2577.
13. Sparrow, E. M. and Cess, R. D.: Radiation Heat Transfer, Hemisphere, Washington.
14. Kairi, R. R. (2011), Melting and Soret effect in presence of magnetic field on natural convection from a horizontal plate, International Journal of Applied Mathematics and Mechanics 7 (14), pp. 42-56.



AUTO-TANDEM CATALYSIS: AN UNIQUE APPROACH FOR THE DIRECT CONVERSION OF ISOXAZOLE TO 2-AZAFLUORENONE

Sajal Das

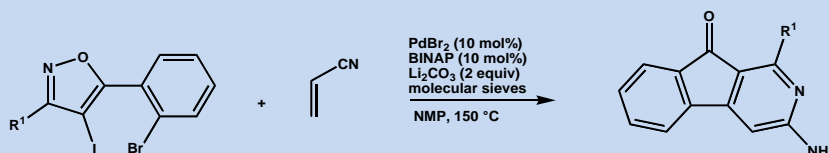
Department of Chemistry, University of North Bengal, Darjeeling 734 013

E-mail: sajal.das@hotmail.com

ABSTRACT

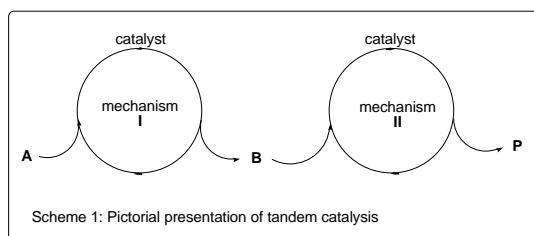
One-pot procedures involving multiple catalytic events constitute a subset of the broader category of one-pot processes that includes domino, cascade, or tandem *reactions*. Few inherent features those make it more interesting are atom economy, time and cost savings, environmental friendliness, and potential applications in the rapid construction of complex molecular structures. Among all other categories, auto-tandem catalysis is the most intriguing as two or more mechanistically distinct catalysis promoted by a single catalyst precursor: both cycles occur spontaneously by cooperative interaction of the various species (catalyst, substrate, additional reagents if required) present at the outset of reaction. No reagents beyond those originally present need be added to trigger the change in mechanism. Entry into both cycles is presumed to be mediated by a catalyst species in which the structure is *essentially* conserved, though intermediates will necessarily differ at points in each cycle. Thus, it is really difficult to control the reaction when the optimal condition for multiple catalytic cycles are differ from each other and the development of tandem reaction is still challenging task.

As a part of our continuous efforts we have successfully developed an auto-tandem Palladium catalytic process for the direct conversion of isoxazole to 2-azafluorenone in one pot as appended below.



Introduction

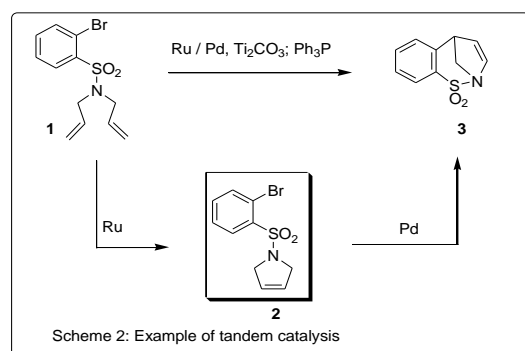
Replacement of multiple steps chemical synthetic process with efficient catalyzed technique which strive for atom economy is having an important impact in the synthesis of fine chemicals and pharmaceutical interesting compounds.¹ “Tandem” reactions, in which various synthetic reactions are combined into one synthetic operation, have been reported extensively in the synthetic chemistry literature.² More specific terms to describe it are domino, cascade, multicomponent or one pot reaction. Individual reactions are so closely



coupled that often yield a product which difficult to obtain by single process. This attributed that the intermediates are not stable enough for isolation and quickly transformed into a stable species. The term “tandem catalysis” has been used to describe the synthetic strategies that comprise the *sequential* use of catalytic reactions with minimum workup, or change in conditions.³ Scheme 1 describe a general example of

tandem catalysis. After the first catalytic cycle substrate A is converting into an intermediate B which immediately get into the next catalytic cycle to resulted in the final product P. Inherent features those make it more interesting are atom economy, time and cost savings, environmental friendliness, and potential applications in the rapid construction of complex molecular structures.

Tandem catalysis can be categorized⁴ as follows a) Orthogonal tandem catalysis [this involves two or more functionally distinct and noninterfering catalysts or precatalysts, all of which are present from the outset of reaction]; b) Auto tandem catalysis [in this process, two or more mechanistically distinct catalyses promoted by a single catalyst precursor] and c) assisted tandem catalysis [catalyst require reagent to trigger a change in

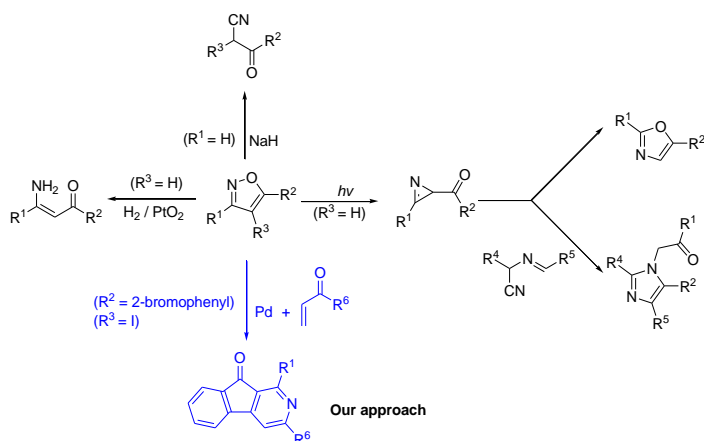


mechanism]. An example of tandem catalysis⁴ is shown in scheme 2. Here, compound **1** undergoes two consecutive reaction in the presence of two different catalyst and results in the final product **2**. If we analyze the reaction deeply, then it is possible to predict the actual pathway of this reaction. Principally, this reaction proceeds *via* an intermediate **2** which results after olefin metathesis reaction. After that the intermediate participate in Pd catalyzed C-C cross coupling reaction (Heck Reaction) to yield the final compound **3**.

Among all other categories, auto-tandem catalysis is the most intriguing as two or more mechanistically distinct catalysis promoted by a single catalyst precursor: both

cycles occur spontaneously by cooperative interaction of the various species (catalyst, substrate, additional reagents if required) present at the outset of reaction.⁵ No reagents beyond those originally present need be added to trigger the change in mechanism. Entry into both cycles is presumed to be mediated by a catalyst species in which the structure is *essentially* conserved, though intermediates will necessarily differ at points in each cycle. Thus, it is really difficult to control the reaction when the optimal condition for multiple catalytic cycles are differ from each other and the development of tandem reaction is still challenging task.

Nitrogen containing heterocycles are the most privileged scaffolds found in both natural products and biologically active molecules and this has encourage the researchers to develop

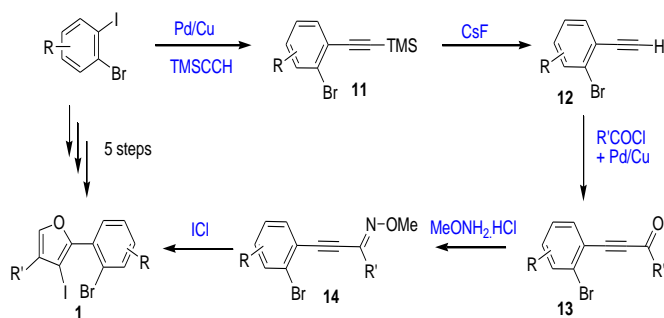


Scheme 3: Reactions of isoxazole

new and efficient synthetic protocol for such moieties. Beside the other applications Isoxazoles, five membered heterocycles, also serve as important building blocks in organic synthesis. Reactions of isoxazoles are summarized in scheme 3. Hydrogenation over platinum oxide, isoxazole undergoes ring opening reaction and resulted in □ □ □ □ unsaturated ketone⁶In contrary, □-keto nitriles in high yield were obtained *via* a ring-opening process when isoxazole was treated with NaH.⁷ When isoxazole exposed to light⁸ (a particular wave length), the N-O bond undergoes homolytic cleavage and

results in acyl acylazirine to generate the three-membered ring and eventually it formed oxazole. This is known as photoisomerization reaction. The efficiency of reaction can be enhanced by using triplet sensitizer. The intermediate, acylazirine may participate in condensation reaction with α -aminonitrile in the presence of pyridine upon heating and yielded imidazole as final product. Palladium-catalyzed ring-opening reactions of isoxazoles remain unknown. Our ongoing interest in developing late-transition-metal-catalyzed processes for the preparation of biologically interesting heterocycles has prompted us to explore more facile synthetic approaches for heterocycles with higher molecular complexity. In our lab, we have utilized halogen substituted isoxazole as building blocks for the construction of even more complex structure, 2-azafluorenones. The tandem palladium-catalyzed Heck/Heck-rearrangement reaction from halogen-substituted isoxazoles and Michael acceptors are the key factors/steps for construction of 2-azafluorenones in one pot.⁹

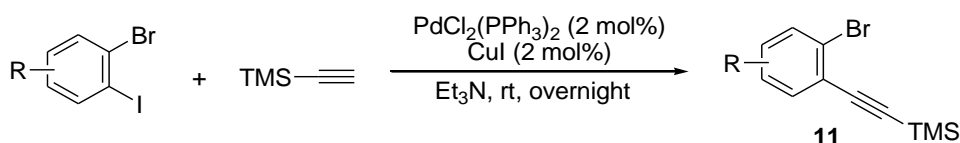
Before the description of 2-azafluorenones synthesis, we rather highlight the opted technique for the construction of halogen substituted isoxazole (scheme 4). We have started from very simple compound substituted 2-bromo iodobenzene.



Scheme 4: Synthesis of isoxazoles

Preparation of ((2-bromophenyl)ethynyl)trimethylsilane (11).

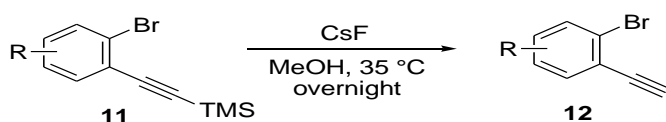
A 6-dram vial was charged with 2-bromoaryliodide (2.0 mmol), ethynyltrimethylsilane (117.86 mg, 2.4 mmol), Pd(PPh₃)₂Cl₂ (21.06 mg, 0.04 mmol), CuI (5.7 mg, 0.04mmol), and Et₃N (12 mL). The vial was then purged with argon and sealed. The reaction mixture was stirred at room temperature overnight, until the



disappearance of starting material was observed, as monitored by thin layer chromatography. The reaction mixture was diluted with diethyl ether (20 mL) and washed with brine (20 mL), and the aqueous phase was then extracted with diethyl ether (2×20 mL). The combined organic layers were dried over anhydrous MgSO_4 , concentrated under reduced pressure; the resulting residue was purified by flash column chromatography on silica gel.

Preparation of 1-bromo-2-ethynylbenzene (12).

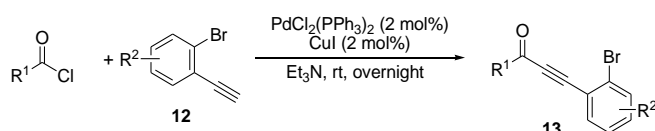
A 6-dram vial was charged with ((2-bromophenyl) ethynyl) trimethylsilane (**11**, 2.0 mmol), CsF (455.7 mg, 3.0 mmol) & methanol (15 mL). The reaction mixture was stirred at 35°C overnight until the disappearance of the starting material as monitored by thin layer chromatography. Methanol was removed using a rotary evaporator under reduced pressure (20 mmHg). The residue was dissolved in diethyl ether (40 mL) & washed with brine (30 mL). The aqueous phase was extracted with diethyl ether (2 × 20 mL).



The combined organic layers were dried over anhydrous MgSO_4 , and concentrated using a rotary evaporator under reduced pressure. The residue was purified by flash column chromatography on silica gel.

General procedure for the preparation of 3-aryl-alkynone (13).

A 4-dram vial was charged with PdCl₂(PPh₃)₂ (21.06 mg, 0.02 mmol), CuI (5.7 mg, 0.02 mmol), acid chloride (1.3 mmol), 1-bromo-2-ethynylbenzene (**12**, 1 mmol), and triethylamine (8 mL). The reaction mixture was stirred at room temperature overnight. After completion of reaction as monitored by thin layer chromatography, the resulting mixture was diluted with 15 mL of diethyl ether and washed with brine (15 mL).



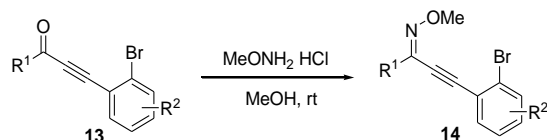
The aqueous phase was extracted with diethyl ether (2×15 mL). The combined organic layers were dried over anhydrous MgSO_4 , and concentrated under reduced pressure (20 mmHg). The residue was purified by flash

column chromatography on silica gel.

Preparation of alkynone *O*-methyl oxime (14).

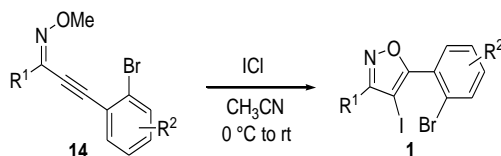
A 6-dram vial was charged with *O*-methylhydroxylamine hydrochloride (167 mg, 2.0 mmol), Na₂SO₄ (284 mg,

2.0 mmol), pyridine (0.5 mL), benzene (1 mL), 3-arylalkynone (**13**, 1 mmol), and methanol (5 mL). The reaction mixture was stirred at room temperature overnight. After completion of reaction as monitored by thin layer chromatography, the resulting mixture was concentrated under reduced pressure (20 mmHg) to remove methanol. The reaction mixture was then diluted with 15 mL of diethyl ether and washed with brine (15 mL). The aqueous phase was extracted with diethyl ether (2×15 mL). The combined organic layers were dried over anhydrous MgSO_4 , and concentrated under reduced pressure. The residue was purified by flash column chromatography on silica gel.



General procedure for the preparation of 5-(2-bromophenyl)-4-iodoisoxazoles (**1**)

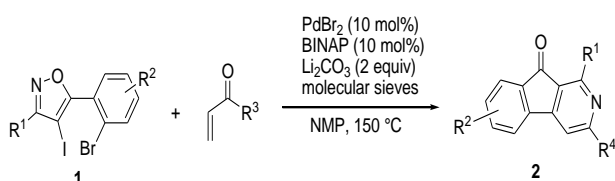
A 4-dram vial was charged with alkynone *O*-methyl oxime (**14**, 1 mmol), acetonitrile (4 mL) and immersed in an ice bath with constant stirring. After 10 minutes, ICl (487 mg, 3 mmol) in 1 mL of acetonitrile was added dropwise. After completion of reaction (30 minutes) as monitored by thin layer chromatography, the resulting mixture was diluted with 15 mL of diethyl ether and washed with sodium thiosulphate aqueous solution (0.1 M) to remove the excess amount of ICl. The aqueous phase was extracted with diethyl ether (3×15 mL). The combined organic layers were dried over anhydrous MgSO_4 , and concentrated under reduced pressure. The residue was purified by flash column chromatography on silica gel.



Preparation of 2-Azafluorenone from substituted isoxazole (Scheme 5)

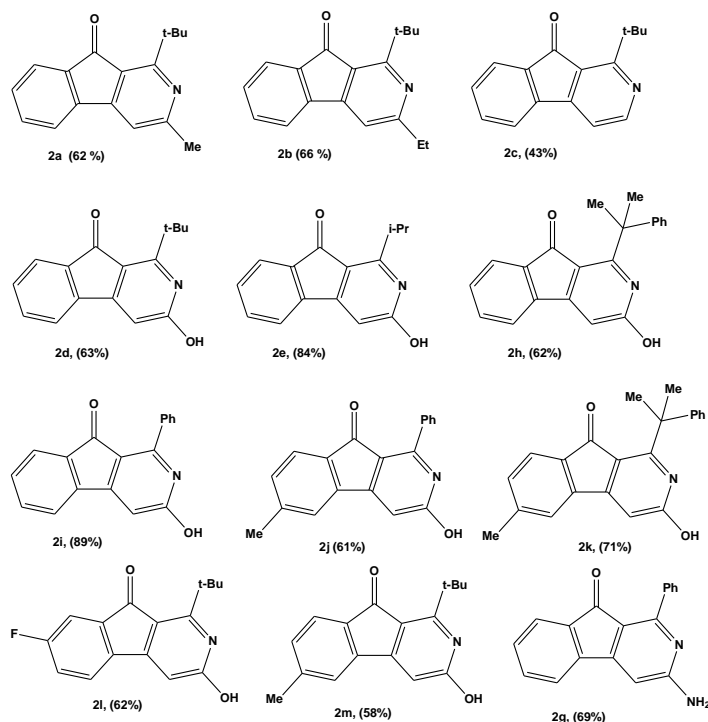
2-Azafluorenone is known as activating agents of phosphatidylinositol specific phospholipase C in C6 glioma cells. Their unique chemical and biological characteristics have attracted the attention of synthetic organic chemists for decades. The known synthetic methods for 2-azafluorenone include (a) a three-component reaction protocol with Knoevenagel condensation as the key step, (b) intramolecular acylation of 4-phenylpyridinyl substrates, (c) a palladium-catalyzed intramolecular coupling reaction of (2-halophenyl)-pyridinylmethanone, (d) Pschorr cyclization of 2-nicotinoylbenzenediazonium salt, and (e) an intramolecular Diels–Alder reaction of (2-alkynylphenyl)(1,2,4-triazin-6-yl)methanone. New efficient synthetic protocols for 2-azafluorenone are still in high demand.

After long trial of different parameters we found the combination of PdBr_2 as catalyst, BINAP (ligand), Lithium carbonate (base) molecular sieves as additive in NMP as solvent at 150°C is best suited for this studied reaction. The procedure for this present reaction for the synthesis of 2-Azafluorenone is as follows. A 4-dram

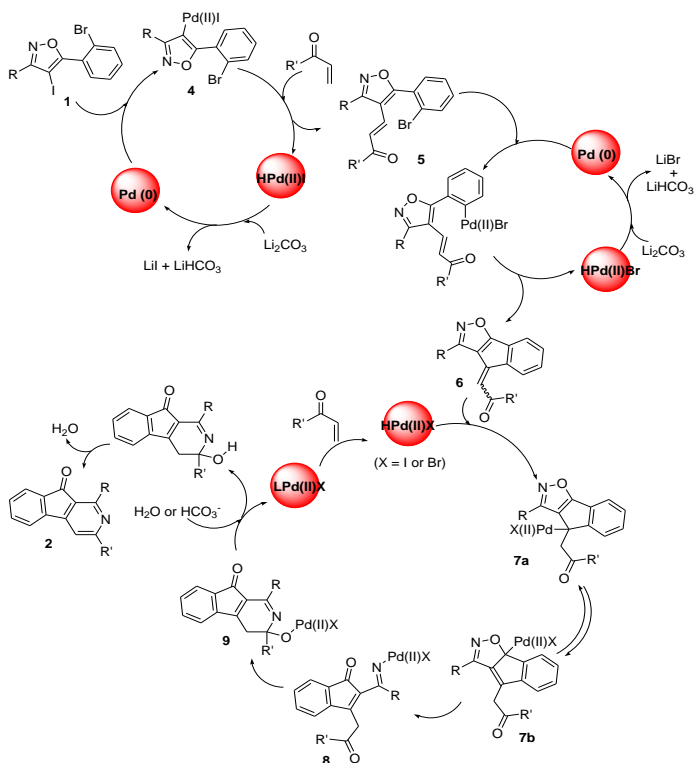


vial was charged with PdBr_2 (13.31 mg, 0.05 mmol), BINAP (31.13 mg, 0.05 mmol), Li_2CO_3 (73.88 mg, 1.0 mmol), molecular sieves (80 wt.%), iodoxazole (**1**, 0.5 mmol), Michael acceptor (1.5 mmol) and NMP (5 mL). The reaction mixture was purged with argon and placed in preheated oil bath at 150°C and

stirred for 6 h. After cooling to room temperature, the resulting mixture was diluted with 15 mL of diethyl ether and washed with brine (15 mL). The aqueous phase was extracted with diethyl ether (2×10 mL) and ethylacetate (2×10 mL). The combined organic layers were further washed with water (10 mL) and dried over anhydrous MgSO_4 , and concentrated using a rotary evaporator under reduced pressure (20 mmHg). The residue was purified by flash column chromatography on silica gel. Under this optimized condition we have synthesized a variety of 2-azafluorenone given below in the table 1.

Table 1: Scope of 2-Azafluorenone synthesis

organopalladium intermediate **7** containing a π -allylpalladium moiety. β -Imino elimination of **7b** opens the isoxazole ring, leading to the formation of indenone intermediate **8**. The latter undergoes an intramolecular cyclization to generate tricyclic intermediate **9**. Protonation of **9** and subsequent dehydration furnish the final product **2**. It is worth noting that the leaving group in the last step is either alcohol or an amine when an acrylate or acrylamide, respectively, is employed, leading to the exclusive formation of 3-hydroxy-2-azafluorenone. An imine-enamine tautomerization furnishes the final product when acrylonitrile is used. APd(II) complex is regenerated at the end of the rearrangement cycle, which can be converted to the XPd(II)H complex by reaction with a Michael acceptor. Two mechanistically distinct catalytic cycles coexist in this tandem catalysis: a Heck reaction and a rearrangement reaction. While the XPd(II)H complex generated in the Heck reaction needs to be reduced to Pd(0) by a base before entering the next Heck catalytic cycle, it is also essential to maintain a sufficient concentration of XPd(II)H complex in the reaction medium to initiate the rearrangement cycle taking place concurrently in the tandem catalysis. Therefore, it is critical to choose an appropriate base to maintain sufficient concentrations of both XPd(II)H and Pd(0) species in the reaction medium.



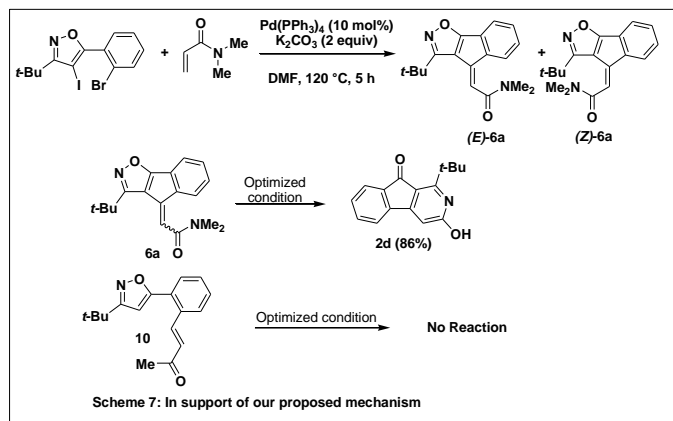
Scheme 6: Plausible mechanism

The reaction scope was investigated using the optimized conditions. Besides alkyl vinyl ketones, other Michael acceptors such as acrolein, acrylates, acrylamides, and acrylonitrile all work well in this reaction. Although moderate yields were obtained with alkyl vinyl ketones, acrolein, acrylates, and acrylonitrile, excellent chemical yields were obtained when acrylamides were employed in this reaction. It is worth noting that the reaction between isoxazole **1a** and acrylates or acrylamides all exclusively lead to the same product, 3-hydroxy-2-azafluorenone **2d**.

A proposed mechanism for the observed tandem catalysis is shown in Scheme 6, starting with an intermolecular Heck reaction between isoxazole **1** and a Michael acceptor to form 4-alkenylisoxazole **5**. A subsequent intramolecular Heck reaction forms indenoisoxazole intermediate **6**. Palladium hydride reinsertion into **6** leads to organopalladium intermediate **7** containing a π -allylpalladium moiety. β -Imino elimination of **7b** opens the isoxazole ring, leading to the formation of indenone intermediate **8**. The latter undergoes an intramolecular cyclization to generate tricyclic intermediate **9**. Protonation of **9** and subsequent dehydration furnish the final product **2**. It is worth noting that the leaving group in the last step is either alcohol or an amine when an acrylate or acrylamide, respectively, is employed, leading to the exclusive formation of 3-hydroxy-2-azafluorenone. An imine-enamine tautomerization furnishes the final product when acrylonitrile is used. APd(II) complex is regenerated at the end of the rearrangement cycle, which can be converted to the XPd(II)H complex by reaction with a Michael acceptor. Two mechanistically distinct catalytic cycles coexist in this tandem catalysis: a Heck reaction and a rearrangement reaction. While the XPd(II)H complex generated in the Heck reaction needs to be reduced to Pd(0) by a base before entering the next Heck catalytic cycle, it is also essential to maintain a sufficient concentration of XPd(II)H complex in the reaction medium to initiate the rearrangement cycle taking place concurrently in the tandem catalysis. Therefore, it is critical to choose an appropriate base to maintain sufficient concentrations of both XPd(II)H and Pd(0) species in the reaction medium.

Further, our proposed mechanism for this current tandem catalysis is supported by the following experiment given in scheme 7. The presumed intermediate compound, indenoisoxazolyldiene-*N,N*-dimethylacetamide **6a**, was prepared from **1a** by

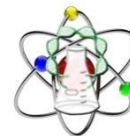
heating with *N,N*-dimethylacrylamide in the presence of $\text{Pd}(\text{PPh}_3)_4$ and K_2CO_3 at 120 °C. Under this condition, two consecutive Heck cross coupling occurred and it results a mixture of (E)- and (Z)-**6a** isomer in 55% yield. When this mixture was subjected to our optimized reaction conditions, the reaction was complete in 4 h, and product **2d** was isolated in 86% yield. In contrary, when a mono Heck coupled product (**10**), was treated under optimized condition, we did not observed any kind of such product. This experiment proved that the present reaction goes *via* indenoisoxazolydene-*N,N*-dimethylacetamide **6a**, intermediate.



In summary, a new synthetic approach towards 2-azafluorenones by a tandem palladium catalyzed Heck-Heck-rearrangement reaction from halogen-substituted isoxazoles and Michael acceptors has been discussed. This catalysis involves two palladium-catalyzed mechanistically distinct reactions: a Heck reaction and a palladium-catalyzed rearrangement of 4-methylene-indenoisoxazoles.

References

- (a) Sheldon, R. A. *J. Mol. Catal., A: Chem.* 1996, 107, 75. (b) Sheldon, R. A. *Pure Appl. Chem.* 2000, 72, 1233.
- (a) Posner, G. H. *Chem. Rev.* 1986, 86, 831. (b) Ho, T.-L. *Tandem Organic Reactions*; Wiley-Interscience: New York, 1992. (c) Hall, N. *Science* 1994, 266, 32. (d) Tietze, L. F. *Chem. Rev.* 1996, 96, 115.
- (a) Burk, M. J.; Lee, J. R.; Martinez, J. P. *J. Am. Chem. Soc.* 1994, 116, 10847. (b) Balema, V. P.; Hey-Hawkins, E. Z. *Anorg. Allg. Chem.* 1996, 622, 2053.
- Wasilke, J. C.; Obrey, S. J.; Baker, R. T.; Bazan, G. C. *Chem. Rev.* 2005, 105, 1001.
- (a) Louie, J.; Bielawski, C. W.; Grubbs, R. H. *J. Am. Chem. Soc.* **2001**, 123, 11312. (b) Kanbayashi, N.; Takenaka, K.; Okamura, T.; Onitsuka, K. *Angew. Chem. Int. Ed.* **2013**, 52, 4897. (c) Yang, Y.; Shu, W.-M.; Yu, S.-B.; Ni, F.; Gao, M.; Wu, A.-X. *Chem. Commun.* **2013**, 49, 1729. (d) Takasu, K.; Tanaka, T.; Azuma, T.; Takemoto, Y. *Chem. Commun.* **2010**, 46, 8246. (e) Li, L.; Herzog, S. B. *Nature Chem.* **2014**, 6, 22.
- Fogagnolo, M.; Giovannini, P. P.; Guerrini, A.; Medici, A.; Pedrini, P.; Colombi, N. *Tetrahedron: Asymmetry* **1998**, 9, 2317.
- Dominguez, E.; Ibeas, E.; Martinez de Marigorta, E.; Palacios, J. K.; SanMartin, R. *J. Org. Chem.* **1996**, 61, 5435-5439.
- Nunes, C. M.; Reva, I.; Fausto, R. *J. Org. Chem.* **2013**, 78, 10657-10665.
- Das, S.; Hong, D.; Chen, Z.; She, Z.; Hersch, W. H.; Subramaniam, G.; Chen, Y. *Org. Lett.* **2016**, 17, 5578.



FERROELECTRIC AND ANTIFERROELECTRIC LIQUID CRYSTALS – STRUCTURES AND APPLICATIONS

Kartick Ch. Dey

*Department of Physics, Acharya Prafulla Chandra Roy Govt. College,
P.O: Matigara, Dist. Darjeeling, Siliguri-734010, W.B., India
Email: kartickdeyl36@gmail.com*

ABSTRACT

Liquid crystal is thermodynamically stable state of matter. It possesses directional property of solid crystal and flow property of liquid. Ferroelectric liquid crystal (FLC) is an important variety where molecules are arranged in layers and tilted and possess chirality. Molecular chirality breaks the mirror symmetry and leads to rotation of azimuthal angle of the director and forms a helix along layer normal. Such molecules are switchable (bi-stable) between two states under an ac electric field. This switching property of FLCs has been utilized in display devices. The FLC based displays have several advantages—faster response, increased viewing angle, higher resolution etc. In antiferroelectric liquid crystals (AFLCs) the molecules of adjacent layers are tilted in opposite direction and hence the polarizations of layers are out of phase by 180° . Under an electric field parallel to smectic layers the molecules of AFLCs placed between crossed polarizer, switch from antiferroelectric (dark state), to one of the two symmetric ferroelectric states (bright state), showing double hysteresis loop. This phenomenon is known as tri-stable switching. High tilt AFLCs are very useful for eliminating the problem of dynamical light leakage at zero field and enhances the contrast ratio. For their tristate switching behaviour, micro-second response, hemispherical viewing angle and no –ghost effect AFLCs are promising material for fast display devices.

Introduction

In 1888 Friedrich Reinitzer, an Austrian botanist, was performing investigations about cholesterol at Charles University in Prague, [1, 2]. He synthesized the benzoate and found that cholesteryl benzoate does not melt in the same manner as other compounds, but has two melting points. At 145.5°C it melts into a cloudy liquid, and at 178.5°C it melts again and the cloudy liquid becomes clear. Reinitzer, send his sample to German physicist Otto Lehmann who was an expert in optics, for better examination. Lehmann examined the intermediate cloudy fluid, and reported it as crystalline state and he named the new state “Liquid Crystal”. Reinitzer presented his results, with credits to Lehmann at a meeting of the Vienna Chemical Society on May 3, 1888 [3]. Reinitzer had discovered the novel state of matter by chance

At first, the notion “liquid crystal” (LC) seems to be absurd. It, however, suggests that it is an intermediate state of a matter, in between the liquid and the crystal. It must possess some typical properties of a liquid (e. g. fluidity, inability to support shear, formation and coalescence of droplets) as well as some crystalline properties (anisotropy in optical, electrical, and magnetic properties, periodic arrangement of molecules in one spatial direction, etc.). The important characteristics of LCs are that it is affected by electric and magnetic fields and can rotate plane of polarization of light. For their properties, they find applications in display industries. The Liquid crystal display (LCD) screen is more energy efficient and can be disposed of more safely than a CRT. Its low electrical power consumption enables it to be used in battery-powered electronic equipment. LCDs are used in a wide range of applications including computer monitors, televisions, instrument panels, aircraft cockpit displays, clocks, watches, calculators etc.

Different types of Liquid Crystals

Liquid crystal is divided into two categories – Thermotropic and Lyotropic. The term “thermotropic” arises because transitions involving these mesophases are effected by changing temperature. Thermotropic liquid crystals are of interest both from the standpoint of basic research and also for applications. Thermotropic LCs

are divided into two categories. Calamatic and Discotic. Calamatic LCs are composed of rod like molecules. The Calamitic liquid crystals are divided into three categories: Nematic, Cholesteric, Smectic.

Nematic Liquid Crystal

The nematic phase is a one dimensional ordered elastic fluid. The molecules have only orientational order but no positional order. There is long range orientational order, i.e., molecules tend to align parallel to each other. The molecular order of nematic phase is shown schematically in Fig 1. The nematic phase is very sensitive to external electric and magnetic field and mechanical stresses, and it modifies the optical path of visible rays, for which they find wide application in display device [4].

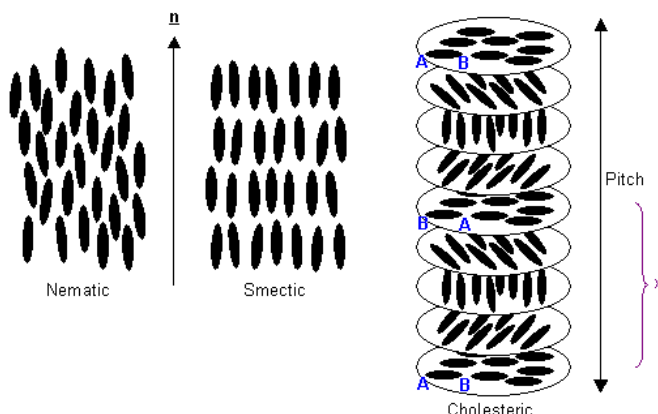


Fig 1. Nematic, Smectic and Cholesteric mesophases.

Cholesterol Liquid Crystal

When a nematic liquid crystal mixed with chiral molecules, the structure undergoes a helical distortion about an axis normal to the preferred molecular direction n . Thus the structure of a cholesteric liquid crystal is periodic and the director varies its direction. The period of this is known as the pitch p (Fig.1).

Smectic Liquid Crystal

Upon cooling from the nematic phase, LC molecules will often self-assemble into layers (Fig.1). These layered phases are called smectic LCs. When the director is perpendicular to the smectic layers and thus parallel to the layer normal (denoted z), the phase is referred to as a smectic A (or simply A). In the A phase, n is parallel to z . When cooling from the A phase, a more ordered smectic phase is often seen in which the molecules are tilted with respect to the layers. This tilted, layered phase is called the smectic C phase. No positional correlation being observed within the layer plane [5].

Ferroelectricity in Liquid Crystals

An idea of the ferroelectric mesophase was presented by R.B. Meyer at the 5th International Liquid Crystal Conference in 1974. From symmetry considerations he deduced that all tilted smectic phases composed of chiral molecules (without mirror symmetry) have to exhibit a (local) spontaneous polarization if the molecules contain a transverse permanent dipole moment. In SmC* phase molecules are arranged in fluid layers. On an average, molecules are tilted from the layer normal by an angle. The angle made between the layer normal and the director is termed the tilt angle (θ). The tilt defines a plane—containing n (molecular direction) and z (normal to layer) — called the tilt plane. The phase is optically biaxial [6].

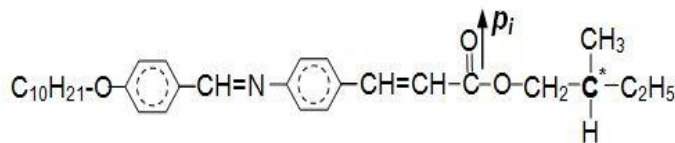


Fig 2. Structure of DOBAMBC

The maximum symmetry an achiral C phase can possess (i) C2 axis normal to the tilt plane, and (ii) σ plane congruent with the tilt plane. Meyer was the first person to realize the simple fact that a chiral phase can possess no reflection symmetry, and therefore the maximum possible symmetry for a chiral C phase is C2. Any medium with C2 symmetry must possess polar order, and therefore Meyer was able to make his famous prediction that chiral C phase (or SmC*) would be ferroelectric (making the reasonable assumption that the direction of the polarization in the polar LC phase would be switchable) [7].

The first synthesized compound fulfilling Meyer's specification is known by an acronym DOBAMBC, standing for (S)-(-)-p'-decyloxybenzylidene p'-amino 2-methylbutyl cinnamate [8]. The molecule of DOBAMBC contains an asymmetric carbon atom C rendering molecular chirality, while a lateral C=O group

provides a transverse permanent dipole moment p_i (Fig. 2). The aliphatic chain attached to the other end of the molecule by an oxygen atom is relatively long, favouring the SmC mesophase.

The other aspect of chirality is rotation of the director and thus also of the direction of dipole moment P about the smectic layer normal (Fig. 3a). Due to formation of the helical superstructure the spontaneous polarization is compensated to zero within one pitch of the helix, p , and the material appears to be non-polarized. In an alternating (a.c.) electric field a typical ferroelectric switching current, as well as electro-optical response is observed. This effect, being relatively fast ($\sim 10 \mu\text{s}$), represents the main principle of technical applications. With the synthesis and evaluation of DOBAMBC, the experimental study of the phenomenon of ferroelectricity in liquids began. Since then, an explosion of research and invention aimed at using and improving these novel materials has occurred.

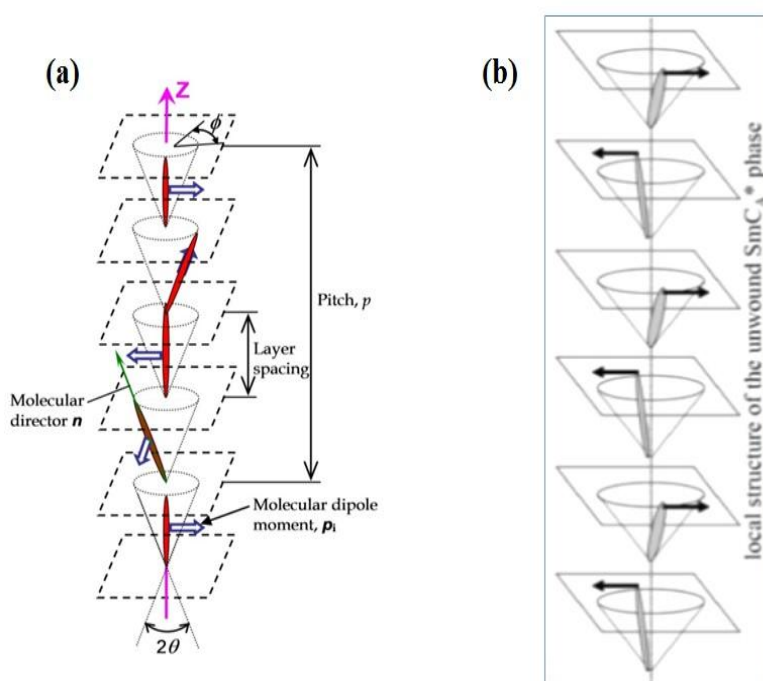


Fig 3: (a) The helicoidal structure of chiral smectic C (SmC*) crystal. The molecular dipole moment \mathbf{p}_i is always perpendicular to the director \mathbf{n} and tangent to the circle of intersection of the cone with the boundary plane of the layer. Azimuthal angle function of the coordinate parallel to the layer normal, tilt angle. (b) The dipole moments alternate in adjacent layers in SmC* phase. Adjacent layers form a helical structure.

Relaxation Modes of FLC liquid crystals

Collective and non-collective relaxations are observed in FLCs. Two collective relaxations (a) Soft mode (observed in A* phase and near C*–A* transition without bias) and (b) Goldstone mode (observed in C* phase without bias) are described here briefly.

Soft mode

Soft mode actually arises from the tilt angle fluctuation of the director. In SmA phase the stability of the structure is maintained by an elastic constant. However due to thermal energy there may be some local instantaneous fluctuation of the tilt angle. Now if the A phase is cooled down to A-C transition, the elastic constant controlling the tilt fluctuation gets soft. Thus the fluctuation amplitude increases drastically. Thus the permittivity diverges and the frequency of tilt fluctuation falls to zero when the temperature approaches the transition temperature. After transition, the molecules also fluctuate collectively around the equilibrium tilt angle. Thus soft mode is present both in smectic C and A phase [9].

Goldstone mode

The SmC* phase is characterized by its chirality, molecular tilt and helical structure. If the director of the molecules fluctuates locally as a result of thermal excitation in azimuthal direction, then this partial reorientation will propagate along the helical axis with a long wavelength. Hence in SmC* phase, there is an additional mode, originates from phase fluctuation of molecular director, called Goldstone mode [10].

Antiferroelectric Liquid Crystals

Another type of liquid crystal exists where the molecules possess chirality and the dipolar cancellation does not take place via a helix but directly from neighbor to neighbor. This means that alternating smectic layers constitutes two sub-lattices of opposite polarization and therefore has opposite tilt, in the kind of herring-bone pattern illustrated in Fig. 4. This corresponds to the dipolar antiferroelectric (AF) pattern. The phase consisting of chiral molecules in successive layers together with such pattern is termed as SmC_A^* phase. Liquid crystals possessing SmC_A^* phases (there may be SmC^* phase at higher temperature) along with other sub-phases (Viz. SmC_a^* , SmC_β^* , SmC_γ^*) are termed as Antiferroelectric liquid crystals (AFLCs) [11].

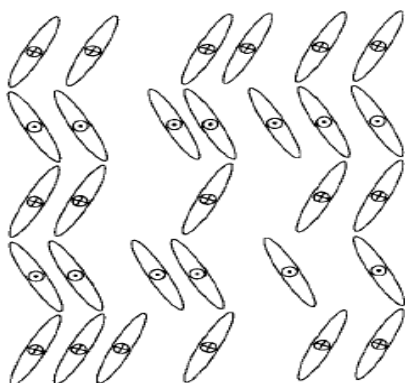


Fig 4. Herring-bone pattern in the hypothetical structure of antiferroelectric liquid crystal. Molecules, on average, have alternating tilt in alternating layers, corresponding to dipole moments pointing alternately into and out of the paper. The director \mathbf{n} would now refer to a single layer like the \mathbf{c} director, and the \mathbf{c} directors of adjacent layers would be anti-parallel. The structure would be biaxial with the layer normal bi-secting the angle between the optic axes.

The chirality induces a slight procession of tilt direction from layer to layer and thus develops spontaneous polarization within a layer. This leads to formation of helicoidal structure with axis parallel to layer normal (Fig. 3b). The direction of molecular tilt and hence direction of spontaneous polarization of adjacent layers are in opposite direction ($\sim 180^\circ$) in SmC_A^* phase. This type of molecular conformation is known as anticlinic conformation.

Relaxation Modes of SmC_A^* phase

Since the discovery of antiferroelectric phase [12], several authors are studying this phase with great importance [13–17]. The alternate layers of molecules in this phase form a helicoidally superstructure. Generally without bias two relaxation process (a) low frequency P_L and (b) high frequency P_H are observed in this phase. P_L mode arises from phase fluctuation of antiferroelectric dipole. Yu Panarin et al. [18] interpreted this mode as antiferroelectric Goldstone mode.

The second process which corresponds to the high frequency dielectric relaxation process is called non-cancellation mode. Panarin et al [19] reported the process is linked to the anti-phase reorientation of the molecules around the long axis. Some author interpreted this as soft mode.

Applications of ferroelectric and antiferroelectric liquid crystals

At present high definition displays (AMLCDs) with viewing angle of ~ 178 degrees are available in market. Twisted nematic liquid crystals are generally used in such displays. High value of response time ($\sim \text{ms}$) governing the frame rate, ghost effect and contrast ratio are still a matter for further improvement. As a result during the process of development of LCDs, two types of LCs namely ferroelectric liquid crystal (FLC) and antiferroelectric liquid crystal (AFLC) gathered a special interest during last decade of 20th century due to their low response time (μs). The basic reason for application of these two types of LCs is due to a special type of molecular packing in them. Manifold problem were faced to development displays based on FLCs. Some of them are small cell spacing ($1\text{--}2\ \mu\text{m}$) to unwind the helix, the problem of mechanical shock due to unstable molecular anchoring at the surface. The AFLCs are attractive for their tri-stable switching behavior, micro-second response, intrinsic analog gray-scale capability, hemi-spherical viewing angle (in-plane switching geometry) high contrast ratio and no-ghost effect [20]. AFLCs are also interesting for the basic studies in soft condensed matter field as these materials are showing numerous sub-phases mentioned earlier and many other with distinct macroscopic properties. So enough scope is here for improvement of display industry in the coming years with fascinating properties of AFLC materials.

References

1. E Reinitzer, Monatsh. Chem. 9, 421, 1888; English translation of this paper: Liq. Cryst. 5,7, 1989.
2. O. Lehmann, Z. Phys. Chem. 4,462 1889.
3. Reinitzer, Friedrich "Beiträge zur Kenntniss des Cholesterins". *Monatshefte für Chemie (Wien)* **9** (1): 421–441, 1888
4. "Ph. D. Thesis" – Baburam Jaishi.
5. "Textures of Liquid Crystals"- Ingo Dierking.
6. Goodby, J.W. (Ed.). *Ferroelectric Liquid Crystals. Principles, Properties and Applications*. Gordon and Breach Science Publishers S.A., ISBN 2-88124-282-0, London, United Kingdom. 1991
7. Meyer, R. B. "Structural Problems in Liquid Crystal Physics," in *Molecular Fluids*, Balian, R. Weill, G. (Eds.); Gordon and Breach, London, 1976; p 272. This paper presents a written account of work presented at the "Summer School of Theoretical Physics," held in Les Houches, France, August, 1973. Meyer also presented this idea, along with preliminary experimental results, in a famous talk at the Vth International Liquid Crystal Conference in Stockholm, in 1974.
8. Meyer, R. B.; Liebert, L.; Strzelecki, L.; Keller, P. J. Phys., Lett. (Orsay, Fr.) 36, L-69-L71. 1975
9. F. Gouda, K. Skarp and S. T. Lagerwall, *Ferroelectrics*, Vol. 113, pp. 165-206, 1991. *Dielectric Studies of the Soft Mode and Goldstone Mode in Ferroelectric Liquid Crystals*
10. A. J. Leadbetter, J. C. Frost, J. P. Gaughan, G. W. Gray, and A. Mosley, *J. Physics. (Paris)*, 40, 375, 1979.
11. M.B. Pandey, Roman Dabrowski and Ravindra Dhar, *Antiferroelectric Liquid Crystals: Smart Materials for Future Display*, pp389-432, Chapter 10. *Advanced Energy Material*, Ashutosh Tiwary and Sergiy Valyukh(eds). Scrivener Publishing LLC.), 2014
12. ADL Chandani, Y. Ouchi, H. Takezoe, A. Fukuda, K. Trashima, K. Furukawa, and A. Kishi, *Jpn. J. Appl. Phys. Part 2*, 28, L1265, (1989).
13. "Relaxation Phenomena"—W. Hasse and S. Wrobel, 2003
14. Hiraoka K., Takezoe H., and Fukuda, A., *Ferroelectrics*, 147, 13, 1993
15. Moritake, H, Uchiyama Y, Myojin K., Ozaki M, and Yoshino K, *Ferroelectrics*, 147,53, 1993
16. Rosario De La Fuente M., Merino S., Gonzalez Y., Perez Jubindo M. A., Ros B., Puertolas J. A., Castro M., *Adv. Matter*, 7, 564, 1995
17. Hiller S, Pikin S.A., Hasse W., Goodby J. W., and Nishiyama I., *Jpn., J. appl. Phys.*, 33, L1170, 1994
18. Yu. P. Panarin, O. Kalinovskaya and J. K. Vij, *Ferroelectrics*, Vol. 213, pp101-108, 1998.
19. Yu. P. Panarin, O. Kalinovskaya and J. K. Vij, *Liquid Crystal*, Vol. 25, No. 2, 241-252, 1998.
20. J.M. Otton, X. Quintana, P.L. Castillo, *Optoelectron. Rev.*, Vol 12, p.263, 2004

EXPLORING EXOTICITY IN THE REALM OF NUCLEAR PHYSICS: RELEVANCE IN ASTROPHYSICS

Prabir Banerjee

Department of Physics

A B N Seal College, Coochbehar

E-mail: banprabir@gmail.com

ABSTRACT

Of the structure of loosely bound nuclear states, 'halo' states are of contemporary interest so far as the current global research scenario is concerned. In our country also, activities in this regard are well under progress. The long tail of the wave function of the loosely bound valence particle(s) has a bearing on a number of observables that can be exploited to have an understanding of the underlying nuclear structure. Comparing the results of nuclear structure and reaction studies with those obtained from binding energy considerations can be indicative of the origin of the halo states. Transfer reaction is one of the most important reaction channels to populate these loosely bound exotic states.

The synthesis of heavier nuclei at low energies through complete and incomplete fusion reactions is possible where one of the reacting partners has an extended density distribution. Because of very small binding energy (~a few keV) of the valence particles, the probability of such processes may be enhanced significantly, facilitating formation of heavier nuclei at energies around Coulomb barrier. This is worth investigating in the context of nucleosynthesis in the primordial universe and also during stellar burning/catastrophic events (supernova explosion etc.) taking place in the cosmos. It is worthwhile to mention that the energy domain relevant for various astrophysical processes is in the sub-MeV region.

Keywords: *Transfer reaction, breakup and fusion cross sections; coupled channels; neutron- and proton-rich exotic nuclei, inelastic excitations, sub-barrier fusion, nucleosynthesis.*

Introduction

One of the interesting aspects of the study of nuclear reactions involving radioactive beams is the possibility to synthesize new, exotic nuclei [1]. In particular, nuclei located near the neutron or proton drip lines, for which the valence nucleons are very loosely bound, give rise to interesting new phenomena, e.g., formation of halo structures in nuclei like ^{11}Li , ^{11}Be , ^8B [2]. This is an example of quantum mechanical tunnelling in a nuclear bound state. The very low binding energies of the valence particles result in large sizes of these nuclei and thus, in increased probabilities for specific reaction channels such as nucleon transfer and fusion. The synthesis of heavier nuclei at energies below the Coulomb barrier could thus be achieved through fusion reactions induced by these exotic nuclei. Nuclei, on the other hand, are seeds for formation of matter as we see them. Therefore, nuclear reactions taking place at different sites under different conditions in the universe that involve these nuclei are worth considering.

But in the first place, one has to produce these neutron- or proton-rich exotic nuclear systems [3]. For very loosely bound systems the number of available particle bound states is limited and can be populated in a selective way by means of transfer reactions. In order to minimize ambiguities related to nuclear wave functions, single nucleon transfer is preferred. The few well spaced energy levels result in an unambiguous identification of the populated states. However, being very loosely bound (by a few keV of energy), the valence nucleons, on the other hand, are easily separable from the core, making these nuclei 'fragile' and the cross sections for breakup reactions in these channels very large (~a few barns) [2].

Discussions

Many questions concerning the effects of breakup processes on sub-barrier fusion have been raised recently, both from the experimental [4-9] and theoretical [10-12] points of view. From studies of fusion of stable nuclei where breakup process is not so important, it is known that any coupling of the relative motion of the colliding nuclei to nuclear intrinsic excitations causes large enhancements of the fusion cross sections at sub-barrier energies over the predictions of a simple barrier penetration model. It is expected that the same thing happens for coupling to the breakup channel as well, especially for these weakly bound exotic nuclei lying close to or on the neutron/proton drip lines, for which the probability of dissociation prior to or at the point of contact is very high. Therefore, for these nuclei, the cross sections for inclusive processes, i.e., the sum of complete and incomplete fusion cross sections should be enhanced when couplings to the breakup channels are considered. Considered from another point of view, the presence of halo structure means a root mean square (rms) matter radius larger than that deduced from the $r_0 A^{1/3}$ systematic. As a consequence, the sub-barrier fusion cross section should be enhanced since the Coulomb barrier is lowered. On the other hand, one could also argue intuitively that increased breakup probabilities for these nuclei remove a significant part of the flux and thus cross sections for complete fusion would be hindered.

Unlike the neutron-rich nuclei, the valence proton in a very loosely bound proton-rich exotic nucleus has to tunnel through the barrier resulting from the Coulomb repulsion due to the charged core, which hinders the formation of proton halo. In fusion reaction, this might not lead to a significant lowering of the Coulomb barrier when such nuclei interact with a target. Thus the observations made in connection with fusion of neutron-rich nuclei at energies around the Coulomb barrier may not be the same for them. The breakup probabilities of the exotic nuclei depend significantly on the separation energy of the valence nucleon as well as its orbital angular momentum configuration [13]. Any non-zero angular momentum with respect to the core will lead to a centrifugal barrier, which will restrict the extent of the wave function in the coordinate space. The increase of the separation energy of the valence nucleon further decreases the spread of the wave function and thereby the cross sections of the breakup processes in which the valence particle is removed from the nucleus also decrease [13]. If the exotic nucleus has some bound excited state(s), a part of the flux will go to its inelastic excitation(s) from the ground state to the excited state(s). Transition from the ground state into the continuum via the excited state(s) would be possible. All these could affect its fusion with a target nucleus.

Formalism and Results

To investigate the roles of all these effects, inelastic excitation of exotic light projectiles ^{11}Be , ^8B and ^{17}F on fusion with a heavy (Pb) target has been studied at near-barrier energies within a continuum discretized coupled channel (CDCC) method [12, 14,15]. The details of the structure of these projectiles (within a core + valence model) and reaction theory formalism are given in [14, 15]. In addition to the normal coupling of the ground state of the projectile to the continuum, its inelastic excitation to the bound excited state and then coupling to the continuum have also been taken into consideration. The inclusion of these additional couplings has been observed to have striking effect on the fusion excitation function of neutron-rich ^{11}Be on ^{208}Pb whereas it has been found to be nominal for the proton-rich ^{17}F nucleus on the same target. In case of ^{11}Be , complete fusion cross sections are significantly enhanced in the sub-barrier region and suppressed at energies above the Coulomb barrier. The suppression becomes less when additional couplings from the only bound excited state of ^{11}Be at 320 keV are taken into consideration. The pronounced effect of the channel coupling on the fusion process in the case of ^{11}Be has been attributed to its well developed s-wave one-neutron halo structure. On the other hand, calculations for fusion of the one-proton halo nucleus ^8B on a Pb target show a significant suppression of the complete fusion cross section above the Coulomb barrier. This is due to the larger breakup probability of ^8B as compared to that of ^{17}F . However, even for ^8B , there is little change in the complete fusion cross sections as compared to the no-coupling case at sub-barrier energies. However, the effects of continuum-continuum couplings on the fusion cross sections have been found to be minimal.

Conclusions

Accurate calculation of the rates of many reactions (and their time-reversed processes) at low energies under different physical conditions is very crucial in the realm of Nuclear Astrophysics because it plays significant role in estimating the elemental abundance in the universe [16]. Fusion reactions, in which one of the reacting partners has exotic structure, could be facilitated if the overlap of the nuclear wave functions is more

than usual even at distances larger than that at the point of contact. This is worth investigating both theoretically and experimentally. We present a brief review of this interesting topic here from theoretical point of view.

It will be highly suggestive to pursue this study for fusion of a loosely bound light projectile with a three-body (core + valence + valence) structure (for example, for ${}^9\text{Be}$, ${}^6\text{He}$) within the CDCC formalism. Measurement of different components of the fusion cross sections is suggested from an experimental point of view.

References

- [1] W. Loveland, in *Proceedings of the Third International Conference on radioactive nuclear beams* edited by D. J. Morrissey (Editions Frontières, Gif-sur-Yvette, 1993), p.526-536.
- [2] P. G. Hansen, A. S. Jensen and B. Jonson, *Ann. Rev. Nucl. Part. Sci.* **45** (1995) 591 and references therein.
- [3] I. Tanihata *et al*, *Phys. Rev. Lett.* **55** (1985) 2676.
- [4] J. Takahashi *et al*, *Phys. Rev. Lett.* **78** (1997) 30.
- [5] K. E. Rehm *et al*, *Phys. Rev. Lett.* **81** (1998) 3341.
- [6] J. J. Kolata *et al*, *Phys. Rev. Lett.* **81** (1998) 4580.
- [7] M. Dasgupta *et al*, *Phys. Rev. Lett.* **82** (1999) 1395.
- [8] M. Trotta *et al*, *Phys. Rev. Lett.* **84** (2000) 2342.
- [9] V. Tripathi *et al*, *Phys. Rev. Lett.* **88** (2002) 172701.
- [10] M. S. Hussein *et al*, *Phys. Rev.* **C46** (1992) 377.
- [11] C. H. Dasso and A. Vitturi, *Phys. Rev.* **C50** (1994) R12.
- [12] K. Hagino *et al*, *Phys. Rev.* **C61** (2000) 037602.
- [13] R. Chatterjee, P. Banerjee and R. Shyam, *Nucl. Phys.* **A675** (2000) 477.
- [14] P. Banerjee, K. Krishan, S. Bhattacharya and C. Bhattacharya, *Int. J. Mod. Phys.* **E11** (2002) 491.
- [15] P. Banerjee *et al*, *PRAMANA (Ind. J. Phys.)* **61(3)** (2003) 529.
- [16] C. E. Rolfs and W. S. Rodney, *Cauldrons in the Cosmos* (University of Chicago, Chicago, 1988).

STABLE VIOLET TO GREEN LUMINESCENT SILICON NANOPARTICLES PREPARED BY TWO DIFFERENT ROUTES

Bhaskar Das^{a,b,*}, Syed Minhaz Hossain^c and Mallar Ray^d

^aDepartment of Physics, Sister Nibedita Govt. General Degree College for Girls, Hastings House, Kolkata-700027, India

^{b,c}Department of Physics, IEST, Shibpur, Howrah, 711103, India

^dSchool of Materials Science and Engineering, IEST, Shibpur, Howrah, 711103, India

(Corresponding author*; Email: dbhaskarmtb@gmail.com)

ABSTRACT

We have prepared luminescent silicon nanoparticles (Si NPs) by reducing (3-aminopropyl)triethoxysilane (APTES) with sodium ascorbate (SA) in a one-step ‘green’ synthesis method. The properties of these NPs were compared with nanocrystalline Si prepared by oxidation-etching of mechanically milled crystalline Si powder as reported by Ray *et. al* (Solid State Commun 149 (2009) 352-356). Colloids of Si NPs formed by both the routes exhibit intense room temperature photoluminescence (PL) that can be detected with the naked eye. While the mechano-chemical route results in dominant blue-violet PL; the wet-chemical synthesis route, exhibits greenish luminescence. PL from the colloidal suspensions of the NPs prepared chemically is found to be stable even after the four months of preparation. Mechano-chemically prepared samples contain abundant crystals along with amorphous oxides. The chemical route however, results in dominant amorphous phase with trace amount of nanocrystals. A comparative analysis of the optical properties of the chemically prepared sample with the mechanically prepared one indicates that green PL from Si NPs is dominantly due to the contribution of oxide enriched surface and defect states rather than quantum confinement of excitons.

Keywords: silicon, nanoparticles, photoluminescence, oxide

Introduction

Being indirect-gap semiconductor, silicon is a poor light emitter. Canham reported room temperature PL from porous Si [1] for the first time. Later, absorption and emission shifts of Si NPs have been observed which confirms that the size dependent optical properties are present in indirect gap semiconductor as well [2]. Since then researchers have shown a lot of interest in Si NPs for their huge application especially in the field of photonics [3–5]. Despite substantial research work the origin of room temperature PL in Si NPs is yet to be understood completely and under active discussion [6-10]. The opinion on origin of PL in Si NPs is roughly divided into two categories. While one group believes, quantum confinement effect [7, 8] plays the most important role in PL; the other explains the origin of PL in terms of surface effects [6]

In this present work we have studied and discussed about the mechanical route of preparation of Si NPs, optical properties of colloidal suspension of nanocrystalline silicon and synthesized green luminescent colloidal Si NPs by a simple and rapid chemical route. In chemical synthesis we have modified a method reported by Wang *et al.* [12] using APTES as the source of Si.

Experimental

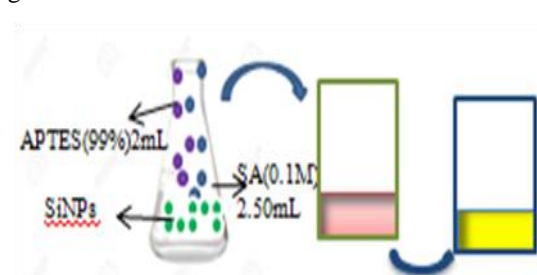
Preparation of colloidal suspension of nanocrystalline Si by mechanical milling:

As reported by Ray *et al.* [11] Si powder from two different sources were used as starting materials (i) commercial Si powder, with average particle size 20 μm with purity of 99.9% (sample: S1) and (ii) Si powder prepared from 2-5 Ωcm resistivity p-type, (100) orientation, Czochralski grown crystalline Si-wafers (lightly B-doped). The wafers were first crushed to reduce the average particle size below 1 mm (sample: S2).

The samples were taken at 10:1 balls (of 10mm) to powder weight ratio in a WC Vial (250mL) in Toluene medium. Toluene was used to minimize oxidation and agglomeration. The ball mill was allowed to operate at 250rpm. After 50hrs milled powder was taken out and kept in clean and covered Petri dishes. The sample was allowed to dry for 3 weeks in a glove box in nitrogen environment. To remove trace of organic and metallic contaminants, if any, a standard piranha etch of the dried powder with 2:1 solution of H_2SO_4 (98%) and H_2O_2 (30%) was carried out. The solution (approximately 0.5g Si powder in 5mL H_2SO_4 and H_2O_2 solution) was then heated slowly at 110°C until the entire liquid evaporated and dry deposits of oxygen rich Si NPs were obtained. The heating was performed in ambient atmosphere inside a fume hood for sufficient oxidation. The piranha etched particles were dissolved in isopropyl alcohol and sonicated to prepare colloidal suspension of particles made of nanocrystalline-Si embedded in SiO_2 . According to the report intense visible luminescence under 365 nm UV excitation could be seen by the unaided eye from the colloidal solution prepared from both the samples.

Synthesis of colloidal Si NPs by the reduction of APTES:

In our case we started with APTES (99%) and Sodium Ascorbate (SA) as the starting chemicals to prepare Si NPs. APTES was purchased from Sigma Aldrich and we synthesized SA in the laboratory of IEST with sodium hydroxide and ascorbic acid. We took 2 mL APTES in a conical flask and added 8mL water with APTES while stirring with a magnetic stirrer. Then 2.5 mL of SA (0.1M) was mixed with the aqueous solution of APTES. The whole mixture was stirred for 10 minutes. The resulting colloidal Si NPs exhibited intense green luminescence under UV irradiation. It took 12-15 minutes to complete the entire process of synthesis. The



whole process has been shown in the schematic (Fig.1). The colour of the sample changes from reddish pink to greenish yellow with the aging of the sample and a blue shift in luminescence could be seen with time discussed later.

Fig.1. Schematic of the synthesis of colloidal Si NPs by the reduction of APTES

Results and discussion

The XRD pattern as reported in [11] clearly reveals the crystallinity of Si. The different planes-(111), (220) and (311) of Si are indexed according to JCPDS card: 27-1402.

While the trace amount of crystalline structure of lyophilized colloidal Si NPs, prepared chemically could be seen with diffraction peaks for (220) and (400) planes along with amorphous oxides in the X-ray diffraction profile (Fig. 2). Most dominant (111) peak is not visible as this peak is masked by the amorphous hump of SiO_2 . This result is expected as Si NPs react with water after synthesis and a thick oxide layer is formed on their surfaces.

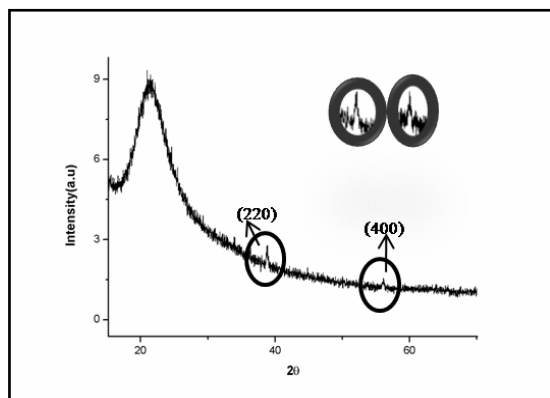


Fig.2. XRD profile of lyophilized colloidal Si NPs. Diffraction peaks for (220) and (400) planes are shown as insets. The planes of Si are indexed according to JCPDS card: 17-0901

In the UV-Vis absorption spectra of the colloidal suspensions of mechanically milled nanocrystalline-Si, reported in [11], the adsorption edges calculated from the point of inflection correspond to 4.3 eV for both S1 and S2. A hump could be seen in the same region (around 290 nm) for the sample prepared by chemical route

(Fig.3). The hump could be due to the presence of trace amount of nanocrystals in sample. The indirect band gaps calculated using Tauc's method are 2.1 and 2.5 eV for S1 and S2 respectively [11]. In case of colloidal Si NPs, synthesized chemically, there is a gradual increase in absorbance with decrease in wavelength from onset wavelength 450 nm (2.75 eV) which is the absorption band edge across the indirect band gap.

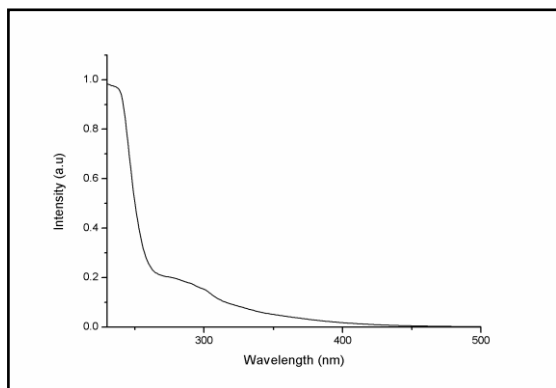


Fig.3. Absorption spectrum of the colloidal Si NPs

The mechanically milled, colloidal suspension of Si NPs [11] and aqueous solution of Si NPs, prepared chemically, exhibit intense room temperature PL which could be detected with the naked eye. According to Ray *et al.* the origin of blue -violet PL at room temperature could be due to the defect states introduced at the interfaces between nanocrystalline-Si islands and amorphous SiO₂ matrix due to invasive oxidation of

chemically treated ball milled nanocrystals-Si. However they did not rule out the role of oxygen related surface states in explaining the origin of PL [11]. Again according to the quantum confinement model, Si NPs of 1-2 nm should emit blue emission [13]. Theoretically at least, Si NPs having average size in the range of 4-5 nm cannot emit blue light due to quantum confinement effect. [13, 14, and 15].

In our case, Fig.4 shows the PL spectra of aqueous solution of Si NPs within excitation wavelength range of 290 to 398 nm. There is a clear indication of red-shift of PL emission spectra with the increase in excitation wavelength. We also note that with increase in excitation wavelength, the intensity of PL peak inconsistently increases or decreases which is inconsistent with the mechanism of PL as explained by quantum confinement effect. There is a clear evidence of blue shift with the aging of the sample (Fig.6). We are inclined to believe that, PL from Si NPs is due to the contribution of oxide enriched surface and defect states (which could be introduced as Si NPs react with water after synthesis and a thick oxide layer is formed on their surfaces) as well as due to quantum confinement of excitons.

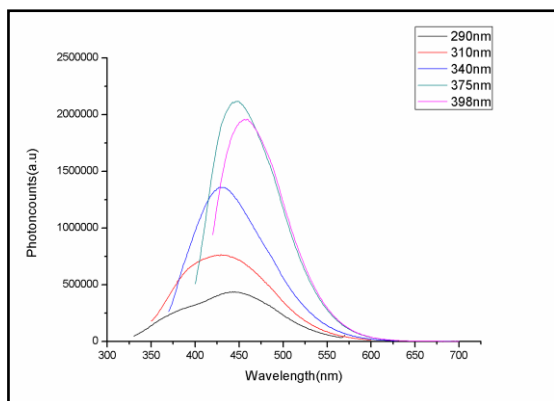


Fig. 4. PL spectra of the colloidal Si NPs at different excitation wavelengths.



Fig.5 Images of as prepared colloidal Si NPs (Day1 and Day2)



Fig.6 Green emission and blue emission from Si NP solution when excited with a LASER of wavelength 400 nm.

Conclusions

We have prepared Light emitting Si NPs successfully by reduction of APTES by SA in a one-step ‘green’ synthesis method which is more rapid and simple process to prepare Si NPs than mechanical milling. In case of chemical synthesis method as the Si NPs react with water soon after its formation, huge amount of amorphous oxide is present along with Si NCs in the prepared sample. On studying the optical properties of the samples we propose that PL from silicon NPs is due to the contribution of oxide enriched surface and defect states as well as due to quantum confinement of excitons.

References

- [1] L.T. Canham, Appl. Phys. Lett. 57 (1990) 1046.
- [2] Y.Kanemitsu, Phys. Rep., 263, 1. (1995)
- [3] L. Pavesi, L. Dal Negro, C. Mazzoleni, G. Franzò, and F. Priolo, “Optical gain in silicon nanocrystals,” Nature, 408(6811), 440–444, 2000.
- [4] K. Y. Cheng, R. Anthony, U. R. Kortshagen, and R. J. Holmes, “High-efficiency silicon nanocrystal lightemitting devices,” Nano Lett. 11(5), 1952–1956, 2011.
- [5] D. P. Puzzo, E. J. Henderson, M. G. Helander, Z. B. Wang, G. A. Ozin, and Z. Lu, “Visible colloidal nanocrystal silicon light-emitting diode,” Nano Lett. 11(4), 1585–1590, 2011.
- [6] Y.Kanemitsu, Phys. Rev. B 49, 16845, 1994.
- [7] M.D. Efremov, V.A. Volodin, D.V. Marin, et al., Pis'ma Zh. Eksp. Teor. Fiz 80, 619(2004), JETP Lett. 80, 544, 2004.
- [8] V. Vinciguerra, G. Franzo, F. Priolo, et al., J. Appl. Phys. 87, 8165, 2000.
- [9] M. Ray, S. M. Hossain, et al., Nanotechnology 21 505602 (9pp), 2010.
- [10] M. Ray, T.S. Basu, et al., Journal of Applied Physics 107, 064311, 2010
- [11] M. Ray et al., Solid State Communications 149 (2009) 352_356
- [12] Jing Wang, Dai-Xin Ye, Guo-Hai Liang, Jian Chang, Ji-Lie Kong, Ji-Yao Chen, J. Mater. Chem. B, 2, 4338-4345, 2014
- [13] Z. H. Kang, Y. Liu, C. H. A. Tsang, D. D. D. Ma, X. Fan, N. B. Wong, S. T. Lee, Adv. Mater., 21, 661 (2009)
- [14] R. D. Tilley, J. H. Warner, K. Yamamoto, I. Matsui, H. Fujimori, Chem. Commun., 1833-1835 (2005)
- [15] J. P. Wilcoxon, G. A. Samara, P. N. Provencio, Phys. Rev. B, 60, 2704-2714 (1999).



BULK VISCOUS COSMOLOGICAL MODEL WITH MODIFIED CHAPLYGIN GAS

Partha Sarathi Debnath

*Department of Physics, A B N Seal College,
Dist.: Coochbehar, PIN: 736 101, India.*

ABSTRACT

We study cosmological solutions in Einstein theories of gravity in the presence of Modified Chaplygin gas which has bulk viscosity type dissipative term. The evolution of the universe is explored considering the imperfect fluid described by Eckart theory. The corresponding cosmological dynamics of the bulk viscous Chaplygin gas is obtained for a flat homogeneous isotropic Friedman-Robertson walker spacetime. We use numerical method to solve nonlinear equation of the evolution of the universe. The interesting feature of the models is that it admits present acceleration phase as well as early inflationary phase with intermediate past deceleration phase of the evolution of the universe. Stability analysis of the models has been discussed. Statefinder diagnostic is also performed for the all models. The present value of the Statefinder parameter is also noted.

Key Words: Chaplygin gas, Bulk viscosity, dark energy

Introduction

The recent cosmological observational data [1] strongly suggest that the most part of the present universe filled with dark matter (~26.8 %) and dark energy (~68.3 %) and the rest (~ 4.9 %) are usual baryonic matter. Dark matter which is supposed to consist of weakly interacting massive particles (WIMPS) with zero effective pressure particle axions (a particle present in the multiplet of grand unified theories) and neutrinos (light particles present in broken supersymmetric models), but none of these particles could not detected until now. Dark energy which is a mysterious entity is responsible for negative pressure. The cosmological constant (Λ) (which arises as the result of the combination of quantum field theory and general relativity) and its generalizations are the simplest way to describe dark energy. However, the theoretical value of the magnitude of Λ is 60-120 orders greater than the observed value [2]. However, there are other candidates [3] for the dark energy namely self interacting scalar-field dark energy models known as quintessence, Kinessence, Brane, Modified gravity field etc.

There exists another route of investigation to describe dark sector of the universe in which dark matter and dark energy are described of a single exotic fluid known as chaplygin gas (CG). Recently, modified forms of Chaplygin gas (MCG) [4] are considered to describe cosmological scenarios. The recent predictions from the observational Astronomy, i.e. supernovae light curve data to WMAP data [1] indicate that the present universe is accelerating. It is also known that the universe might have emerged to the present state from an inflationary phase in the past. In the early universe a number of processes may occurred that could lead to a viscosity in the cosmological fluid. Viscosity may be arises due to the decoupling of neutrinos from the radiation era, the decoupling of matter from radiation during the recombination era, creation of superstrings in the quantum era, particle collisions involving gravitons, cosmological quantum particle creation processes and formation of galaxies [5]. It has been predicted from observations that a non negligible dissipative bulk stress on cosmological scales at the late universe phase might be important. To describe a relativistic theory of viscosity, Eckart [6] made the first attempt. This paper explores viscosity together with chaplygin gas can provide a description of the dark sector of the cosmic medium.

It is the purpose of this paper to consider the effects of possible existence of the bulk viscosity of the modified chaplygin gas on the cosmological dynamics of the universe. The plan of this paper is as follows: in sec. 1, we give the gravitational action and set up the relevant field equations. In sec. 2, cosmological solutions are presented. Finally, in sec. 3, we summarize the results obtained.

1. The Gravitational Action and set up the Relevant Field Equations:

We consider the homogeneous and isotropic space-time given Friedmann Robertson-Walker (FRW) metric

$$ds^2 = -dt^2 + a^2(t) \left[\frac{dr^2}{1-kr^2} + r^2(d\theta^2 + \sin^2\theta d\phi^2) \right] \quad (1)$$

Where $a(t)$ is the scale factor of the universe. The constant k defined curvature of space time $k = 0, 1, -1$ represents flat, closed and open spaces respectively. The Einstein equation in FRW metric (i.e., for a homogeneous and isotropic universe) are given by

$$H^2 = \frac{\rho}{3} + \frac{k}{a^2}, \quad 2\dot{H} + 3H^2 = -p + \Pi, \quad (2)$$

$$\dot{\rho} + 3(\rho + p)H = -3\Pi H. \quad (3)$$

Where $H = \frac{\dot{a}}{a}$ is the Hubble parameter and an over dot represents derivative with respect to cosmic time(t). Where we consider $8\pi G = 1$, $c = 1$. Where p is the isotropic pressure of the universe, ρ is the energy density of the universe and $\Pi (\leq 0)$ is the bulk viscous pressure. In this article we consider that our universe is field with the MCG and the isotropic pressure p of the cosmological fluid obeys a MCG equation of state [4] of the cosmological fluid, i.e. $p = B\rho - \frac{A}{\rho^\alpha}$. (4)

Where $B (0 \leq B \leq 1)$, $\alpha (0 \leq \alpha \leq 1)$ and $A (A > 0)$ are constant. The deceleration parameter (q) is related to H as

$$q = \frac{d}{dt} \left(\frac{1}{H} \right) - 1. \quad (5)$$

The deceleration parameter is negative for accelerating and positive for decelerating phase of the universe. Using equations (2)-(4) for flat universe ($k = 0$), we obtain

$$\Pi = -2\dot{H} - 3 \left[1 + B - \frac{A}{3^{\alpha+1}} \frac{1}{H^{2\alpha+2}} \right] H^2. \quad (6)$$

2. Cosmological Solutions:

The set of equations (2)-(6) are employed to obtain cosmological solutions. The systems of equations are not closed as the numbers of equations are less than the number of unknowns. The bulk viscous stress satisfies following transport equation [6]

$$\Pi = -3\zeta H, \quad (7)$$

Where $\zeta (\geq 0)$ is the co-efficient of bulk viscosity. The positive entropy production due to bulk viscosity is confirmed by positive sign of the co-efficient of bulk viscosity (ζ). It is known that the coefficient of bulk viscosity in general function of time (or of the energy density). We, therefore, consider following relation [7]

$$\zeta = \beta \rho^s, \quad (8)$$

Where $\beta (\geq 0)$ and $s (\geq 0)$ are constant. The constant β is known as bulk viscous constant. It is worth to note that $\beta = 0$ indicate that there is no dissipative effect in the evolution of the universe.

Using equations (7)-(8), equation (6) becomes

$$2\dot{H} + 3(1+B)H^2 - \frac{A}{3^\alpha} \frac{1}{H^{2\alpha}} = \beta 3^{s+1} H^{2s+1} \quad (9)$$

In the above equation A and β are dimensional constant, i.e., for a given value of α and s it remains dimensionally correct.

Using Eq. (5), Eq. (9) can be rewritten in terms of deceleration parameter as

The presence of 3rd and 4th term in the right hand side is due to MCG and bulk viscosity respectively. The combination of bulk viscosity with Chaplygin gas here acts as dark energy of the universe. Number analytic cosmological solutions may be obtained from eq. (10), a detail study please go through Ref [8]. The following cases are considered here: (i) If $s = \frac{1}{2}$, $A = 0$, $\beta = \frac{B+1}{\sqrt{3}}$; the evolution of the universe exhibits de Sitter type expansion ($q = -1$) even in the presence of matter. (ii) If $s = \frac{1}{2}$, $A = 0$, $\beta \leq \frac{B+1}{\sqrt{3}}$; the evolution of the universe exhibits Friedman-like behaviour ($q = \text{const.}, \text{but } q \neq -1$). In this paper to a numerical solution of the field equations are mainly discussed, so a numerical technique is adopted same as Ref [9]. We plot q vs H for different values of other parameters. Assuming that cosmic comoving time (t) is determined by a monotonically decreasing function of Hubble parameter ($t \sim \frac{1}{H}$). The earlier phase of evolution of the universe is described by higher value of H and the later phase of the evolution of the universe is described by smaller H . The field equation (10) suggests that the effect of modified chaplygin gas (MCG) is higher at the later phase of the evolution of the universe than earlier phase of evolution of the universe. If $s \geq \frac{1}{2}$, then the bulk viscosity dominates at the earlier stage of the evolution of the universe. In this case one may obtain three phases of evolution of the universe, as described by: earlier accelerating (i.e., inflation) phase dominated by bulk viscosity, followed by an intermediate deceleration phase dominated by matter content of the universe and finally the present accelerating phase dominated by the MCG. In this model there may be no further deceleration phase of the evolution of the universe. From the graphical plot of q vs H the following points are noted:

(i) The variation of q with H for different values of Chaplygin parameter (A) are shown in fig. (1) for a given set of other parameters. It is evident that the universe has one deceleration phase and two accelerating phase. Let us consider cosmic time (t) is estimated as $\sim \frac{1}{H}$. The early inflationary phase may be obtained due to presence of viscous effect and present accelerating phase may be obtained due to presence of chaplygin gas. The universe entered into the accelerating phase followed by decelerating phase in addition to early inflation phase. The figure shows that for the smaller values of Chaplygin parameter (A), the period of decelerating phase is larger. In the absence of MCG ($A = 0$) the evolution of the universe doesnot exhibits late (i.e., present) phase of acceleration.

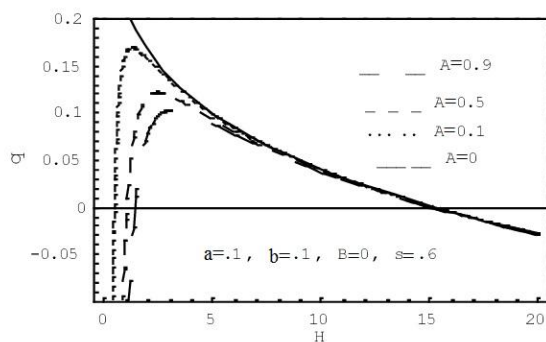


Fig 1: Shows the variation q vs H for different value of A with $\alpha = 0.1, \beta = 0.1, B = 0$, and $s = 0.6$.

(ii) The variation of q with H for different values of Chaplygin gas parameter α are shown in fig. (2) for a given set of other parameters A, B, β, s . It is evident that the universe entered into the accelerating phase followed by decelerating phase in addition to early inflation phase. The figure shows that for the smaller value of α the period of decelerating phase is shorter.

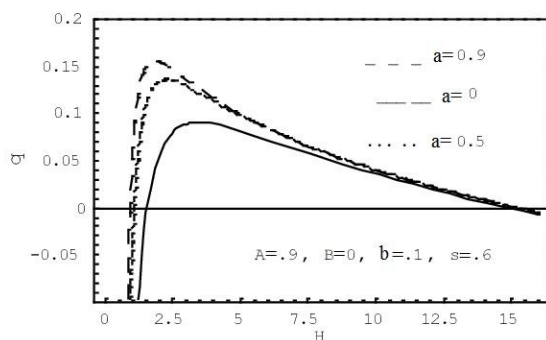


Fig 2: Shows the variation q vs H for different value of α with $A = 0.9, \beta = 0.1, B = 0$, and $s = 0.6$.

(iii) The variation of q with H for different values of viscous exponent parameter s is shown in fig. (3) for a given set of parameters A, B, β, α . It is evident that the universe entered into the accelerating phase followed by decelerating phase in addition to early inflation phase. The figure shows that for the smaller value of s the

period of decelerating phase is shorter.

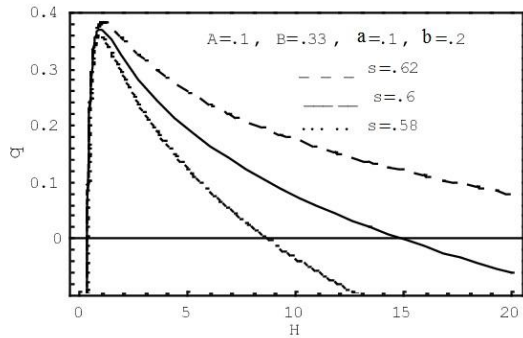


Fig 3: Shows the variation q vs H for different value of s with $A = 0.1$, $\beta = 0.2$, $B = 0.33$, and $\alpha = 0.1$.

(iv) The variation of q with H for different values of equation of state (EoS) parameter B is shown in fig. (4) for a given set of parameters A, s, β, α . It is evident that the universe has entered into the accelerating phase followed by decelerating phase in addition to early inflation phase. The figure shows that for the smaller value of B the period of decelerating phase is shorter

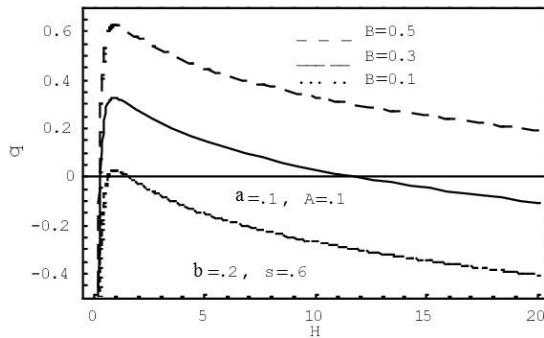


Fig 4: Shows the variation q vs H for different value of B with $A = 0.1$, $\beta = 0.2$, $s = 0.2$ and $\alpha = 0.1$.

Stability Analysis

The stability of cosmological model with chaplygin gas and viscosity are studied in different literature [8] and found that viscous modified chaplygin gas model is completely stable and also consider observational data. The chaplygin gas cosmological model provides an example of a model where entire trajectories are stable [10]. The stability of FRW cosmological models with the chaplygin gas of 2-dimensional system are studied [11].

Statefinder diagnostic

In this paper chaplygin gas with bulk viscosity is considered as dark energy. One of the properties of dark energy is that it is model dependent. Sahni et. al [12] proposed a new geometrical diagnostic pair, based on dimensionless parameter (r, S) which are function of scale factor and its higher order time derivatives are known as Statefinder diagnostic tools. The Statefinder is a geometrical diagnostic tool and allows us to characterize the properties of dark energy in a model independent manner. The Statefinder pair (r, S) are defined as follows:

$$r = \frac{\ddot{a}}{a} H^3, \quad S = \frac{r - 1}{3(q - 1/2)} \quad (11)$$

In the Eckart theory using Eq. (9) and (10) the value of the statefinder parameter becomes

$$r = 1 + \frac{1}{2 H^3} \left[\frac{\beta(2s+1)}{2 3^{-s-1}} H^{2s} - \frac{A \alpha}{3^\alpha} H^{2\alpha+1} - 3 B H \right] \times \left[\beta 3^{s+1} H^{2s+1} + \frac{A}{3^\alpha} H^{2\alpha} - 3(1+B) H^2 \right] \quad (12)$$

$$S = \frac{2(1-r)H^2}{\frac{3A}{3^\alpha H^{2\alpha}} - 3 B H^2 + \beta 3^{s+1} B^{2s+1}} \quad (13)$$

The above expression of the Statefinder parameter can be used to study Statefinder diagnostic in Eckart theory. The plot of r vs H in Eckart theory of different value of Chaplygin gas is shown in the figure (5) for a given set of other parameters. The figure shows that the effect of chaplygin gas (A) is more for small value of H . So the late evolution of the universe is mainly controlled by Chaplygin gas (A).

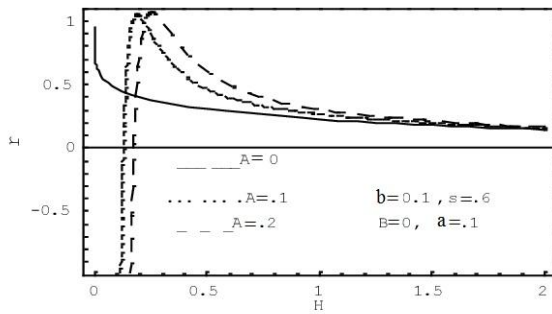


Fig 5: Shows the variation r vs H for different value of A for a given set of other parameter $B = 0$, $\beta = 0.1$, $s = 0.6$ and $\alpha = 0.1$.

The plot of S vs H in Eckart theory of different value of Chaplygin gas (A) is shown in the figure (6) for a given set of other parameter. The figure shows that the effect of chaplygin gas (A) is more for small value of H . So the late evolution of the universe is mainly controlled by

Chaplygin gas (A).

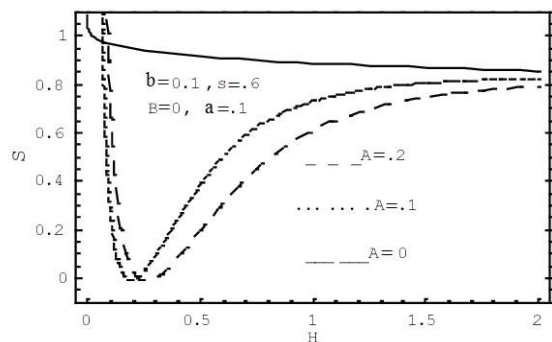


Fig 6: Shows the variation S vs H for different value of A for a given set of other parameter $B = 0$, $\beta = 0.1$, $s = 0.6$ and $\alpha = 0.1$.

We now plot r vs S for different value of A for a given value of other parameters α, B, β, s , in fig (7). The figure shows how the value of the statefinder parameters depend on Chaplygin gas parameter A . It is evident that the presence of chaplygin gas parameter (namely, A) effect more in the future evolution compare to the past evolution of the universe. The parametric plot of r vs S is shown in figure (7) for different value of A . The figure shows how the value of statefinder parameter changes due to presence of Chaplygin gas.

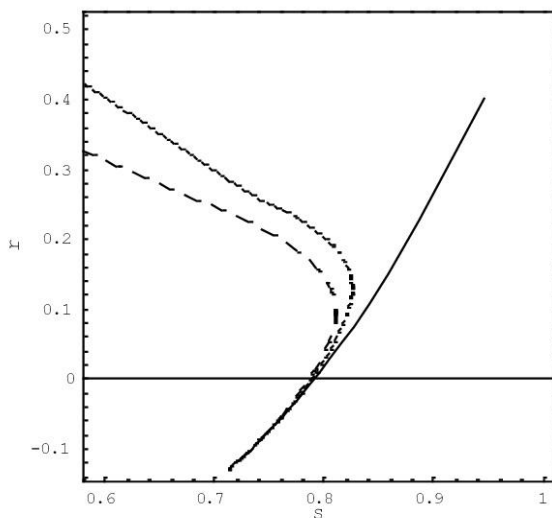


Fig 7: Shows the variation r vs S for different value of A for a given set of other parameter $B = 0$, $\beta = 0.1$, $s = 0.6$ and $\alpha = 0.1$. Where in the figure " $-\quad-\quad A=0.2$ ", " $\cdots\cdots A=0.1$ ", " $\text{---} A=0$ ".

The parametric plot of r vs S is shown in figure (8) for different value of α for a given set of other parameters. The figure shows how the value of Statefinder parameter changes due to presence of Chaplygin gas. The plot indicates that late evolution of the universe is greatly influence by chaplygin gas.

In the absence of Chaplygin gas ($A = 0$) and $s = \frac{1}{2}$ Statefinder parameters of the system are $r = 1 + \frac{9}{2}(\beta\sqrt{3} - 1 - B)(\beta\sqrt{3} - B)$, $S = (1 + B - \beta\sqrt{3})$ i.e., in

this case value of the Statefinder parameters are independent of Hubble parameter. For $1 + B = \beta\sqrt{3}$ the value of Statefinder parameter of the system are fixed point ($r = 1$, $S = 0$), under this condition scale factor of the universe evolve as exponentially ($a(t) \sim e^{c_1 t}$). We would like to mention that the well-known Λ CDM model corresponds to a fixed point ($r = 1$, $S = 0$), in (r, S) plane. The present ($q[H] = -0.5$) value of the statefinder parameters in Eckart theory are determined ($r = 0.94$, $S = 0.02$) for a given value of other set of parameter ($\alpha = 0.01$, $A = 0.02$, $B = 0.3$, $\beta = 0.512$ and $s = 0.9$).

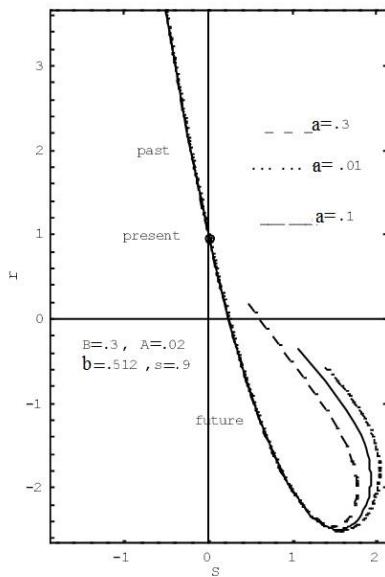


Fig 8: Shows the variation r vs S for different value of α for a given set of other parameter $B = 0$, $\beta = 0.1$, $s = 0.6$ and $\alpha = 0.1$.

Discussion:

In this paper, we explore cosmological models of the universe in the presence of Modified Chaplygin gas which has bulk viscosity type dissipative term which is described in Eckart theory. We adopt here a technique similar to that used in Ref [9]. The relevant equations are written in terms of Hubble parameter H and the deceleration parameter q . We plot q vs H for different parameters that are used in Modified Chaplygin gas which has bulk viscous type dissipative term, namely, α , β , s , A and EoS parameter B . In the entire plot it is found that the present accelerating phase of the universe is followed by past decelerating phase and early inflation, may be described as: earlier accelerating (i.e., inflation) phase dominated by bulk viscosity, followed by an intermediate deceleration phase dominated by matter content of the universe and finally the present accelerating phase dominated by the MCG. It may be note that the universe may remain present accelerating phase, for the large value of chaplygin gas. The period of the present accelerating phase depends on the parameters that are plotted in fig. (1)- (4) which are discussed. The Statefinder diagnostic of the models have studied and their dependence with other parameter are shown in figure (5)-(8).

References:

- [1] A. G. Riess et al., Astron. J. **116**, 1009 (1998); A. G. Riess et al., Astron. J. **607**, 665(2004); S. Permuter et al., Astrophys. J. **517**, 565(1999). P. Astier et al., Astron. Astrophys. **447**, 31 (2006). D. N. Spergel et al., ApJS. J. **170**, 377 (2007).
- [2] S. Permuter et al., Astro Phys. J. **517**, 565(1999); A. Sen, J. High Energy Phys. 0207, 065(2002).
- [3] C. Wetterich, Nucl. Phys. B **302**, 668(1988); S. Hannestad, Int. J. Mod. Phys. A **21**, 1938(2006).
- [4] M. C. Bento, O. Bertolami and A. A. Sen, Phys. Rev. D **66**, 043507 (2002). S. Chaplygin, Sci. Mem. Moscow Univ. Math. Phys. **21**, 1 (1904).
- [5] L. P. Chimento, Phys. Rev. D **81**, 043525 (2010); U. Debnath, A Banerjee and S. Chakroborty, Class. Quantum Grav. **21**, 5609 (2004); B. C. Paul, P. Thakur and A. Saha, Phys. Rev. D **85**, 024039 (2012).
- [6] C. W. Misner, Astrophys. J. **151**, 431 (1968); J. D. Barrow and R. A. Matzner, Mon. Not. R. Astr. Soc. **181**, 719 (1977); B. L. Hu, Advances in Astrophysics, eds. L. Z. Fang and R. Ruffini (World Scientific, Singapore, 1983).
- [7] C. Eckart, Phys. Rev. D **58**, 919 (1940).
- [8] V. A. Belinskii, S. Nikomaro, I. S. Khalatnikov, Sov. Phys. JETP **50**, 213 (1979); R. Maartens, Class. Quantum Grav. **12**, 1455 (1995).
- [9] P. S. Debnath, B. C. Paul, SSRG Int. Journal of App. Phys, **3**, 1 (2016).
- [10] S. Das, N. Banerjee and N. Dadhich, Class. Quantum Grav. **23**, 4159 (2006); P. S. Debnath, B. C. Paul, and A. Beesham Phys. Rev. D **76**, 123505 (2007).
- [11] J. Sadeghi and H. Farahani, Astro. Phys. and Space Science **347**, 209 (2013); V. Gorini, A. Kamenshchik, U. Moschella, V. Pasquier, A. Starobinsky, Phys. Rev. D **72**, 103518(2005).
- [12] M. Szydlowski and W. Czaja, Phys. Rev. D **69**, 023506(2004).
- [13] V. Sahni, Lect. Notes. Phys. **653**, 141(2004); T. Padmanabhan, Phys. Rep. **380**, 235(2003); U. Alam, V. Sahni, T. D. Saini and A. A. Starobinsky, Mon. Not. R. Astron. Soc. **344**, 1057(2003).

